Technical Report No. 21

Climatology of the
HOPE-G
Global Ocean - Sea Ice General Circulation Model

Stephanie Legutke, Deutsches Klimarechenzentrum
Ernst Maier-Reimer, Max-Planck-Institut für Meteorologie
Bundesstraße 55, D-20146 Hamburg

Edited by: Modellberatungsgruppe, DKRZ
Hamburg, December 1999

ISSN 0940-9327

ABSTRACT

The HOPE-G global ocean general circulation model (OGCM) climatology, obtained in a long-term forced integration is described. HOPE-G is a primitive-equation z-level ocean model which contains a dynamic-thermodynamic sea-ice model. It is formulated on a 2.8^{o} grid with increased resolution in low latitudes in order to better resolve equatorial dynamics. The vertical resolution is 20 layers.

The purpose of the integration was both to investigate the models ability to reproduce the observed general circulation of the world ocean and to obtain an initial state for coupled atmosphere - ocean - sea-ice climate simulations. The model was driven with daily mean data of a 15-year integration of the atmosphere general circulation model ECHAM4, the atmospheric component in later coupled runs. Thereby, a maximum of the flux variability that is expected to appear in coupled simulations is included already in the ocean spin-up experiment described here.

The model was run for more than 2000 years until a quasi-steady state was achieved.

It reproduces the major current systems and the main features of the so-called conveyor belt circulation. The observed distribution of water masses is reproduced reasonably well, although with a saline bias in the intermediate water masses and a warm bias in the deep and bottom water of the Atlantic and Indian Oceans. The model underestimates the meridional transport of heat in the Atlantic Ocean. The simulated heat transport in the other basins, though, is in good agreement with observations.

Table of Contents

1 Introduction

In the last decade, increasing attention has been paid to the question of climate change. Numerical simulations of climate change scenarios have been performed at several research institutions (Mitchell and Johns 1997, Manabe and Stouffer 1996, Meehl et al. 1996, Cubasch et al. 1992, Roeckner et al. 1998, Bengtsson et al., 1999). An important aspect of climate change studies is the detection problem which requires the estimation of the natural variability (Hasselmann 1993, Hegerl et al. 1996). This is usually done by means of long coupled model simulation run under present-day greenhouse gas concentrations. Thus, coupled ocean-atmosphere climate models (CCMs) must be able to properly simulate the natural variability of the climate system. The most outstanding signal of natural variability on interannual time scales is the El Nino - Southern Oscillation (ENSO) phenomenon. In the ocean, this phenomenon is tied to changes in the equatorial current system which has meridional scales of the order of 100 km only. The requirement of high resolution, at least regionally in the ocean, is complemented by the requirement that climate change scenarios have to be run for long times of order 100 years, since on shorter time scales, the climate change signal expected to result from anthropogenic influences is of small amplitude compared with that of natural variability.

Here, we present the ocean component HOPE-G of a CCM, designed for studies of both natural variability and anthropogenic climate changes. The variable horizontal resolution of the model is a compromise between high resolution, which allows one to resolve a sufficiently broad spectrum of natural variability, and coarse resolution, which allows one to simulate phenomena with long time scales. An earlier version of this model, HOPE-2, has already been used as a component model of the coupled atmosphere-ocean model ECHO-2. Studies of natural variability (Frey et al. 1997, Venzke et al. 1999) have been performed and the observed mean state of the upper ocean as well as the ENSO variability have been successfully simulated in low to midlatitudes. However, since sea-ice physics were not included, sea surface temperatures (SST) and salinities (SSS) in high latitudes were relaxed to climatological fields instead of being determined interactively in the CCM by the heat and freshwater fluxes calculated at the ocean-atmosphere interface. The wind forcing in high latitudes was taken from Hellermann and Rosenstein (1983). Consequently, the model could not be used in studies of long-term variability, e.g. climate change studies, since watermass formation processes that help to ventilate the deep world ocean become important on long time scales, and these processes are assumed to be strongly influenced by sea-ice formation. In order to use the HOPE model in long simulations, a prognostic fully interactive sea-ice model, including a snow layer, was incorporated. This global version of the ocean model is named HOPE-G. It is described in Section 2.1.

Coupled climate simulations have to be started from a defined initial state. While the atmosphere adjusts to its boundary conditions on a rather short time scale of order several months, the ocean's adjustment time to a change of surface fluxes is of order 1000 years. The calculation of a quasi-steady climatological

state of a coupled model thus requires long, expensive coupled simulations if it is started with an ocean state that differs substantially from the climatological state of the coupled model.
In order to obtain an initial state that is as close as possible to the ocean's climatological state of the coupled model, the ocean - sea-ice model has been spun up to quasi-equilibrium with forcing data produced by the atmosphere component-model. The forcing data and the atmosphere model are described shortly in Section 2.2.

The tuning of HOPE-G started from the model version used in the investigations of the tropical oceans mentioned above (Frey et al. 1997). Some aspects of the model formulation, in addition to the implementation of the sea-ice model, had to be changed during the spin-up run in order to adapt the model to the global set-up used here. No more changes have been made to the model during the last 1000 years of the integration. It has reached a steady state judged by commonly used stationarity criteria (Section 2.3). The mean state and seasonal cycle of the simulated ocean and sea-ice fields are presented in Section 3. The last section concludes with a summary and discussion.

2 Model description and forcing

2.1 The ocean - sea-ice model

HOPE-G is a global version of the Hamburg Ocean Primitive Equation general circulation model HOPE. It was used as the oceanic component in a CCM (Frey et al. 1997, Venzke et al. 1999) with the same horizontal resolution as the model described here, though without sea-ice physics. In a coarser global version, it was used in studies of the impact of sea-ice physics on deep ocean water-mass characteristics (Stössel et al. 1998, Kim and Stössel 1998), and long-term simulations of natural variability (Kim et al. 1998, Stössel and Kim 1998, Drijfhout et al. 1996). Regional studies with higher resolution (Marsland and Wolff 200).

The model is described in detail in Wolff et al. (1997). It is formulated on horizontal (z-) surfaces. The prognostic variables are horizontal velocities $\vec{v}$, potential temperature θ and salinity S, and sea-surface elevation ζ. These variables are calculated from non-linear horizontal momentum equations, conservation equations for heat and salt, and the continuity equation for an incompressible fluid. The baroclinic pressure p is calculated from the hydrostatic equation using a nonlinear equation of state (UNESCO 1983), and the Boussinesq approximation is used with reference density ρ_o.

The momentum equations include parameterisations for horizontal and vertical turbulent viscous momentum dissipation $\vec{F}_H$ and $\vec{F}_V$:

$$\frac{d}{dt}\vec{v} + f(\vec{k} \times \vec{v}) = -\frac{1}{\rho_o}(\vec{\nabla}_H(p + \rho_o g\zeta)) + \vec{F}_H + \vec{F}_V \ .$$

The horizontal viscous dissipation $\vec{F}_H$ is composed of a term depending on the local rate of strain and of harmonic and biharmonic background terms :

$$\vec{F}_H = \nabla(\nu_A T^2 \vec{\nabla}_H(\vec{v})) + A_H \nabla^2(\vec{v}) - B_H \nabla^4(\vec{v}) \qquad (2.1.1)$$

with constant coefficients $A_H = 150\ m^2 s^{-1}$ and $B_H \cdot \Delta t/(\Delta x)^4 = 10^{-3}$. The coefficient T^2 at time step n is composed of the squared strain rate at time step n and of T^2 at the previous time step: $(T^2)^n = \lambda_{T1}(v_x^n + u_y^n)^2 + \lambda_{T2}(T^2)^{n-1}$. With the model time step $\Delta t = 2h$ and with $\lambda_{T2} = 0.9$, this defines a viscous memory time scale of 20 h. The other two coefficients are $\lambda_{T1} = 0.1$ and $\nu_A = 4.5 \cdot 10^{15} \cos(\varphi)\ m^2 s$, where φ denotes the latitude.
At lateral walls and at the bottom, Newtonian friction is applied in addition to no-slip conditions. At lateral boundaries the Newtonian-friction coefficient is of the size of the Coriolis parameter, whereas at the bottom, the coefficient is constant ($=10^{-7} s^{-1}$).

Figure 1 shows the relative importance of the three terms of the right-hand side of eq. (2.1.1) at the end

of the spin-up integration. The profiles represent horizontal-mean values in selected regions of the model domain. In the equatorial Pacific (Figure 1a), the strain-rate dependent dissipation clearly dominates in the upper 300 m, where strong shear currents are simulated (see also Figure 37). The biharmonic and harmonic terms are negligible. They dominate, however, in the Southern Ocean (Figure 1b), which has a coarser horizontal resolution. There, the harmonic viscous dissipation is the most important term in the zonal momentum balance below 500 m. In the upper ocean, the more scale-selective biharmonic term dominates. All three viscous terms decelerate the eastward drift in the Antarctic Circumpolar Current (ACC). In the eastward branch of the subtropical gyre of the North Atlantic, the Gulf Stream Extension, velocities and their shears are weak and so is the shear-dependent viscous dissipation (Figure 1c). In the upper ocean the biharmonic term dominates, while below 500 m the harmonic term is dominant.
From Figure 1 it is clear that the strength of the equatorial undercurrent can be tuned by varying the coefficient ν_A without severely affecting the currents in higher latitudes.

The actual vertical eddy viscosity $\hat{F}_V = \frac{\partial}{\partial z}\left(A_V \frac{\partial}{\partial z}\hat{v}\right)$ also depends on the ocean state at the previous time step as well as on the actual state of the ocean. The eddy coefficient A_V includes a term accounting for shear instability with a dependence on the local Richardson number $Ri = g\rho_o^{-1}\partial\rho/\partial z \cdot [(\partial u/\partial z)^2 + (\partial v/\partial z)^2]^{-1}$ in a way similar to that proposed by Pacanowsky and Philander (1981), a simple mixed-layer parameterisation, and a background term representing mixing by internal wave breaking:

$$A_V^n = (1-\lambda_V)A_V^{n-1} + \lambda_V(A_{V0}(1 + C_{RA}Ri)^{-2} + \delta_{\Delta\rho}W_\rho + A_b). \qquad (2.1.2)$$

λ_V is set to 0.4, corresponding to a decay time of 4 hours. C_{RA} is set to $5 \cdot l/4$, where l is the number of neighbouring wet grid cells. The vertical eddy viscosity is thereby increased near lateral boundaries. In addition, $10^{-3}m^2s^{-1}$ is added to the final value of A_V at the lower boundary of each water column. Both formulations serve to simulate stirring by topographic features. The value for small Richardson numbers is $A_{V0} = 2.5 \cdot 10^{-3}m^2s^{-1}$.
The term $\delta_{\Delta\rho}W_\rho$ symbolises the mixed-layer parameterisation. In cases of weak surface stratification, i.e. when the density difference $\Delta\rho$ between the surface layer and an underlying layer is smaller than a critical value ($\Delta\rho < 7.7 \cdot 10^{-6}\rho_o\Delta z_1 m^{-1}$), the vertical eddy viscosity coefficient is increased by $4 \cdot 10^{-3}m^2s^{-1}$ multiplied by a vertical decay coefficient of 0.4^k, where k is the level index. The critical value we use is set according to Latif et al. (1994) who tuned it to give the best results in the tropical Pacific. However, we use density instead of temperature differences for the mixing criterion, so that the formulation can be applied also at high latitudes. The background viscous coefficient A_b is set to $5.0 \cdot 10^{-5}m^2s^{-1}$. High values of the total vertical eddy viscosity coefficient can diffusively propagate into the interior.

Profiles of effective vertical eddy viscosity coefficients in selected model regions are shown in Figure 2. They display maximum values in the upper ocean due to the mixed-layer parameterisation and the stron-

ger velocity shear there. In the deep ocean, the values are also enhanced, a consequence of the 'topographic stirring' parameterisation.
The Ri-dependent coefficients show a strong seasonality in high latitudes, with higher values in the cold season. This is partly due to the larger velocity shear induced by stronger wind forcing, and partly due to the weaker stratification. The seasonality of the mixed layer term is much less pronounced (Figure 2 b/c).

The momentum flux through the sea surface is composed of the interfacial air/water and sea ice/water stresses, applied to the ice-free and ice-covered part of each grid cell, respectively.
The air/water stress $\vec{\tau}_a$ is taken from the AGCM while the ice/water stress $\vec{\tau}_o$ is calculated with a quadratic drag law: $\vec{\tau}_o = -\rho_o c_w |\vec{v}_1 - \vec{v}_I|(\vec{v}_I - \vec{v}_1)$ with drag coefficient $c_w = 5.5 \cdot 10^{-3}$. $\vec{v}_1$ is the velocity in the uppermost ocean layer. The two-dimensional ice velocity $\vec{v}_I$ is calculated from a momentum balance equation, in which the advection terms are neglected:

$$\frac{\partial}{\partial t}\vec{v}_I = -f\vec{k} \times \vec{v}_I + \frac{\vec{\tau}_a}{\rho_I h_I'} + \frac{\vec{\tau}_o}{\rho_I h_I'} + \frac{\vec{F}_I}{\rho_I h_I'} - g \cdot \vec{\nabla}_H \zeta \ .$$

$\vec{F}_I$ is the force due to the internal ice resistance. It is formulated as in Hibler (1979), i.e. it has a viscous-plastic constitutive law with an elliptical yield curve. The terms ρ_I and h_I' are the density of the sea ice and the ice thickness, respectively.

Salinity and potential temperature are determined from continuity equations including vertical and horizontal eddy diffusivity parameterisations:

$$\frac{dS}{dt} = \frac{\partial}{\partial z}\left(D_V \frac{\partial S}{\partial z}\right) + D_H \nabla^2(S) + \nabla(\nu_D T^2 \vec{\nabla}_H(S)) \,,$$

$$\frac{d\theta}{dt} = \frac{\partial}{\partial z}\left(D_V \frac{\partial \theta}{\partial z}\right) + D_H \nabla^2(\theta) + \nabla(\nu_D T^2 \vec{\nabla}_H(\theta))$$

where $\nu_D = 5.5 \cdot 10^{14} m^2 s$ and $D_H = 1.5 \cdot 10^3 m^2 s^{-1}$ are constant coefficients, and T^2 is defined as for the horizontal viscosity. All parameterisations of diffusion of temperature and salinity conserve heat and salt respectively.
A profile of mean horizontal shear-dependent eddy diffusivity coefficients in the tropical Pacific is shown in Figure 3a. The shear-dependent eddy diffusivity is important only in the upper ocean and only in regions with very strong velocity shear. Elsewhere, it is more than one order of magnitude smaller than the harmonic diffusivity. Its inclusion, however, allowed a reduction of D_H by a factor of 2. Thus, the notoriously high horizontal diffusion of heat in the Southern Ocean could be reduced. This improved the

simulation of the ice edge position.

The vertical eddy diffusivity D_V depends on the local Richardson number in a similar way as the vertical eddy viscosity:

$$D_V^{n+1} = (1-\lambda_V)D_V^n + \lambda_V Max[D_{V0}(1 + C_{RD}Ri)^{-3} + \delta_{\Delta\rho}0.5W_\rho, D_b]. \qquad (2.1.3)$$

This formulation slightly deviates from that used by Latif et al. (1994). We kept their parameterization of the background diffusion with a constant coefficient $D_b = 10^{-6}m^2s^{-1}$ in the upper ocean, but specified it to depend on depth below 500 m, using the profile of Bryan and Lewis (1979). D_{V0} and C_{RD} are $2.5 \cdot 10^{-3}m^2s^{-1}$ and $5 \cdot l/4$ respectively, they thus have the same values as in the vertical dissipation of momentum. The profiles of vertical diffusivity also show seasonal variability in the upper ocean with larger values in the cold season (Figure 3 b/c). At depths, the net coefficient takes on the background values.

At the lateral boundaries and at the sea floor, zero-flux conditions are used.
Surface salinity changes according to internal dynamics by advection and diffusion, and to dilution by freshwater fluxes through the free surface. The latter includes precipitation, snow fall over open water, snow melt, sea-ice growth or melt, continental runoff, and evaporation. The sea-surface elevation ζ is a prognostic variable. It is calculated from the linearized kinematic boundary condition $\partial\zeta/\partial t = -\nabla\int_{-H}^{0} \vec{v}dz + Q_\zeta$, where H is the water depth, and Q_ζ the total net freshwater flux through the surface

Heat fluxes are calculated separately over the ice-free and ice-covered part of each grid cell. The surface heat-flux calculation over open water depends on whether the grid cell is located in an ice region or not. Ice regions are defined by the SST fields derived for the atmosphere-model intercomparison project (AMIP) (Gates 1992). Outside the ice region (defined by $T_{AMIP} > T_{frez} + 0.2^o$ C), the net heat flux as calculated by the atmosphere model is used to update the surface temperature. Over open water in the ice region and over ice, near-surface atmospheric variables and standard bulk formulas similar to those described by Parkinson and Washington (1979) were used for the heat-flux calculation.

The ice is considered to be a two-dimensional slab floating on the water. Continuity equations are solved for the concentration A_I, the grid-cell-mean ice thickness $h_I = h_I'A_I$, and snow depth h_S. Source terms for the mean ice thickness or ice volume are calculated according to the net heat flux through the ice-free part of the grid cell, the conductive heat flux through the snow/ice cover, and surface melt. Net upward heat flux through the ice-free part of the grid cell is interpreted as new-ice growth when the upper ocean temperature is at freezing point. In this case, the ice concentration is also changed assuming that new ice is formed with a thickness of 50 cm. The conductive heat flux through the snow/ice cover is proportional to the inverse effective ice thickness and the difference between the skin temperature and freezing point. The skin temperature is calculated from a heat balance equation. The effective ice thickness includes the

snow depth and accounts for the different thermal insulation properties of snow and ice. Snow accumulates on the sea ice when the net atmospheric freshwater flux is downward and the near-surface air temperature is below freezing point. It melts when the calculated skin temperature is above freezing point. When no more snow is present at melting conditions, surface melt of the sea ice starts. For more details see the technical report of Wolff et al. (1997).

In cases of unstable stratification, convective adjustment is applied. Each pair of vertically adjacent unstably stratified grid boxes is mixed, with heat and salt being conserved. Only one swap is done at each time step. The freezing and melting of sea ice is associated with fluxes of salt and water through the water/ice interface. The corresponding changes of sea surface salinity under freezing conditions destabilise the upper water column and may initiate convective adjustment. In the weakly stratified Southern Ocean, this process acts as an upward pump of heat and salt, but it is confined in nature to the upper ocean in deep water (Martinson 1990). A salinification of bottom water is supposed to occur only in shallow shelf areas. In large-scale OGCMs, convective adjustment is often too strong in the Southern Ocean, and this destroys the weak stratification. The adjustment is therefore switched on only if the density gradient $\partial\rho/\partial z$, evaluated at the interface between two layers, exceeds the critical value of $0.6 \cdot \rho_o \cdot 10^{-12} \mathrm{m}^{-1}$. This is the largest value that could be used without generating instabilities in the equatorial region.
It is not known whether the sinking of dense surface water after haline rejection during the freezing of sea ice occurs in filaments without much dilution, or whether the entire surface column beneath the ice is convectively stirred. In any case, neither a 'rain' of brine-enriched surface water nor local downslope motion of dense water is resolved in the present model. We choose to distributed the salinity increase, associated with freezing of ice, to the upper two layers of the ocean (70% is left in the surface layer). This partially decouples the surface layer from the adjustment process and improves the deep and bottom water characteristics (Legutke et al. 1997). A similar formulation has been used in Maier-Reimer et al. (1993).

Both the ocean and sea-ice equations are discretized on an Arakawa-E type grid, with 20 vertically unevenly spaced horizontal levels. Regarding the distribution of the variables on the grid the reader is referred to the technical report of Wolff et al. (1997). In high and mid latitudes, the position of the even grid lines is that of a Gaussian grid corresponding to a spectral resolution with triangular truncation at wave number 42 (T42). From $\pm 30^o$ on, the meridional resolution starts to increase. The distance between even latitude circles is 0.5^o within ten degrees of the equator. The zonal resolution of the even grid is kept everywhere at that of a T42 grid, i.e. the zonal grid-point distance is 2.8125^o.
The model domain includes the Baltic and Mediterranean Seas, as well as the Hudson and Baffin Bays. The Arctic Ocean is connected to the Pacific by the Bering Strait, and to the Atlantic by the Denmark Strait and the Iceland-Scotland Passage. Besides the continental land masses of America/Greenland, Africa/Eurasia/Indonesia, Australia/New Guinea, and Antarctica, there are 5 additional islands. These are Svalbard, Iceland, New Zealand, the Philippines, and Madagascar.

The northernmost grid cell is treated as an island as well. At its lateral walls, a no-slip condition is applied for the ice velocity. The zonal density gradients are set to zero near the pole, and the baroclinic velocity is computed from geostrophy to avoid fast internal waves in this region.
The vertical levels (at 10, 30, 51, 75, 100, 125, 150, 175, 206, 250, 313, 425, 600, 800, 1050, 1450, 2100, 3000, 4000, 5250 m) are concentrated in the upper ocean with 12 layers above 500 m. A good resolution of the topography, however, is guaranteed since the model formulation allows for partial grid cells at the bottom. The height of the lowermost grid box is specified such that the accumulated height of all boxes at each grid point is equal to the local observed water depth. Thus, the resolution of the bottom topography is limited by the horizontal resolution of the grid only, and not by the number of computational levels. The baroclinic pressure is computed at a constant depth for each layer, and thus does not induce spurious bottom-pressure terms. It has been shown that this formulation gives a smoother flow field above topographic features (Adcroft et al. 1997).

2.2 The forcing data

The forcing has been obtained from an integration of the ECHAM4 atmosphere general circulation model (AGCM). ECHAM4 is the latest version of the AGCM developed at the Max-Planck Institute for Meteorology in Hamburg. The model, which has been adapted originally from the ECMWF weather forecast model, has been extensively modified to adjust it to climate applications. The horizontal representation of the variables (except water components and trace substances) is by a series of spectral harmonics with triangular truncation at wavenumber 42. The vertical domain is resolved by 19 levels with a hybrid σ-p coordinate system and extends to 10 hPa. The lowest level is about 30 m above the surface. Most of the parameterised physics is formulated on the associated Gaussian transform grid (T42) which has a grid-cell size of about 2.8^{o} in both directions. Outside the low-latitude regions with refined ocean grid, the atmosphere land/sea mask is identical to the grid composed by the even lines of the ocean grid.

The ECHAM4 model and its climatology obtained with prescribed monthly mean AMIP SST and sea-ice extent of the period 1979-1994 is described in Roeckner et al. (1996).
ECHAM4 is able to reproduce realistically the observed seasonal mean climate, and intraseasonal variability as represented by the ECMWF operational analyses and the Legates and Willmott (1990) precipitation climatology. The most apparent deficiencies concerning the surface fluxes are a warm bias of 2^{o}-3^{o} in the lower troposphere over the Arctic, an easterly bias of the zonal winds in the tropics, particularly over the tropical Pacific, an underestimated summer monsoon, a lack of precipitation in the Mediterranean area, and underestimated westerlies over the Southern Ocean (Roeckner et al. 1996).
The radiation budget is investigated in more detail in Chen and Roeckner (1996). Overall, the model results are in good agreement with the observed budget as represented by the ERBE data. An overestimated short-wave radiative cloud forcing in summer over the tropical oceans is in accord with the underestimated summer monsoon. Over the eastern tropical ocean, the midlatitude oceans as well as over the

Southern Ocean, Chen and Roeckner (1996) diagnose a lack of low-level clouds in summer.

The daily meanforcing data for the ocean model were obtained from a 15-year run with climatological monthly AMIP SST of the period 1979-1988 specified at the lower boundary. The averaging period of one day corresponds to the exchange frequency of data between the ocean and atmosphere models in the CCM. We therefore account already in the forced ocean spin-up experiment for a large part of the high frequency variability of fluxes that will force the ocean in the coupled experiments. Jumps of forcing data between the end and the start of the 15-year period were smoothed by locally applying a running-mean filter on the first and last 5 days of the data period. The data were cyclically repeated during the spin-up.

Figure 4 to Figure 6 show the 15-year annual-mean fields of surface stress, net heat flux, and freshwater flux applied to the ocean. The wind stress is shown only on the grid points that correspond to the AGCM grid. Note that this field represent the AGCM data only outside the ice region. Inside that region the surface stress is modified by the ice/water interfacial stress.
The atmospheric freshwater flux (Figure 6) is modified by horizontal transport of snow deposited on ice floes. In addition to precipitation and evaporation, continental runoff diagnosed from the atmospheric freshwater flux over land is applied at near-coastal grid cells . The freshwater budget for the ocean is only partially closed by the continental run-off, since the water that falls on continental glaciers is lost with the present formulation of ECHAM4. The net heat flux in ice regions is calculated with bulk formulas from near-surface variables of the ECHAM4 data. We thus also use the near-surface air and dew-point temperatures, as well as cloudiness. The strong cooling of the Southern Ocean, in particular in the Ross and Weddell Seas (Figure 5), results from penetrating deep convection that brings warm circumpolar deep water (CDW) in contact with the cold near-surface temperature of the AGCM, which has been simulated on the assumption of a compact ice cover of 1m thickness.

In addition to forcing the ocean model by fluxes derived from the atmosphere model, SST was relaxed to the climatological monthly AMIP SSTs which were used during the calculation of the atmospheric forcing data, assuming a heat flux of 40 Wm^{-2} K^{-1}. The lowest temperature used is the freezing point. Thus, there is no additional heat flux into grid cells where ice is simulated in agreement with the AMIP data. This is the case in the northern hemisphere. There, at high latitudes, the heat flux related to the SST relaxation is large only in the warm Norwegian and Barents Seas (Figure 7), where the surface water flowing in from the south is too cold and too fresh.
At high latitudes of the Southern Ocean, large cooling due to SST relaxation occurs in regions where strong convective adjustment brings large amounts of heat to the surface. In the Weddell and Ross Seas, the values due to the relaxation term locally amount to 60 and 80 Wm^{-2}, respectively. This is due to the destabilisation of the water column by haline rejection during of sea-ice formation. The surface signal of convective overturning (see also Figure 13) is also seen south and east of Greenland.
In the Southern Ocean, the pattern of heat flux due to SST relaxation displays a patches aligned with the center of the Antarctic Circumpolar Current (ACC). The signs of the flux depend on bending-character-

istics of the ACC , indicating an incompatibility between the zonality of the AMIP SST and the SST the model would like to generate. In particular, in the southern Indian Ocean, the ACC seems to take up too much heat from the Agulhas retroflection, which is then transported southward causing a strong surface cooling of up to 200 Wm^{-2}. It will be shown in Section 3.2, that this is one of the regions where low-salinity Antarctic Intermediate Water (AAIW) is produced in the model.

Cooling dominates off the western continental boundaries. The associated SST error can be attributed mostly to an underestimation of stratiform cloud coverin ECHAM4 and a resulting overestimation of shortwave radiative heat flux there, and to a lesser extent to the insufficient resolution of coastal upwelling.

Over the Kuroshio and its extension, the heat flux due to SST relaxation is from the ocean to the atmosphere. It has the same sign as the net atmospheric heat flux and a slightly more northerly position. Since the net atmospheric heat-flux maximum seems to be too weak by about 30 W/m^2 compared to the COAD data (Oberhuber 1988), the heat flux due to SST relaxation serves to both correct the atmospheric fluxes and the position of the Kuroshio which extends too much to the north. In the Gulf Stream region, the heat flux changes signs across the stream axis, again indicating that the simulated path lies to the north of that observed. This 'Gulf Stream separation problem' is common to most coarse-resolution models (Dengg et al. 1996).

A region with strong positive heat fluxes due to SST-relaxation is the tropical Pacific. The equatorial upwelling seems to be too strong, which can be attributed to the easterly bias in the surface wind stress simulated by ECHAM4 (Roeckner et al. 1996). In addition, Rodger et al. (2000) have shown that a cold bias of temperatures in the eastern upper tropical Pacific results from an insufficient retroflection of the South Equatorial Current in the western tropical Pacific.

Globally, the net atmospheric heat flux entering the ocean is -*2*.46 Wm^{-2}. This is almost balanced by the heat flux stemming from the SST relaxation.

An important aspect of the relaxation-heat flux is the implied meridional transport of heat in the ocean. Starting from the north, the implied heat flux is southwards and decreases monotonically to -1 PW at about 5^o S. The minimum of -1.5 PW is reached at about 45^o S (Figure 9a). Since the ocean has nearly reached a steady state, the heat flux implied by the SST relaxation at the southern boundary of the model domain has about the amplitude of that implied by the net atmospheric heat flux, which is northwards south of 25^oS, in contrast to observations (Trenberth and Solomon 1994). The SST relaxation forces the total implied meridional heat flux in the southern hemisphere to be directed to the south (full curve in Figure 9a).

SSS is also relaxed towards climatological values through the specification of a freshwater flux, which corresponds to an SSS relaxation to annual climatological data (Levitus et al. 1994) on a time scale of 30 days. The relaxation was done only on grid cells where the monthly climatological AMIP SST are higher than $T_{frez} + 0.2^oC$. Thus, as long as the simulated ice cover does not extend equatorwards of the climatological ice edge, the changes of upper-ocean salinity in ice regions are exclusively governed by

the net atmospheric fluxes and the freezing and melting of sea ice. In this way one avoids an uncontrolled flux of fresh water due to SSS relaxation in high latitudes that arises in response to the brine released during the freezing or melting of sea ice.
Near the coasts, the pattern of the freshwater flux corresponding to the SSS relaxation displays localised minima (Figure 8). They result from the freshening due to continental runoff that is diagnosed from the ECHAM4 data. The freshening seems to be too localized relative to the smooth climatological data.
In the open ocean the pattern resembles that of the relaxation-heat flux with the sign reversed due to the tight T/S relationship of sea water. A notable exception is the equatorial Pacific. There, the maximum flux in the Intertropical Convergence Zone (ITCZ) is moved to the west, and the inclination of the South Pacific Convergence Zone (SPCZ) is decreased by the relaxation-freshwater flux. The impact on the implied global meridional freshwater transport in the ocean is less evident than that of the heat flux due to SST relaxation on the implied meridional heat flux (Figure 9b).

2.3 Stationarity

The model has been integrated for 2209 years with the same forcing. However, some changes have been made to the code during the first 1200 years. The most important ones were modifications of sill depths in order to get a better exchange between the ocean basins and peripheral seas (e.g. Mediterranean, Norwegian Sea). Also a tuning of sea-ice parameters and the vertical diffusion under ice and in the deep ocean was necessary in order to improve the deep-water characteristics and stratification.

No changes have been made during the last 1009 years of model integration. Table 1 on page 39 shows trends of global mean potential temperature and salinity and the deviation from the Levitus et al. (1994) climatology at the end of the interation. The trends and errors are largest near 800 m. This is the depth of the intermediate water masses which are generally too warm and too saline. Globally, the ocean freshened by 0.0006 psu during the last 1009 years of the calculation. The input of freshwater by the relaxation was slightly larger than the net atmospheric flux, which was upward. The basin-mean temperature of the world ocean has dropped by 0.008 K.

Figure 10 shows the time series of sea-ice extent of both hemispheres based on 15-year-means. The sea-ice extent in the Arctic has increased by 0.2% in the last 90 years of the integration period. The sea-ice extent time series of the Southern Ocean shows a fluctuation with a very long time scale of order 1000 years. A similar fluctuation is present in the salinity time-series at 3000 m (not shown). The change of Southern Ocean sea-ice extent in the last 90 years of the integration period is less than 0.6% of its total value. The latter, however, is underestimated (see Section 3.4 on page 29).
The trend patterns of temperature and salinity are spatially coherent. However, south of 30^o S the sign is variable (not shown) with the largest values near the Antarctic coast. The peaks are organized in trains of alternating signs indicating that the locations of convective overturning are not stationary.
Useful indicators of stationarity in our model are also the transports of some current systems. In partic-

ular the ACC is sensitive to the stratification in the Southern Ocean. This in turn depends on the strength of convective overturning and on the characteristics of the Circumpolar Deep Water (CDW) which has its origin in the North Atlantic. The volume transport of the ACC has decreased by $0.5 \cdot 10^6 \mathrm{m}^3\mathrm{s}^{-1}$ over the last 90 years, which is about 0.5% of the mean value of 91 Sv. The transport of the Gulf Stream, on the other hand, is still slowly increasing by $0.1 \cdot 10^6 \mathrm{m}^3\mathrm{s}^{-1}$ per 90 years, giving an increase of 0.3% of the mean value (34 Sv) in that period.

3 The mean state

In this section, the climatology of the ocean - sea-ice model is described. Since the model was forced by daily data with a repeat-cycle of 15 years, the terms climatological, annual-mean, monthly-mean etc., if related to model results, denote 15-year-mean values from the end of the integration. The simulated potential temperature and salinity will be compared with 'observations', meaning potential temperature and salinity calculated from the Levitus et al. (1994) climatology which has been interpolated onto the ocean-model grid.

The model grid is in most places coarser than the characteristic scales of observed hydrographic fronts or currents. The comparison of the model circulation with observations will thus be done in terms of volume transport and circulation pattern rather than current speed.

In addition to describing the simulated oceanic circulation and the distribution of temperature and salinity, we follow what has been termed the 'global conveyor belt' (Broecker 1991), including the ventilation of the deep oceans and the meridional redistribution of heat by ocean currents. The description starts with the Atlantic Ocean where the lower limb of the conveyor has its origin (Section 3.1), and will then follow the circuit of the North Atlantic Deep Water (NADW) and later Circumpolar Deep Water (CDW) with the ACC into the Indian (Section 3.2) and Pacific Oceans (Section 3.3). In the Southern Ocean, the CDW participates in the deep and bottom water formation processes, in particular in the Ross and Weddell Seas, which ventilate the deep oceans. The high-latitude oceans, including the sea-ice cover, are described in the last section.

3.1 Atlantic Ocean

The driving agent of the conveyor-belt circulation is commonly assumed to be the cooling of northward flowing Atlantic surface water and the simultaneous increase of its salinity (Figure 5 and Figure 6). The meridional oceanic heat transport implied by the surface fluxes in the North Atlantic is with a maximum of 0.8 PW at 20^o N below observational estimates. The values given by Hastenrath (1983) or Talley (1984), for example, based on surface-flux calculations, amount to about 1.1 PW.

In the model, the net atmospheric fluxes are partially offset by the heat flux due to the SST relaxation. As a result, the oceanic meridional heat transport implied by the total surface fluxes in the Atlantic Ocean is only 0.6 PW, and thus too low. The mean heat transport by the simulated ocean currents is shown in Figure 11a. The estimates of Macdonald and Wunsch (1996), obtained with an inverse model based on hydrographic data, are superimposed. It is evident that the model underestimates the meridional fluxes in the North Atlantic. This deficiency is shared by many other OGCMs (Maier-Reimer et al. 1993, Danabasoglu and McWilliams 1995). High resolution seems to be a necessary but not sufficient condition for a realistic simulation of the northward heat flux in the Atlantic (Böning et al. 1995, Gordon et al. 1998). For example, the values calculated with the model of Semtner and Chervin (1992) are, with a maximum of about 0.8 PW in the North Atlantic, also significantly smaller. The model of Semtner and

Chervin is formulated on a 0.5^ox0.5^o grid. Temperature and salinity are restored to climatological values at all depth within 10^o of the northern and southern boundaries, and everywhere below 710 m. Thus, the model state is not expected to deviate much from the climatological state.
The meridional heat transport has been shown to depend strongly on the Ekmann transport, and thus on the wind fields used in the simulation (Böning and Herrmann 1994). The model results presented here show a high degree of variability in the tropical Atlantic on a monthly basis, with maximum values in northern winter and minimum values in northern summer (not shown). The investigation by Böning and Herrmann (1994) of the seasonal heat flux in the North Atlantic reveals a strong dependence of the seasonal range in the tropical North Atlantic on both the model resolution and the wind forcing. In the subtropical North Atlantic, the wind forcing has the dominant influence. Our annual range in the North Atlantic is 1.6 PW and 0.7 PW at 10^o N and 20^o N respectively, which is comparable to the values of Böning and Herrmann (1994).
We note that the Atlantic basin is not meridionally closed south of 34^o S, the latitude of the southern tip of Africa. The large heat transport of Figure 11a in this region is due to the meandering of the ACC. The southward heat transport poleward of 60^o S reflects the bottom and deep water formation in the Weddell Sea.

Under the combined influence of surface heat and freshwater fluxes, the surface water flowing north experiences a net increase of density. Overturning takes place in the Norwegian Sea, near the Iceland-Faeroe Ridge, and south and east of Greenland at the northern periphery of the subpolar gyre (Figure 13). Loss of buoyancy in the Norwegian instead of the Greenland Sea is in agreement with the revised circulation scheme for the North Atlantic/Arctic Ocean of Mauritzen (1996), in which the Norwegian Atlantic Current becomes gradually dense by heat loss to the atmosphere. This scheme does not invoke deep convection in the Iceland and Greenland Seas as did previous theories of NADW formation.
The exchange with the Greenland/Norwegian Seas is not seen in the barotropic streamfunction, since it is highly baroclinic. Direct transport calculations give an inflow and outflow of 4.4 Sv and -5.4 Sv through the Denmark Strait respectively. The exchange through the Faeroe Channel is 3.7 Sv and -4.1 Sv. The imbalance is mainly due to a flow of 1.4 Sv from the Pacific into the Central Arctic through the Bering Strait. This is larger than the measured estimate of 0.8 Sv given by Roach et al. (1995). It may be a consequence of a too large Bering Strait cross section and water depth, due to the constraint that it is represented by at least one vector grid point and three layers.

The newly formed deep water flows southwards in the western basin and on both sides of the Mid-Atlantic Ridge (Figure 14a). This deep-water flow seems to be less concentrated at the western boundary between 45^o-25^o N than some direct observations indicate. However, Macdonald and Wunsch (1996) also found with an inverse model that 'the southward deep flow is not always tightly tied to the western boundary'. Near 25^o N, the simulated southward deep flow converges and forms a boundary current that crosses the equator and transports NADW southward. Some of the overturned water reaches a depth of

3500 m. However, most of it flows southward at shallower depths (Figure 12a). The maximum value of the streamfunction in the North Atlantic is 14.5 Sv, with an outflow of 11.3 Sv at 30^o S and 3.2 Sv upwelled in the North Atlantic between 45^o N and 30^oN. Estimates of the transport of NADW lie in the range of 12-15 Sv augmented by 4-5 Sv of upwelled and modified Antarctic Bottom Water (AABW) (Schmitz and McCartney 1993, Schmitz 1995, Macdonald 1993).
The small volume transport of the southward flowing NADW in the model is probably related to the fact that the water involved in the overturning in the northern North Atlantic is too warm and not sufficiently dense, when it is formed in the Greenland/Norwegian Seas (see Section 3.4) and in the northern North Atlantic. Furthermore, in z-level OGCMs with their poor representation of the overflow processes, the overflow water crossing the Greenland/Scotland Ridge is normally too strongly mixed with the less dense surrounding water. Both the low transport and the fact that the water mass is too warm contribute to the underestimation of the northward heat transport. Böning et al. (1995) have shown that excessive upwelling in the North Atlantic can be another reason for a too low northward heat transport in the subtropical North Atlantic, even when the NADW formation is realistically simulated. They showed that isopycnal advection and mixing parameterization of tracer transports by mesoscale eddies can yield a substantial improvement of the outflow of NADW and northward heat transport. The HOPE-G model has a diffusion parameterisation which operates on horizontal surfaces. However, even with this simple parameterisation only 28% of the overturned water upwells, while Böning et al. (1995) report values up to 50% in their study.

Northward flow across the equator into the North Atlantic compensating for the outflow of NADW has been observed in the upper ocean and in the depth range of 400 to 800 m. In between, the Equatorial Undercurrent (EUC) is the most prominent feature of the circulation in the equatorial Atlantic. A large part of the northward flow retroflects near the equator and feeds the EUC (Figure 20c). Above (Figure 14b) and below, the near-shore current directly enters the Caribbean Sea, circulates in the Gulf of Mexico, and exits south of Florida as the model's Florida Current. The eastward transport south of Florida amounts to 14 Sv. This is well below the 30 Sv deduced from observations, which are composed of an inflow from the South Atlantic of 13 Sv and of 17 Sv of subtropical-gyre return flow into the Caribbean Sea (Schmitz and McCartney 1993). In the model simulation, only a small portion of the subtropical-gyre return flow passes through the Caribbean Sea. Most of it stays north of the Caribbean islands (which are resolved only as a submarine ridge). Together with a recirculation cell, the mean transport of the model's Gulf Stream reaches a maximum of 34.4 Sv. This low transport, as well as the late separation of the Gulf Stream, can be attributed to the coarse resolution. Model studies suggest, however, that this problem is not even solved with resolutions that are beyond the reach of what is affordable in climate simulations (Dengg et al. 1996).
The interior flow of the subtropical gyre extends across the entire central and eastern North Atlantic (Figure 14b and Figure 13). There is a mean inflow into the Mediterranean Sea of 0.86 Sv in the upper layers. The outflow at deeper levels is smaller (-0.83 Sv) due to an excess of evaporation over precipitation.

These figures are slightly below the values of +0.90/-0.86 Sv given by Bryden and Kinder (1991) which are based on measurements and a hydraulic-control model. The upper Mediterranean outflow is to the north and to the south in the depth range 600 m to 800 m, while the deeper flow at a depth of 1050 m is to the south only. The impact of the Mediterranean water on the salinity distribution is too strong in the upper levels if compared with the Levitus climatology (Levitus et al. 1994), while it is too weak at 2000 m (not shown). The resulting underestimated vertical density gradient may also contribute to the weak flow of NADW. This can be attributed to the poor representation of overflow dynamics in z-level models. The dense overflowing water is too strongly mixed with the lighter ambient water before it can reach its observed depth.
The model does not simulate a southern recirculation cell of the North Atlantic Current (NAC) as described by Schmitz and McCartney (1993). They argue that in this gyre the water is further cooled and preconditioned for its later role in the deep-water formation of the northern hemisphere. The absence of this feature can be one of the reasons for the warm bias of the NADW in the simulation.

South of 30^o N, below the NADW, a deep overturning cell extending to 25^o N is simulated with a maximum value of 5 Sv (Figure 12a), which is related to Antarctic Deep and Bottom Water (AAD/BW) formation in the Southern Ocean. The spreading of the abyssal waters in the North Atlantic can be inferred from Figure 14c. A comparison with Figure 13 of Schmitz and McCartney (1993), which is based on independent studies, shows that many of the circulation features that are known from hydrographic observations are reproduced by the model. Note that Figure 14c displays the horizontal flow in the deepest box of each water column. Thus, the southward flows in the north and along the continental slope of South America represent NADW at depths above 3500 m. AABW flows northward along the continental slope (northeast and deeper than the NADW) and along the eastern slope of the Mid-Atlantic Ridge. The eastern branch crosses the ridge south and near the equator to join the western branch. The flow separates again into two branches at the latitude of the Vema Fracture Zone (6^o N). One part turns east through the fracture zone and keeps that direction until it nearly reaches the African coast, where it retroflects westward and then turns north into the Canary Basin. The other part continues moving northwest along the continental slope and invades the southern North America Basin. In the eastern part of this basin, some of the flow continues northward until it meets the southward flowing NADW at about 38^o N. In the eastern North Atlantic, the abyssal flow of AAD/BW extends to about 48^o N.
It was mentioned above that the NADW is too salty and too warm. The error in abyssal temperatures (Figure 15a) is thus generally higher in the northern North Atlantic (locally up to 1.6^o C), where the influence of the NADW is strongest. It decreases towards the south and has disappeared in the subtropical South Atlantic. The influence of the NADW on the salinity error displays a similar pattern, with a positive bias of up to 0.15 psu in the north, and negative errors of comparable magnitude south of the equator (Figure 15b).

The streamfunction of the zonally integrated flow in the Atlantic Ocean exhibits 8 Sv of South Atlantic water upwelling near the equator and ca. 2 Sv crossing the equator at about 650 m, which is the depth of the low-salinity intermediate water of the model. These circulation features are consistent with those described by Schmitz and McCartney (1993).

The barotropic streamfunction (Figure 13) indicates leakage of at least 5 Sv of Indian Ocean water into the South Atlantic. Observational estimates of this "Agulhas leakage" range from 3 to 14 Sv (Peterson and Stramma 1991). Such a flow is likely to occur if the southern tip of Africa lies north of the line of zero wind stress curl (Godfrey 1989) which applies to our wind stress forcing (not shown). The simulated westward flow through a meridional section that cuts the coast of Africa at its southwesternmost point amounts to 6.7 Sv. Of this, 3.2 Sv is upper water (above 350 m) and 3.5 Sv consist of low-salinity water at intermediate levels. The simulated flow pattern at 1050 m in the Atlantic and Indian Ocean sectors of the Southern Ocean (not shown) suggests that the intermediate water leaking into the South Atlantic is also of Atlantic origin and recirculates in the Indian Ocean as described by Gordon et al. (1992).

The strength of the Agulhas leakage is related to the question of how the NADW is replaced in the model, i.e. the question of the relative importance of the 'warm water path', meaning a replacement by warm Indian Ocean upper water flowing in from south of Africa as hypothesized by Gordon (1986), and the 'cold water path', which means a replacement by cold AAIW that enters through the Drake Passage (Broeker 1991, Rintoul 1991). Garzoli and Gordon (1995) estimate that about 10 Sv of the NADW replacement flow follow the 'cold water path' while 2-5 Sv enter south of Africa. This picture is also supported by Schmitz (1995).
It is believed that the relative importance of the 'cold' and 'warm water paths' in OGCMs depends on the horizontal resolution, with coarse-resolution models favoring the cold water path (Drijfhout et al. 1996). In HOPE-G, the volume transport of the Agulhas leakage is about 60% of the outflow of NADW at 30^o S. Semtner and Chervin (1992), with a 0.5^o model, also simulate an almost equal partitioning of the NADW replacement by the 'cold' and 'warm water route'. However, the northward heat transport by the model presented here is 0.2 PW at 30^o S, well below the 0.65 PW obtained by Semtner and Chervin (1992). It better agrees with the results of Rintoul (1991) of 0.25 ± 0.12 PW. Zhang et al. (1998), using an isopycnal ocean model of the same horizontal resolution as the one presented here which has been coupled to an AGCM, simulate 12 Sv and 4 Sv of compensating flow using the 'cold' and 'warm water path' respectively.

Figure 16a shows the vertical structure of the meridional flow in a zonal section along 32^o S in the South Atlantic. At the western boundary, a shallow Brazil Current transports 4.5 Sv upper water to the south. East of that current, concentrated in the upper 350 m, a northward flow of 5 Sv is simulated which is a return flow of the western boundary current in an elongated recirculation cell in the subtropical gyre. Below that recirculation, a deep southward flow of 21.3 Sv transports NADW, but also contains a contribution from the northern limb of the subtropical gyre. Thus, the western boundary current transports

a total of 25.8 Sv. Estimates derived from hydrographic data yield a wide range of values between 4 Sv for the northern part of the Brazil current (when a shallow reference level is used), to 76 Sv for the latitude just before it turns offshore, when the deep water is taken into account (Peterson and Stramma 1991). The model probably underestimates the transport due to its coarse resolution in these latitudes. The western boundary current transport obtained from the Sverdrup relation by zonally integrating the mean wind stress curl along the same latitude amounts 22 Sv.

To the east of the deep western boundary current, the interior flow of the subtropical gyre extends down to about 1200 m. This northward flow intensifies in the upper 300 m at the eastern end of the section off the coast of South Africa. This flow, the Benguela Current, originates partially south of Africa as a leakage of the Agulhas Current. It transports 5.9 Sv in the upper 350 m, with the total simulated transport above 2000 m amounting to 13 Sv. No more than half (6.7 Sv) of the simulated transport can originate from the Indian Ocean. Garzoli and Gordon (1996) have estimated the volume transport of the Benguela Current to be 13 Sv of which 50% originate from the South Atlantic Current (SAC). Stramma and Peterson (1989) found 8 Sv of Indian Ocean water in a Benguela Current with a total transport of 18-20 Sv.

In the eastern basin, the Cape Basin, the flow is directed southwards between 1200 m and 2500 m and is more saline than its environment (Figure 16). This flow transports NADW to the south in a branch that separates from the western boundary current at about 19^{o} S, crosses the South Atlantic, and exits eastwards south of Africa (Figure 17b).

The total northward flow through the deep part of the section is bottom-intensified and transports a total of 8.2 Sv. The deeper part of this flow contains AABW, which has a fresh bias of 0.1 psu, while the temperature errors vary between -0.2^{o}C and 0.6^{o}C. This water is formed in the Weddell Sea (Figure 13) where a total divergence of 4.9 Sv has been calculated for the deepest layer (below 3500 m). The divergence below 2500 m amounts to 10.9 Sv. The Weddell Sea Deep Water (WDW) circulates clockwise after formation and leaves the Weddell Sea towards the north into the Argentine Basin between the Scotia and the Mid-Atlantic ridges. A second flow path is directed towards the east into the Indian Ocean. Part of this flow retroflects at 30^{o} E and reenters the deep basins of the eastern South Atlantic.

The net southward flow through the section is -1.2 Sv and is related to the inflow through the Bering Strait. Note that the net flow through a section is not exactly zero even if the northern boundary is closed, due to the net water flux through the free surface of the model.

Figure 16b shows the distribution of salinity on the same section. At 500-1100 m depth, the salinity-minimum layer of the intermediate water is simulated, which circulates below the thermocline layer of the upper ocean. A comparison with the salinity distribution of the Levitus climatology (not shown) reveals that the observed salinity-minimum layer has a somewhat deeper position of about 100-200 m and is fresher by about 0.2 psu. Please note also the fresh signal at 1050 m depth in the west. It extends along the coast until about 10^{o} S and is due to a weak northward flow along the American coast in northern winter. This signal is not seen in the Levitus climatology. It fits, however, to the salinity distribution and schematic circulation shown by Warner and Weiss (1992). Low-salinity intermediate water in the South

Atlantic is formed by coastal downwelling and wintertime convection in the confluence zone of the Brazil and Malvinas Currents. The low-salinity water spreads eastwards and northwards with the SAC and enters the Indian Ocean from the east (Figure 18). This picture of the formation of South Atlantic AAIW is similar to that obtained by England (1992) with a different model.

The salinity pattern at 32^o S (Figure 16b) suggests a simple water-mass classification. The water above 500 m with salinity higher than 34.8 psu is assumed to represent the model's thermocline upper water (UW). The water above 1200 m that is fresher than 34.8 psu is the intermediate water (IW), water with a salinity above 34.8 at levels below 500 m is deep water (DW), and the fresh deep water (<34.8 psu, below 1200 m) is bottom water (BW). This classification covers all water masses on the section. A net southward export of 16.5 Sv of deep water through the section is balanced by a net northward flow of 4.7 Sv of upper water, 6.3 Sv of intermediate, and 4.2 Sv of bottom water. All three constituents of the replacement flow (UW, IW, BW) have a contribution from the Indian Ocean, as noted above. The transport figures can be compared with the estimates of Rintoul (1991) who used an inverse model based on 4 hydrographic sections from different years in the South Atlantic. Rintoul (1991) obtained with his 'standard' model a southward flow of 17 Sv through 32^o S, which is balanced by 8 Sv of surface water, 5 Sv of intermediate water, and 4 Sv of bottom water. The results of Rintoul (1991) varied between 13 to 17 Sv, 6 to 8 Sv, 4 to 5 Sv, and 3 to 5 Sv for the deep, surface, intermediate, and bottom water respectively. With none of his models, however, Rintoul (1991) obtained an inflow of Indian Ocean thermocline water from the east. The meridional heat flux simulated at 32^o S with HOPE-G (Figure 9a) is just at the lower limit of the range given by Rintoul (1991). Note, that we calculate the heat flux relative to 0^oC. Since the net mass flux through the section is not zero, and since the water flowing in from the Arctic Ocean has a temperature above 0^oC, this means that our heat transport calculation gives a lower value than if we assumed a zero net mass flux. This correction, however, would be small ($O(10^{-2}$PW)).

When the Agulhas leakage south of Africa turns to the north, it becomes increasingly surface-intensified and unites with the eastern limb of the subtropical gyre to form the Benguela Current. It then becomes the South Equatorial Current (SEC) which crosses the South Atlantic Ocean in a northwest direction (Figure 17a). Near 15^o S, where the SEC hits the South American coast, it bifurcates into a northward branch, the North Brazil Current, and a southward branch that feeds into the Brazil Current.
The Brazil Current forms the western boundary current of the South Atlantic subtropical gyre. It separates from the coast at about 40^o S, where it meets the Falkland Current, a northward branch of the ACC, and flows eastward as the South Atlantic Current (SAC), the southern limb of the subtropical gyre. The ACC flows south of the SAC, with a mean simulated transport of 91 Sv, which is on the lower side of what observational estimates. The SAC and ACC, which exhibit large meanders, are not clearly distinguishable in the model.

The northward flowing branch of the SEC, the North Brazil Current, enters the complicated system of currents, countercurrents, and undercurrents of the tropical Atlantic. This current system undergoes strong seasonal variations. Therefore, the mean zonal equatorial velocity is shown for August and February, the months in which the EUC and North Equatorial Counter Current (NECC) attain their maximum and minimum strengths (Figure 19 a and b). The February pattern shows a high degree of baroclinicity. The EUC is squeezed vertically between two westward flowing currents, the SEC at the surface and a westward flow with maximum velocities at 250 m. There are two other eastward flowing undercurrents below the SEC in February, the North and South Equatorial Under Currents (NEUC and SEUC). Such currents have been observed (Molinari et al. 1981). In the model they exist only in austral summer. Their transports are below those observed (see Table 2 on page 40). The transport values of the EUC, which range between 6 and 9 Sv are well within those estimated from hydrographic measurements. The same is true for the transport of the SEC (Table 2 on page 40).

A comparison of the simulated temperature and salinity with those of the Levitus climatology on the same section reveals smaller spatial structures in the simulations. The EUC is better marked by high salinities slightly to the south of the core of the EUC and by a more pronounced vertical spreading of the isotherms (Figure 19 c - f).

The surface currents in the tropical Atlantic simulated in August and February are shown in Figure 20 a and b. While in February there is a significant contribution from the surface currents to the North Atlantic gyre (replacement of NADW), most of the SEC in August retroflects at the American coast and feeds into the NECC.

Seasonal variations are much smaller south of the equator, where current reversals are seen in the eastern South Atlantic only, in agreement with ship drift data (Peterson and Stramma 1991). The horizontal currents in February at 75 m (Figure 20 c), the depth where the EUC reaches its maximum, demonstrate how the EUC is fed directly by the North Brazil Current from the south. A second contribution from the North Brazil Current enters the EUC from the north after a triple retroflection.

The simulated zonal-mean temperature and salinity in the Atlantic basin and the corresponding data of the Levitus climatology are presented in Figure 21. The simulated temperatures are too high and salinities too low in the deep Greenland/Norwegian Seas and the Central Arctic. Thus, the deep water flowing over the Greenland/Scotland Ridge is not dense enough to help form NADW at a sufficiently large rate in the northern North Atlantic. South of the Greenland/Scotland Ridge, where most of the NADW is formed and the water column is almost homogenized vertically in the simulation as well as in the Levitus climatology, the simulated zonal-mean values are about 1^{o}C too warm and up to 0.2 psu too saline. (The large salinity anomaly at 60^{o} N in 75 m is a result of net ice production in the Hudson Bay. This leads to an accumulation of salt near the bottom, since there is very little exchange with the world ocean in this basin.) As a result, the overturned water is too light (up to 0.1 kg/m^3) and the conveyor-belt driving too weak with only 11.3 Sv outflow at 30^{o} S. In the South Atlantic, both the low-salinity AAIW and the NADW flow at too high levels and are too saline with about the same error. Thus the simulated vertical

salinity gradient is approximately correct. In the Southern Ocean, the deep water formed near the shelf seems to be slightly too warm, in particular in the deep Weddell Sea. The doming of isotherms, however, is well simulated there. The AAD/BW seems to effectively ventilate the deep South Atlantic if judged by the position of the 2^o C isotherm. When crossing the Mid-Atlantic Ridge north of the equator, the AABW is not able to keep the observed fresh and cold characteristics, the bottom water in the North Atlantic is too warm and too salty.

3.2 Indian Ocean

While the strength of the meridional overturning cell and the heat transport in the Atlantic are underestimated, the model satisfactorily reproduces the observed heat transports in the other basins. This is demonstrated for the Indian Ocean in Figure 11b, which shows the advective, diffusive, and total simulated northward oceanic heat transport, together with estimates by Macdonald and Wunsch (1996).
The jump in the curves just south of the equator is related to the Indonesian Throughflow (IT) and has a corresponding jump with reversed sign in the Pacific (Figure 11c).
The large simulated transport poleward of 40^o S has a counterpart in the Atlantic sector of the Southern Ocean and is a consequence of the southward bending of the ACC in the Indian Ocean as opposed to the northward bending in the Atlantic. Almost all the heat transport is advective, with a small contribution by diffusion in the Southern Ocean. Diffusive transports are always poleward.

The bottom water that ventilates the deep Indian Ocean is formed in the Weddell Sea, in the Prydz Bay (70^o to 80^o E), off the east Antarctic coast between 90^o E and 125^o E, and in the Ross Sea (Figure 13). The spreading of the Antarctic deep and bottom water can be followed by its fresh and cold characteristics, which become less distinct along its pathway through mixing with the overlying saltier and warmer CDW (Figure 22). The bottom water formed between 90^o E and 150^o E spreads eastward along the continental slope. Further offshore, the bottom water formed in the Ross Sea enters the Indian Ocean from the east (Figure 23). The Weddell Sea water, after entering the deep Indian Ocean from the west, separates into three branches at 30^o E, with one branch retroflecting into the eastern South Atlantic, another branch flowing north into the Mozambique Basin, and a third branch continuing east until it arrives at the Kerguelen Plateau where it turns north and invades the Crozet and Madagascar Basins. North of 20^o S, the water is quite homogeneous at 34.72 psu and 2.0^o C, except for some saline and warmer water in the northern Arabian Sea and at the Indonesian and Australian eastern continental slopes. There is some leakage of bottom water across the Central Indian Ridge. Deep bottom flow is predominantly southward in the eastern South Indian Ocean.
The simulated distribution of bottom salinity agrees well with the climatology and with that presented by Mantyla and Reid (1995), although a fresh and warm bias in the bottom water of the Weddell Sea is simulated.

Figure 24 shows the meridional flow through a section crossing the Indian Ocean at 32^o S similar to that

shown for the South Atlantic in Figure 16. In the deep layers, there is a tendency for the flow to enter the Indian Ocean in the western basin and to leave it further east.

In the upper layers, the Agulhas current and some recirculation are simulated in the west. Further to the east, the model simulates a southward flow east of Madagascar, and a northward interior flow in the South Indian subtropical gyre. The total simulated transport of the Agulhas Current west of 50^{o} E amounts to 64 Sv, which compares well with the estimate of 60-65 Sv from hydrographic data by Stramma and Lutjeharms (1997). The western boundary current transport obtained from the Sverdrup relation by zonally integrating the mean windstress curl along the same latitude is 42 Sv. In agreement with the finding of Stramma and Lutjeharms (1997), most of the northward return flow is in the western Indian Ocean.

Near the Australian coast, the southward Leeuwin Current with an annual mean transport of 1.2 Sv is simulated at the surface. This current is strongly seasonal and most prominent in austral autumn with a maximum mean southward transport of 2.3 Sv in May and minimum transport of 0.4 Sv in October. Smiths et al. (1991) arrived at transport of 5 Sv while Toole and Warren (1993) obtained only 0.7 Sv from hydrographic data. Below the Leeuwin Current, and slightly to the west, the West Australian Current (WAC) is simulated with a transport of 8 Sv.

The barotropic streamfunction in the southern Indian Ocean (Figure 13) fits well to the schematic based on historical hydrographic data presented by Stramma and Lutjeharms (1997) for the flow above 1500 m, except for differences in the northeastern South Indian Ocean where the simulated flow has a significant baroclinic component. Most of the model flow that feeds the Agulhas Current arrives from the east and south of Madagascar. The Mozambique Channel adds only 9.4 Sv. Stramma and Lutjeharms (1997) included a flow of 5 Sv through the Mozambique Current, other estimates are 10 Sv (Harris 1972) or 6 Sv (Fu 1986).

Table 5 on page 43 contains the accumulated transports through the section in six layers defined by their densities, which are taken to represent the model's upper-layer water, the intermediate water, the deep, and the bottom water. The density classes are taken from Schmitz (1995), except for the bottom water which is defined here to be denser than 27.75 rather than 27.8 to account for the light bias of the bottom water in the model. With this classification, the model simulates a southward flow of -13.8 Sv of upper water, a net southward flow of -1.1 Sv of intermediate water, and a net northward flow of 1.3 Sv of bottom and deep water. There is a large recirculation associated with the flow in each layer. For example, in the upper deep water class, with a net northward transport of 0.8 Sv, the recirculation is as large as 15.5 Sv. Estimates based on measurements vary considerably depending on the data and the method used. For example, while Toole and Warren (1993) obtained a net northward flow of 11 Sv in their NADW layer (here: UDW), Robbins and Toole (1997), with the same data, obtained a revised figure of 2 Sv with a recirculation of 14-15 Sv when silicate-conservation arguments were included in the model. Compared with the net northward transport of 9 Sv of bottom water given by Robbins and Toole (1997), our ventilation rate is rather weak. An underestimated ventilation rate by AABW is also suspected from the pat-

terns of zonally integrated temperature and salinity, if compared with the Levitus et al. (1994) climatology (Figure 25). The deep water is too warm and near the Antarctic coast it is too homogeneous vertically. However, in the upper 1000 m, the climatological pattern is well reproduced. Near the northern coast, the downward slope of the isotherms is underestimated between 500 m and 2000 m. This can again be attributed to the inability of the model to adequately represent the downslope spreading of dense water, similar to the finding for the Mediterranean outflow.

The net outflow of intermediate water at 32^o E is also significantly below the values obtained from hydrographic data. Toole and Warren (1993) and Macdonald (1993) found a net outflow of 9 Sv of intermediate water. Schmitz (1995) argues that the conversion of deep into intermediate water which is needed to provide the water of the 'cold water path' takes place in the Indian Ocean. For our model, this means that a conversion about 3.2 Sv is needed if we assume that all the water that flows westward south of Africa replaces NADW. The value of 3.2 Sv is obtained by subtracting the Bering Strait flow and the Agulhas leakage from the total southward flow at 32^o S in the South Atlantic (=11.3-1.4-6.7). The meridional overturning in the Indian Ocean (Figure 12b) is consistent with this picture since there is a zonal-mean northward flow of 3.2 Sv that upwells from below 1500 m. Significant ventilation in the deep layers seems to occur only south of 10^o N with very little upwelling from the deep ocean to the surface at the equator.

The model simulates a tongue of AAIW, though with a saline bias of 0.1 to 0.2 psu and more small-scale patterns than the climatological data. The upper salinity-minimum water is formed in the model as a result of vigorous overturning along the path of the Agulhas Current and the ACC. These currents transport warm water to higher latitudes in particular where they bend poleward due to topographic influences near the Kerguelen Plateau/Central Indian Ridge at 60^o E (Figure 26a). The water is cooled in austral winter along its poleward path until it has become dense enough to overturn (Figure 26b). Note that in the model simulation which is forced by a heat flux pattern that is relatively zonal, it is the SST relaxation that provides the anomalous heat loss (Figure 7). Figure 26c shows the salinity on a zonal section at 53^o S along the zonal axis of the region with strong convective overturning. While the western basin, west of 60^o E, is stably stratified by the salinity gradient, east of 60^o E, the surface water is homogenized to progressively deeper levels along the flow path. The newly formed fresh water is advected northwestward with the subpolar gyre (Figure 26d). A similar salinity pattern is found in the Levitus climatology (1994) in 800 m (not shown). This picture of AAIW formation is more consistent with the traditional one of crossfrontal mixing and subsequent subduction than that found in the South Atlantic and Pacific, which is characterized by coastal downwelling.

Below the AAIW, the core of the CDW is seen in Figure 25c. It is only slightly too saline, however, it flows at too shallow a level due to the warm bias. This CDW is not upwelled in the Southern Ocean to the degree indicated in the climatology.

The mean barotropic streamfunctions for February and August (not shown) reveal significant seasonal variations in the tropical and subtropical Indian Ocean. The western boundary return flow computed from the zonal integral of the wind stress curl at 32^o S is -63 Sv in August and only -30 Sv in February. The maximum simulated transport of the Agulhas Current differs only by 10% in the two months, however, the shape of the subtropical gyre changes considerably with a much stronger northward interior flow in the eastern Indian Ocean in August. Associated northward excursions of the streamlines over the Central Indian Ridge result in a northward shift of the gyre axis. This shift has been found by Stramma and Lutjeharms (1997) in their investigation of the subtropical gyre based on historical hydrographic data. The SEC is also shifted to the north by about 10^o in August relative to February. The IT is twice as strong in September, when it attains its seasonal maximum, as in February when the throughflow is at its minimum (19 Sv and 9 Sv respectively). This seems to agree well with measurements reported by Fieux et al. (1996). They obtained 18.6 ± 7 Sv in August. In February, however, their flow was directed to the east while the simulated monthly mean flow is always into the Indian Ocean. The seasonal range of the flow through the Mozambique Channel is smaller. It is increased by 70% in September relative to February (12/7 Sv). The fluctuations of the IT and of the transports through the Mozambique Channel vary in phase with a two month time lag to the zonal integral of the wind stress curl at 32^o S in the Indian Ocean.

The net mean simulated IT is -13.5 Sv. Macdonald (1993) and Macdonald and Wunsch (1996) could not arrive at constraints for the IT with inverse models. Transports between 0 and 20 Sv were consistent with their model constraints. There is thus still considerable uncertainty about the mean magnitude of the throughflow. The simulated mean meridional velocity in the Indonesian Passage is shown in Figure 27. The flow is concentrated in the western part of the section in the upper 200 m. Observational evidence suggests that the IT is primarily derived from North Pacific water (Gordon 1995). In the model simulation, the influence of the saline South Pacific water, which should to a large extent retroflect north of New Guinea at about 140^o E, is too strong. While the salinity in the western tropical Pacific is well reproduced in the upper 250 m, the simulated salinity in the Indonesian Seas and the Indian Ocean is too high (Figure 28). Rodgers et al. (1999) have shown that details in the land/sea mask of the model in the Indonesian Seas have a large influence on the origin of the throughflow waters.
Also, the monsoon precipitation in this region is underestimated in the atmosphere model (Roeckner et al. 1996). In addition, the freshening of the surface waters of the Indonesian Seas by precipitation does not seem to effectively penetrate to greater depths. Vertical and horizontal diffusion in these shallow seas is presumably underestimated since mixing by tidal currents is not included in the model physics. Schiller et al. (1998) have shown that an empirically based representation of tidal mixing in the Indonesian Seas causes a more realistic transformation of water masses and affects the Indian Oceans subsurface temperature and salinity. The underestimated precipitation being too strongly surface trapped in HOPE-G can only partly be compensated by the freshwater fluxes that correspond to the SSS relaxation. As a consequence, the simulated salinity in the Indonesian Seas is too high below the surface (Figure 28

b and c). The underestimation of the Indian summer monsoon precipitation can also be blamed for the too high salinity in the Arabian Sea and the Gulf of Bengal.

The IT crosses the Indian Ocean at 5^o S to 10^o S in the southern limb of the cyclonic southern tropical gyre (Figure 28a). At the Madagascar or African coasts, a part of this flow turns to the south while the rest continues northward as the western boundary current of the gyre, the East African Coastal Current (EACC).
The surface layers of the tropical and northern Indian Ocean are strongly influenced by the seasonally varying atmospheric monsoon circulation. In northern summer, the Southwest Monsoon season, the EACC extends across the equator and feeds into the northward Somali Current (Figure 29a). There is a double gyre structure simulated off the African coast with centers at 2^o N and 5^o S. After separation from the coast, the Somali Current feeds into the eastward zonal flow south of India, the Southwest Monsoon Current (SWMC) which constitutes the northern limb of the tropical gyre in the summer monsoon season. The anticyclonic circulation in the Gulf of Aden and the Arabian Sea also finally feeds into the SWMC. While the currents are coherently eastward north of the equator, there are several reversals of the zonal flow between the equator and 10^o S with considerable zonal asymmetry. In the western half of the basin, there is a strong concentrated eastward jet at the equator, the Wyrtki jet (Wyrtki 1973).
In northern winter, driven by the Northeast Monsoon, the circulation north of the equator reverses and is westward south of India. When this current, the Northeast Monsoon Current (NEMC), arrives at the African coast, it turns to the south into the Somali Current which flows southward along the coast in this season. At 5^o S, the Somali Current meets the EACC, and both currents turn to the east and feed into the South Equatorial Countercurrent.
The simulated surface circulation in the northern Indian Ocean compares well with that summarized by Schott et al. (1994) with the exception of the circulation in the western Bay of Bengal during the summer monsoon, which is northward in their description.

Zonal equatorial currents during the mature phases of the monsoon seasons are shown in Figure 30. The currents almost completely reverse down to 300 m. Figure 30 also contains the simulated volume transports of the individual current branches. These values are compared with those from direct observations in Table 3 on page 41. With regard to the strong spread of observational results, the simulated transports seem to be reasonably well reproduced.

3.3 Pacific Ocean

It was shown in Section 3.2 that the model quite well reproduces the observed meridional heat transport in the Indian Ocean. The same holds for the Pacific Ocean (Figure 11c). The simulated transport is in good agreement with the results of Macdonald and Wunsch (1996), except at 28^oS, where the model value is slightly above their upper errorbar. The meridional heat transport curve of the Indo-Pacific

Ocean (not shown) is very similar to that simulated with the 0.5^{o}x0.5^{o} model by Semtner and Chervin (1992). However, their absolute values are slightly smaller.

The meridional streamfunction of the Pacific Ocean is shown in Figure 12c.
There are 7 Sv inflow of AABW below 3500 m. This water is formed in the Ross Sea (Figure 13). It flows northward in slope currents in the deep basins of the western Pacific, though not always in western boundary currents (Figure 31). The main flow passes through the Samoan Passage east of Fiji (represented as a seamount at 17^{o}S /180^{o}E). At and north of the equator there are several branches which separate from the main flow and invade the central deep basins with a predominantly zonal direction. The deep circulation described by Schmitz (1996) is very reminiscent of the circulation pattern of Figure 31. North of 25^{o} N, the simulated abyssal flow is very weak and anticyclonic along the periphery of the basin (not shown). The structure of the flow here is a subject of controversy in the observational literature (Schmitz 1996). The return flow of the abyssal flow is between 3500 to 1800 m (Figure 12c) along the continental slope of southeast Asia, Australia, and New Zealand (Figure 31).
The deep Pacific seems to be effectively ventilated since the simulated temperature is rather too cold by about 0.2^{o} C in the North Pacific to 0.6^{o} C in the southeast. Since bottom water formed in the southern hemisphere is generally too fresh there is also a fresh bias in the deep Pacific Ocean (Figure 15). South of Australia the temperature error (difference to the Levitus climatology) becomes positive and increases towards the Indian Ocean. As noted above, the deep Indian Ocean is mainly ventilated by Weddell Sea bottom water and thus has a warm bias. Accordingly, the small salinity error in the deep Indian Ocean is rather a consequence of error compensation.
The deep flow of the model can be related to the tracer distributions on a zonal section at 10^{o} N as described by Wijffels et al. (1996). The deep northward flow below 3500 m in the model which has maximum speed at 175^{o} W (Figure 32) is consistent with the low silica observed at that position, while the broad southward flow above 3500 m in the east occurs at the depth of the North Pacific Deep Water silica maximum. The 6 Sv northward flow of AABW through this section also compare well with the 8 Sv obtained by Wijffels et al. (1996), as does the simulated northward heat transport (Figure 11c) which is 0.7 ± 0.5 PW according to Wijffels et al. (1996).

Note that the meridional overturning displays no upwelling at the equator from depths greater than 1700 m (Figure 12c). Instead, all bottom water leaves the Pacific Ocean below 1700 m, i.e. below the intermediate water. This is in agreement with the observed distribution of silica and radiocarbon data which do not support upwelling from the deep ocean to the surface in low latitudes (Toggweiler and Samuels 1994). The strength of the bottom-to-deep water conversion, however, which is about 7 Sv in the model, is weaker than the 10 Sv to 20 Sv estimated the from hydrographic data by Schmitz (1995). The upwelling of 4 Sv of intermediate water (below 750 m) to the surface between the equator and 15^{o} N, however, fits to his summary picture of the interbasin-scale thermohaline circulation.

AAIW formation in the model can be located east of New Zealand at the confluence of the northward bending fresh ACC and the southward flowing current east of New Zealand (Figure 36b). The fresh water is subducted (Figure 33a) and advected first eastward and then northwestward with the South Pacific subtropical gyre (Figure 33b). This process is similar to that of the AAIW formation in the South Atlantic in the confluence zone of the Malvinas and Brazil Currents. A second region with formation of AAIW is found southwest of Cape Horn. This is also a region with vigorous subsurface winter overturning and subduction of fresh water at the coast (Figure 33a). Formation of low-salinity AAIW off southern Chile in an OGCM has already been described by England (1993). The formation rate of low-salinity AAIW in HOPE-G is too weak in the Pacific, which is reflected in the simulated zonal-mean salinity distribution (Figure 38c/d).

The low-salinity signal of the North Pacific Intermediate Water (NPIW) is also too weak. This water has its origin in the Okhotsk Sea, the Bering Sea, and the Gulf of Alaska. It is advected east- and southward with the subtropical gyre both in nature and in the simulation (Figure 34a/b). The locations of minimum salinity are reproduced by the model, however, there are patches of increased salinity in the central Sea of Okhotsk and the Bering Sea, which have no counterpart in the climatology. These patches originate from brine released during the wintertime sea-ice growth. The water is flushed out in summer only along the peripheries of the basins or is diluted by continental runoff. There are a number of reasons potentially responsible for this misrepresentation of the salinity distribution in the model. One reason can be an inappropriate representation of haline rejection which is distributed over the upper two ocean layers. Too weak diffusion due to the missing tidal friction might degrade the situation. Secondly, while the simulated water is too fresh in the Yellow Sea and the Sea of Japan, it is too saline in the western Sea of Okhotsk where the NPIW originates in the model. The runoff is predominantly into the Yellow Sea and might be overestimated there at the expense of that into the Sea of Okhotsk, and the missing connection between these seas might be another reason for the changing sign of the salinity error there.
The NPIW is not efficiently transported downward by diffusion in the model. This is demonstrated by Figure 35 which shows the simulated and observed salinity on a zonal vertical section that cuts the centre the North Pacific subtropical gyre. In the upper ocean in the east, the salinity-minimum water is efficiently transported west- and downward, but instead of sinking to a depth of 600 m it remains at a depth of about 200 m. It seems as if the horizontal diffusivity is underestimated. This is also supported by the overestimated horizontal gradients in the west of the section. The isopycnals in the east are sloping, and thus a better reproduction of the NPIW would presumably be achieved with isopycnal diffusion with large isopycnal mixing coefficient (England 1993).

Figure 36a shows the circulation in the upper 190 m of the North and South Pacific outside the tropics. It shows most of the known large-scale circulation features, i.e. the NEC (the southern limb of the North Pacific subtropical gyre), the Kuroshio (western boundary return flow of the subtropical gyre) with a well-defined recirculation cell, a cyclonic subpolar gyre in the western North Pacific, and an Alaska Cur-

rent in the eastern North Pacific. It does not show, however, an Oyashio Current which is distinguishable from the Kuroshio Current. Instead, both the Kuroshio and Oyashio Extensions form a broad eastward flow between 45^o N and 35^o N. The model transport of the Kuroshio/Oyashio is 57 Sv of which 38 Sv can be attributed to the Sverdrup interior flow. In the eastern North Pacific, a California Current is simulated near the coast of North America.

In the South Pacific (Figure 36b), the subtropical gyre is less well-defined, the zonal currents change direction several times in the west. This, however, seems to be supported by observations (Tabata 1975; see also Figure II-25 of Schmitz 1996). As is the case for the North Pacific, the major current systems are reproduced. The East Australia Current (EAC) with a mean transport of 14.3 Sv shows a pronounced recirculation. The Sverdrup transport at 30^o S is 36 Sv. If the simulated transport of the EAC is to be related to the Sverdrup interior flow one has to account for the 1.4 Sv outflow through the Bering Strait and the 13.5 Sv IT. New Zealand disturbs the usual north-south symmetry of the subtropical gyres. From the southeastern tip of Australia to the northern tip of New Zealand flows the Tasman Current. Following topographic contours it turns south to meet a northward flowing branch of the ACC. In the confluence zone of the two currents, AAIW is formed.
The model's Peru Current extends from 45^o S to 17^o S with a large westward excursion at 25^o S. There is an undercurrent beneath it which transports warm light water southward and has been diagnosed by England et al. (1993) to play an important role for the formation of AAIW off southern Chile.
The simulated transports of the currents are summarized in Table 4 on page 42, together with some values found in the literature. Overall, in view of the large range of values derived from observation and the relatively coarse resolution of the model, the observations are reasonably well reproduced.

The meridional velocity through 32^o S is not shown for the Pacific. For the sake of completeness, however, the simulated transport through the section is given in Table 5 on page 43 for the same water mass classes as was discussed for the Indian Ocean.

Zonal annual-mean equatorial currents are shown in Figure 37. Overall, the seasonal variations are much weaker than those in the Indian and Atlantic Oceans, and thus only the annual mean is shown here.
Figure 37 can directly be compared with the representation of Wyrtki and Kilonsky (1984) of annual-mean hydrography and geostrophic currents on the same section. The model results show no bias, except that the simulated annual-mean EUC extends to larger depths. A westward flow at the equator below 300 m as displayed by Wyrtki and Kilonsky (1984) is not present in the simulated annual-mean state at this longitude. It is, however, seen in the February mean 13^o further east (not shown).

A comparison of the simulated and observed zonal-mean temperature and salinity patterns shows that the temperature bias is small at low and mid latitudes, generally below 1^o C. Below 2000 m and in the Southern Ocean, the simulated temperatures are slightly too cold by about 0.5^o C. The largest temperature errors in the North Pacific above 2000 m are caused by the inefficient subduction of cold and fresh

NPIW, as discussed above.
The largest salinity errors also occur in the intermediate water masses, the NPIW and the AAIW (0.2 to 0.4 psu). The simulated deep and bottom water is less salinity stratified than the observed. Since the AABW is formed with a fresh bias of about 0.1 psu, while the intermediate water have a saline bias, the deep ocean below 1000 m is filled with water of similar salinity from the north and the south. A saline signal is given by the CDW of Atlantic origin.

3.4 High latitudes

Deep-water formation processes at high latitudes are important for the ventilation of the entire deep world ocean. The formation of sea ice can have a strong influence on the characteristics of the deep water. The density of sea water near the freezing point is dominated by its salinity. Since the salinity of sea ice is generally much lower (ca. 5 psu) than that of the water it is formed from, the freezing or melting of sea ice leads to an increase or decrease of the salinity, and thus density, of the ambient surface water. Thus, in ice regions, it is the salinity that primarily determines the stability of the upper water column.

In long-term integrations of ocean models, modelers frequently use so-called relaxation techniques to prevent the ocean from drifting away from the observed climatology. Such techniques are also applied for SST and SSS in the integration described here. However, since thermodynamic and dynamic changes of the sea ice are prognostically determined and the change of upper-ocean salinity by freezing and melting of sea ice is accounted for, SSS relaxation is not applied in ice regions in order to not disturb or weaken the seasonality of the salinity stratification due to ice formation. Ice regions in this respect are defined by the SST of the AMIP climatology (Gates 1992). No SSS relaxation is done in a gridpoint where the observed SST of the actual month is below -1.79^{o} C. Since the 'ice edge' defined in this way undergoes seasonal variations no spurious artificial fronts are created. By this formulation, freshwater flux corresponding to SSS relaxation is restricted to the Norwegian Sea and some coastal regions in summer in the Arctic (Figure 8). SST relaxation is done everywhere but with observed SST at or above freezing point only. Thus, in the Arctic, there is essentially no heat flux due to SST relaxation away from coastal points and outside the Norwegian Sea (Figure 7). In the Southern Ocean, though, large negative fluxes occur in the Ross and Weddell Seas, since there the sea surface is warmed to above freezing point by vertical mixing with the warm CDW when the water is overturned by convective adjustment. It is then nudged back to the observed value.

3.4.1 Southern Ocean

It is believed that in the Southern Ocean, the AAD/BW is formed through subsurface mixing of warm saline CDW with cold shelf water whose salinity is enhanced by brine release during freezing of sea ice. Driven by its density, the shelf water flows down the continental slope and entrains ambient warmer and lighter water (Gordon et al. 1993). Toggweiler and Samuels (1995) summarized observational evidence

for the degree of salinification the water on the Ross Shelf experiences due to ice growth. The net salinification, estimated from the salinity difference between the water that enters and leaves the shelf, amounts to 0.15-0.2 psu. Assuming an atmospheric freshwater input of 15 cm a^{-1}, 36 cm a^{-1} glacial meltwater input, and a residence time of 6 years for the water on the shelf, Toggweiler and Samuels (1995) concluded that the salinification of the shelf water due to ice growth is equivalent to a freshwater flux of about -84 cm a^{-1}. The freshwater flux which forced the ocean model described here includes continental runoff but no input from any kind of glacier melt. Table 6 on page 44 lists the zonal mean freshwater input in the 10 grid lines nearest to the Antarctic continent. At 76.7^{o} S, which has sea cells only in the Weddell and Ross Seas, the areal mean flux by atmospheric net precipitation is 15 cm a^{-1}. SSS relaxation adds 2.6 cm a^{-1}. Since there is no glacier melt in the model, the salinification effect needed if one follows the arguments of Toggweiler and Samuels (1995) corresponds to a net ice-growth freshwater effect of -0.84+0.36-0.026=-0.51 cm a^{-1}. The net ice growth simulated by the model corresponds to -53.0 cm a^{-1} which is remarkably near the value of Toggweiler and Samuels (1995). The mean ice growth along the coast, amounts to -43 cm a^{-1}. Moving offshore, the atmospheric fluxes increase to about 50 cm a^{-1}, while the net ice growth decreases until, at 62.8^{o} S, it is changed into a net ice melt. In parallel, the freshwater flux arising from SSS relaxation increases to 38 cm a^{-1}. The offshore ice melt does not seem to be sufficient to maintain the fresh characteristics of the surface water offshore.

From a comparison with observed data it is seen that a deficit of atmospheric freshwater flux of this magnitude can not be maintained. The simulated ice concentration (Figure 39a) provides a hint that another process which has the potential of spuriously increasing the SSS is active in the model. In the Weddell and Ross Seas, the ice concentration is rather low, regionally below 20%. These regions of low ice concentration coincide with those where enhanced vertical mixing by convective adjustment has been diagnosed (Figure 13). A comparison of the observed and simulated zonal-mean temperature and salinity distribution off the Antarctic coast in all three ocean basins confirms that vertical mixing is too strong in the simulation (Figure 21, Figure 25, Figure 38) in particular in the Atlantic and Pacific Oceans. Martinson (1990) has investigated vertical mixing processes in the Southern Ocean. He showed that the weak stratification in the open ocean is stabilized by the warm CDW which underlies the surface water. When the upper ocean becomes unstable due to brine release by sea-ice growth, the CDW is mixed upward and melts the ice that has just formed. The freshening effect in the surface water restores the upper-ocean stability. Thus net ice growth is expected to mainly occur on the shallow shelves where the warm-water reservoir is more limited. Only there can a salinification by net sea-ice growth lead to the formation of saline cold water dense enough to flow below the CDW and take part in the formation of AAD/BW.

In ocean models with horizontal grid scales such as the one presented here, Antarctic shelves are only crudely resolved. As a consequence the net ice growth rapidly decreases towards the north (Table 6 on page 44). There, open-ocean convection triggered by brine release accesses the warm CDW mass. The upward flux of heat is so large that there is even net ice melt regionally (Figure 39b). Martinson (1990) also showed that, with the stratification observed in the Southern Ocean, the open-ocean convection acts

not only as an upward pump of heat but also of salt. The relatively large freshwater flux diagnosed between 68^o S and 57^o S for the SSS relaxation (Table 6 on page 44) can be attributed to the spurious deep-reaching open-ocean convection simulated in the model. Much of the sea ice formed near the coast is already melted in the central Weddell and Ross Seas when moving offshore (Figure 39d), and is not available for melt farther offshore.

In order to limit the freshening effect of open-ocean convection on the deep water, 30% of the brine released during ice growth is transferred to the second ocean layer. Legutke et al. (1997) have shown how this can improve the simulated profiles of temperature and salinity in the Weddell and Ross Seas. The profiles of the present run are shown in Figure 39c. Those of the Ross Sea are better reproduced than those of the Weddell Sea. In the Ross Sea the observed ice cover starts to open up in October/November and freezes over in March/April (Gloersen et al. 1992). The ice pattern shows large deviations from zonality indicating that oceanic heat fluxes are important and perhaps open-ocean convection plays a larger role there than elsewhere in the Southern Ocean. This might explain why the simulation, where open-ocean convection plays a major role, is more successful in the Ross Sea. While some of the subsurface temperature maximum of the CDW is maintained there, it is totally eroded in the Weddell Sea. In the Ross Sea, the deep ocean is cold and fresh, the convection seems to reach to the bottom frequently. In the Weddell Sea, by contrast, it seems at most times to reach only 2000 m. The deeper layers are not ventilated enough. As was said before, a proper simulation of the formation of AAD/BW as it is observed requires an appropriate resolution of the Antarctic shelves and slope-flow processes. Both are not guaranteed with the present model.
The biases of the deep simulated temperature and salinity in the Weddell and Ross Seas match those further north in the Atlantic and Pacific (Figure 15). All deep oceans are too fresh in the southern hemisphere. In the Atlantic Ocean the bottom salinities are too low south of the equator only. The deep North Atlantic is flushed by the NADW with a positive salinity bias. Bottom temperatures are too high in the entire Atlantic in accord with the positive temperature bias of the NADW and the Weddell Sea deep and bottom water.

The seasonal cycles of all heat fluxes that contribute to the temperature change of the uppermost ocean layer in the observed climatological ice region are shown in Figure 40d. The annual mean of the oceanic heat flux in this layer, provided by convective adjustment amounts to 85 Wm^{-2}, that by vertical diffusion is 19 Wm^{-2}, and that by the atmospheric fluxes is -96 Wm^{-2} (upward fluxes are negative.). There is an effective cooling of the upper layer associated with penetration of solar radiation into deeper layers of -8 Wm^{-2}, which is not included in the figure. The melting of sea ice is thereby delayed in summer. The simulated values are well above estimates based on measurements, which are about 30 Wm^{-2} for both the atmospheric and the oceanic heat flux (Gordon 1981). Note however, that the simulated values include the fluxes near the ice edge which are generally believed to be higher than those well within the ice region. Also the estimates of Gordon (1981) give lower limits for the oceanic heat flux since it is

obtained as a residual flux needed to melt the sea ice in summer. A seasonal warming of the mixed layer or the melting of icebergs or ice sheets is not considered. The global meridional heat flux across 60^{o} S simulated by HOPE-G is 1 PW (Figure 11d). This fits the results of Trenberth (1979), but lies above other estimates by a factor of 2 (Gordon 1981). The model heat transport is equally partitioned between advective and diffusive fluxes.
The phase of the seasonal cycle of sea-ice extent is well reproduced. An excessively large spring and summer surface melt contributes to an underestimated ice cover in summer. Only very little ice remains, mainly to both sides of the Antarctic Peninsula (not shown). Though the main mass of sea ice in the figures of Gloersen et al. (1992) is found at the same position in austral summer, it seems to be underestimated. This holds also for the winter ice thickness (Figure 40b).

The ACC is weaker than observed. It dropped from about 140 Sv at the start of the integration to its steady state value of 91 Sv (Figure 13) and is about 30% below estimates from oceanographic observation (Whitworth and Peterson 1985). Part of this can be attributed to the underestimated surface winds in the atmosphere over the SO.
It was shown that formation of AAIW takes place in confluence zones of the ACC and warmer saltier southward-flowing currents. The weak simulated ACC can be responsible for the saline bias in this water mass. Sensitivity studies show that a relatively small increase in the strength of the windstress and thus of the ACC can, on long time scales, result in a significant decrease of the salinity of the AAIW. Fluctuations of the ACC transport in the integration occurred not only because of the 15-year forcing but also on longer time scales due to internal dynamics. They are negatively correlated with the fluctuations of the Southern Ocean ice volume (not shown).

3.4.2 Arctic Ocean

The sea-ice cover of the northern hemisphere is much better reproduced than that of the Southern Ocean. In September, when the sea-ice extent assumes its seasonal minimum, the ice concentration is above 95% north of Greenland and the Canadian Archipelago (Figure 41a). The Barents Sea is almost free of ice, which is also in agreement with the mean distribution derived from the SMMR data by Gloersen et al. (1992). The ice in the Kara and Laptev Seas is slightly more concentrated than the observations show but also decreases towards the coast. The concentration off the Canadian coast is also slightly higher than that observed. Both the simulation and the observations have high concentrations even at the coast on the East Siberian shelf and near Severnaya Semlya. Also, the concentration in the Greenland Sea and north of the Bering Strait agrees well with the SMMR data. In February the ice cover is compact everywhere in the Central Arctic with the exception of the southern Barents Sea. While the observed ice edge in the Greenland Sea extends to the southern tip of Greenland, in the simulations it reaches to the Denmark Strait only. The Hudson and Baffin Bays are ice covered in both the observations and the model results. The overestimation of the ice extent in winter (Figure 41c) is mainly due to the fact that the ice edge

extends too much south in the North Pacific. Otherwise the seasonal cycle is well reproduced. The sea ice in the northern hemisphere is much less sensitive to the state of the ocean below, due to the strong salinity stratification which prevents excessive overturning. The diffusive vertical heat flux is almost as large as that caused by convective adjustment (Figure 41d). This is in contrast to the simulation in the Southern Ocean. Again the contribution by horizontal advection and diffusion is small. The annual mean oceanic heat flux is 9.4 Wm^{-2}, which is above the value of 2 Wm^{-2} often cited for the inner ice cover. Note again that the value given for the simulation includes fluxes at the ice edge which can be orders of magnitudes above those estimated for the strongly stratified Central Arctic.

Figure 42a shows the simulated annual-mean sea-ice thickness distribution. The average value seems to be slightly above the value of 2.7 m obtained by Thomas et al. (1996) with a thermodynamic ice-growth model which uses satellite ice concentrations and buoy velocities. The thickest ice is simulated in the Siberian sector of the Central Arctic with only moderate increases of thickness north of Greenland and Canada. This is in contrast to the distribution derived from observations by Bourke and Garrett (1986) which shows a clear maximum in the thickness distribution off northern Greenland and the Canadian Archipelago. Such a thickness has been simulated by Hibler (1979) with measured geostrophic wind data from 1965. However, with data from other years, Flato and Hibler (1995) obtained a distribution which is in many respects similar to the one presented here.

The simulated thickness distribution is largely determined by the wind-forced sea-ice velocity field. It shows (Figure 42b) the well known Beaufort gyre north of the Bering Strait and a large convergence zone in the Siberian Sea which caused the thickness maximum there. In the Kara and Laptev Seas, the ice drifts offshore leading to thin ice near the coast and to large annual net ice-growth rates (Figure 42c). There is no net ice melt in the Central Arctic except near the Bering Strait in agreement with the results of Thomas et al. (1996). The ice drifts southward through the Fram Strait and melts when it encounters the warm Norwegian Sea water. The transport through the Framstrait is 0.032 Sv, at the lower end of the range given by Thomas et al. (1996). Net ice melt is also simulated in the North Pacific, the southern Hudson Bay, and the Labrador Sea. The ice growth in the Central Arctic counteracts the net freshwater input by continental runoff and precipitation-evaporation which is 30 and 15 cm a^{-1} respectively. A strong halocline is simulated by the model (Figure 42d), though it is not as strong as the observed. In the deep ocean the water is slightly too fresh. Since it is also too warm, it is too light. Otherwise, the shape of the temperature profile is well reproduced though with the salinity maximum of the Atlantic water above the observed level. The deep water of the Central Arctic is one component of the water that flows over the Greenland/Scotland Ridge and takes part in the formation of the NADW. The light bias of this water mass is presumably one reason for the weak overturning in the North Atlantic.

4 Summary and discussion

The HOPE-G climatology obtained in a 2000-year spin-up experiment is described. HOPE-G differs from an earlier version (Frey et al. 1997) in that a sea-ice model has been included in order to account for the influence of sea-ice processes on water mass formation. The ocean is forced by daily fluxes and near-surface variables from a 15-year integration of the atmosphere general circulation model ECHAM4. In the northern and southern hemisphere ice regions, which are diagnosed from the same climatological monthly AMIP SST which have been used as lower boundary conditions during the production of the forcing fields, the fluxes into the ocean are calculated with bulk formulas. The calculation is done separately, with the appropriate bulk coefficients, over the ice-covered part of the gridcell and over ice-free water. Outside the ice regions, the ocean is forced by the momentum, freshwater, and heat fluxes calculated in the atmosphere. No relaxation of SSS to observations is done in ice regions. Thereby, it is guaranteed that the vertical fluxes of freshwater in the mixed layer under ice are exclusively controlled by the atmospheric and oceanic fluxes and by local changes of ice volume. Outside the ice regions, both SSS and SST are nudged to observations, partly in order to counteract model deficiencies, and partly in order to correct the model-generated forcing data.

Of course, the daily to 15-year fluctuations of the forcing data are reflected by the simulated ocean variables. However, the model is in a quasi-steady state at the end of the integration if 15-year mean variables are considered. Internal low-amplitude and low-frequency fluctuations are still present, though. They are most obvious in the Southern Ocean, in variables which are directly involved in the Antarctic Bottom Water formation such as sea-ice volume, potential energy released by convective adjustment, or deep-ocean salinity.

The simulated climatology is compared with observed climatological temperatures and salinities, with patterns of ocean currents and transports obtained from direct measurements, and with other model results.

The main water masses observed in the world ocean are also found in the model.
The North Atlantic Deep Water has a warm and saline bias, which has the potential of being at least partially at the base of most of the model deficiencies. This points to the fact that the North Atlantic Deep Water in the real ocean is not formed directly at the surface by exchange with the atmosphere. Subsurface mixing processes which are not appropriately parameterized in the model also play a crucial role.
Mauritzen (1996) has derived a revised circulation scheme for the North Atlantic/Arctic Ocean in which the Norwegian Atlantic Current becomes gradually dense by heat loss to the atmosphere. The modified water returns southward as distinct layers of the East Greenland Current. This scheme does not invoke deep convection in the Iceland and Greenland Seas as did previous theories of North Atlantic Deep Water formation. In agreement with this scheme, the model presented here simulates loss of potential energy by overturning in the Norwegian Sea. In the Greenland Sea, the strong salinity stratification prevents

overturning. The surface water in the Norwegian Sea is cooled by the atmospheric fluxes. The net freshwater flux is downward there. The relaxation fluxes counteract with warming and evaporation, since the model grid resolution in the North Atlantic does not allow the North Atlantic Current to enter the Norwegian Sea with the observed warm and salty surface characteristics. In addition, because of the small number of gridcells in the Greenland/Norwegian Sea, the horizontal mixing of fresh water from the Greenland Current into the upper water of the Norwegian Sea is too large. The Atlantic Water north of the Greenland/Scotland Ridge is thus too fresh at the beginning of its way through the Arctic basin and the Greenland Sea. More serious is the warm bias of the North Atlantic Deep Water. The Atlantic water is already too warm below 500 m when it has crossed the Greenland/Scotland Ridge northward. It keeps its warm bias on its way through the Arctic. Processes that take place in the Arctic do not seem to be at the base of the warm bias, since the temperature error is slightly decreased there. Also, the simulated heat loss from the deep ocean to the ice cover or atmosphere is larger than commonly assumed.

The deep water formed north of the Greenland/Scotland Ridge is thus too warm and too fresh. By contrast, the water in the Northern North Atlantic is too salty. Since the latter dominates the salinity characteristics of the North Atlantic Deep Water, it is too salty as well. Much of the misrepresentation of the North Atlantic Deep Water characteristics can be related to the coarse grid resolution in high latitudes. An improvement can also be expected by an inclusion of some kind of bottom boundary layer (Beckmann and Döscher 1997) in order to reduce the vertical mixing when the water has to cross a sill or descend down other topographic features. In these situations, vertical mixing is usually too large in z-level models. A boundary layer parameterization can also help to improve the influence of the Mediterranean water on the North Atlantic Deep Water in the model. In addition, the simulated characteristics of Antarctic Deep and Bottom Waters can profit from a bottom boundary layer formulation. These water masses contain cold brine-enriched high-latitude shelf water, which is assumed to flow down the continental slope before it mixes with the overlying water masses.

The warm bias dominates the density error of the North Atlantic Deep Water and it is thus slightly too light. This has a weakening influence on the strength of the meridional circulation. The outflow of North Atlantic Deep Water into the Southern Ocean is with 11 Sv near the lower limit of the range of 12 to 15 Sv estimated from observations. The combination of a warm bias with a low overturning in the North Atlantic gives a meridional heat transport in the North Atlantic, which is clearly underestimated, a deficiency that is shared with many other ocean models, in particular those with coarse resolution in high latitudes. However, the meridional heat transport simulated in the other ocean basin is in good agreement with that obtained from hydrographic measurements.

The North Atlantic Deep Water can be traced to flow southward into the Southern Ocean and then eastward around Antarctica. Along its path, it is transformed to Circumpolar Deep Water by freshening and cooling. Since this water upwells near the continental shelf forced by Ekman pumping, its warm bias increases the oceanic heat flux into the mixed layer in the Southern Ocean, which is to a large extent

responsible for the low sea-ice volume simulated in southern high latitudes. In addition, with the layer thicknesses used here, the convective-adjustment process seems to be inappropriate for ice regions. Too much fresh meltwater is mixed downward, and as a result, a fresh bias is simulated in the Antarctic Bottom Water.
The convection takes out a part of the excessive heat that is stored in the Circumpolar Deep Water, and thus partially compensates for the warm bias of the North Atlantic Deep Water. The transports of deep overturning cells of Antarctic Bottom Water lie within the (admittedly large) range deduced from observations. Judged by net ice-growth rates near the coast, the ice production seems to be sufficiently large in view of the freshwater fluxes which enter the mixed layer from the atmosphere.

The picture of the simulated 'conveyor' circulation which is derived from variables such as northward heat transport, vertical overturning, and water mass transport through zonal sections, seems to favor the 'warm water path' south of Africa. There, 6.7 Sv enter the South Atlantic from the Indian Ocean. However, not all of this is warm upper-ocean water. The inflow also contains low-salinity intermediate water. It is not clear, how much of this water is of South Atlantic origin and just performs a recirculation loop in the Indian Ocean.

The formation of low-salinity Antarctic Intermediate Water and North Pacific Intermediate Water is another critical aspect of ocean modeling. The Antarctic Intermediate Water in the Atlantic sector of the Southern Ocean is well reproduced if judged by vertical salinity differences between the Antarctic Intermediate Water and the underlying North Atlantic Deep Water. Formation of Antarctic Intermediate Water is also simulated in the Indian Ocean. In the Pacific Ocean, its fresh signal is too weak. The North Pacific Intermediate Water also has a saline bias. Other model studies have shown that isopycnal mixing with large coefficients can improve this aspect of the simulation, in particular in the Pacific. However, it does not seem to have a large impact on the density distribution, currents, and meridional heat transport (Hirst and Cai 1994, Cummins et al. 1990).

The simulated ocean currents display many features known from observation. This holds for the upper ocean as well as for the bottom flow. Also, mean horizontal transports are well reproduced in view of the large range of values found in the literature. Of course, simulated velocities are much too small since they represent gridcell means which have, in most cases, scales larger than fronts or currents in the real ocean. An exception is the zonal velocity in the tropical oceans, where the meridional grid resolution is highest.

Acknowledgment

We thank Mojib Latif and Keith Rodgers for proof-reading the manuscript. The integration of ECHAM4, by which the atmospheric forcing was obtained, has been undertaken by Monika Esch. Special thank is due to Arno Hellbach, who developed the ocean model postprocessor which helped much preparing the figures. Achim Stössel participated in the sea-ice - ocean coupling.

5 Tables

Table 1 Salinity and Potential Temperature Trends and Errors

Variable	Depth	$\Delta / (90a)$	Error
Potential temp. [^{o}C]	125	$-7.2 \cdot 10^{-4}$	-0.18
Potential temp. [^{o}C]	800	$1.6 \cdot 10^{-2}$	0.92
Potential temp. [^{o}C]	3000	$1.8 \cdot 10^{-3}$	0.1
Salinity [psu]	125	$1.2 \cdot 10^{-4}$	0.12
Salinity [psu]	800	$2.4 \cdot 10^{-4}$	0.19
Salinity [psu]	3000	$-1.5 \cdot 10^{-4}$	-0.04

Table 2 Volume Transport of Currents in the Atlantic Ocean

Current	sim. annual mean*	sim. Feb. mean*	sim. Aug. mean*	obs.*	Reference
SEC(6^oN-11^oS)	-	-8.9	-16.6	-3	Molinari 1982
SEC (subtropical gyre)	-	-12.5	-16.9	-16	Stramma et al. 1990
EUC	-	6.4	9.3	4 - 15	Düing et al. 1975
NECC	-	3.8	14.4		-
SECC	-	0.1	0.1		-
NEUC	-	1.2	-	15	Molinari et al. 1981
SEUC	-	4.2	-	5 - 23	Molinari 1982
Gulf Stream	34.4	-	-		
N. Atl. subpolar gyre	-17.0	-	-		
S. Atl. subtrop. gyre	-25.8	-	-	-76	Peterson and Stramma 1989
ACC	91.0	-	-	120	Whitworth and Peterson 1985
AAD/BW deep over-turning cell	5				
Greenland/Scotland Ridge	8.1 / -9.6	-	-		
outflow of NADW at 30^o S	-11.3	-	-	-12 - -15	Schmitz and MacCartney 1995
max. overturning in the North Atlantic	14.5				
Mediterranean overflow	0.86/ -0.83	-	-	0.90/ -0.86	Bryden and Kinder 1991
WDW formation	4.9	-	-	5	Schmitz 1995
Agulhas leakage	-6.7	-	-	-3 - -14	Peterson and Stramma 1991
Benguela Current	13.2	-	-	18 - 20 13	Stramma and Peterson 1989 Garzoli and Gordon 1996
Brazil (near coast)	4.5	-	-	4 - 11	Peterson and Stramma 1991
Bering Strait	1.4			0.8	Coachman and Aagaard 1988

* in Sv=10^6 m^3 s^{-1}

Table 3 Volume Transport of Currents in the Indian Ocean

Current	HOPE-G*	Observed *	Reference
NEMC (February)	-15.1	-10 - -12	Schott et al. 1994
SWMC (August)	22.6	8 - 15	Schott et al. 1994
Wyrtki Jet (June)	19.0	20 / 14	Wyrtki 1973 / Hastenrath and Greischar 1991
SECC (August)	12.3	5	Hastenrath and Greischar 1991
SEC (August/February)	-21 / -15	-13	Hastenrath and Greischar 1991
EUC (August/February)	- 18.7 / +17.6	-	
Somali C. (August)	27.8	37	Sverdrup transport across 2^{o} N
Agulhas C.	64	60 - 65	Stramma and Lutjeharms 1997
Mozambique Channel	-9.4	-10 / -6	Harris 1972 / Fu 1986
Leeuwin C.	1.1	5 0.7	Smith et al. 1991 / Toole and Warren 1993
W. Austral. C.	8.0		
Indonesian Throughflow	-13.5	0 - -20	MacDonald and Wunsch 1996

* in Sv=10^6 m^3 s^{-1}; months in the first column relate to the simulation

Table 4 Volume Transport of Currents in the Pacific Ocean

	HOPE-G*	Observation*	Reference
Kuroshio/Oyashio Ext.	57	57/22 52	Joyce and Schmitz (1988) Qiu and Joyce (1992)
Subpolar gyre	-11.0		
Alaska Current	-3.2		
Mindanao C.	-21.6	-18	Wijffels et al. 1996
EAC/Recirculation	-14.3 / +4.0	-27.5 / 17.5	Ridgway and Godfrey (1994)
Tasman Current	3.7		
Peru Current	7 .0		
NEC, 137^{o} E	-68.4	-62.3	Qiu and Joyce 1992
NECC, 137^{o} E	38.7	51.5	“
SEC at 140^{o} W	-47.7		
EUC at 140^{o} W	35.8		
AAD/BW deep overturning cell	7		

* in Sv=10^{6} m^{3} s^{-1}

Table 5 Meridional Volume Transport at 32^{o} S

Pot. density	Water mass	Northward*	Southward*	Net
Indian Ocean				
σ_θ < 26.8	SW	21.0	-35.0	-14.0
26.8< σ_θ <27.2	UIW	16.5	-16.6	-0.1
27.2< σ_θ <27.5	LIW	13.5	-14.5	-1.0
27.5< σ_θ <27.7	UDW	16.3	-15.5	0.8
27.7< σ_θ <27.75	LDW	11.4	-10.9	0.5
27.75< σ_θ	BW	1.1	-1.1	0.0
All layers		79.8	-93.6	-13.8
Pacific Ocean				
σ_θ < 26.8	SW	20.6	-15.4	5.2
26.8< σ_θ <27.2	UIW	8.9	-5.3	3.6
27.2< σ_θ <27.5	LIW	9.9	-8.1	1.8
27.5< σ_θ <27.7	UDW	8.7	-9.8	-1.1
27.7< σ_θ <27.75	LDW	5.5	-7.2	-1.7
27.75< σ_θ	BW	7.3	0.0	7.3
All layers		60.9	-45.8	15.1
Atlantic Ocean				
σ_θ < 26.8	SW	9.7	-4.4	5.3
26.8< σ_θ <27.2	UIW	4.9	-2.2	2.7
27.2< σ_θ <27.5	LIW	7.6	-5.5	2.1
27.5< σ_θ <27.7	UDW	2.2	-7.1	-4.9
27.7< σ_θ <27.75	LDW	0.0	-0.2	-0.2
27.75< σ_θ	BW	8.2	-14.5	-6.3
All layers		32.6	-33.9	-1.3

* in Sv=10^6 m^3 s^{-1}

Table 6 Freshwater Flux in the Southern Ocean

Latitude	P-E [cm a^{-1}]	SSS relaxation [cm a^{-1}]	Ice growth [cm a^{-1}]
-51.6	48.0	3.8	1.3
-54.4	50.1	12.0	1.6
-57.2	50.7	28.8	3.5
-60.0	50.3	38.0	5.8
-62.8	52.2	36.6	3.0
-65.6	49.7	35.5	-17.3
-68.4	40.6	30.9	-29.7
-71.2	38.7	16.3	-26.7
-73.9	31.8	2.5	-19.0
-76.7	15.3	2.6	-53.0
Coastal cells	40.6	21.4	-43.4

6 References

Adcroft, A., C. Hill, and J. Marshall, 1997: Representation of Topography by Shaved Cells in a Height Coordinate Ocean Model. Mon. Weath. Rev., 125, 2293-2315.

Bengtsson, L., E. Roeckner, and M. Stendel, 1999: Why is the global warming proceeding much slower than expected? J. Geophys. Res., 104(D4), 3865-3876.

Böning, C. W. and P. Herrmann, 1994: Annual cycle of poleward heat transport in the oceans: results from high-resolution modeling of the Equatorial North Atlantic. J. Phys. Oceanogr., 24, 91-107.

Böning, C. W., W. R. Holland, F. O. Bryan, G. Danabasoglu, and J. C. McWilliams, 1995: An overlooked problem in model simulations of the thermohaline circulation and heat transport in the Atlantic Ocean. J. Climate, 8, 515-523.

Bourke, R. H. and R. P. Garrett, 1986: Sea Ice Thickness Distribution in the Arctic Ocean. Cold Regions Science and Technology, 13, 259-280.

Broecker, W. S., 1991: The Great Ocean Conveyor. Oceanography, 4, 79-89.

Bryan, K. and L. J. Lewis, 1979: A Water Mass Model of the World Ocean. J. Geophys. Res., 85(C5), 2503-2517.

Bryden, H. and T. H. Kinder, 1991: Steady two-layer exchange through the Strait of Gibraltar. Deep-Sea Res., 38, 5445-5463.

Chen, C.-T. and E. Roeckner, 1996: Validation of the Earth radiation budget as simulated by the Max Planck Institute for Meteorology general circulation model ECHAM4 using satellite observations of the Earth Radiation Budget Experiment. J. Geophys. Res., 101, 4269-4287.

Cubasch, U., K. Hasselmann, H. Höck, E. Maier-Reimer, U. Mikolajewicz, B. D. Santer, R. Sausen, 1992: Time-dependent greenhouse warming computations with a coupled ocean-atmosphere model. Climate Dynamics, 8, 55-69.

Cummins, P. F., G. Holloway, A. E. Gargett, 1990: Sensitivity of the GFDL ocean model to a parameterization of vertical diffusion. J. Phys. Oceanogr., 20, 817-830.

Danabasoglu, G. and J. C. McWilliams, 1995: Sensitivity of the global ocean circulation to parameterizations of mesoscale tracer transports. J. Climate, 8, 2967-2987.

Dengg, J., A. Beckmann, and R. Gerdes, 1996: The Gulf Stream Separation Problem. Published in "The Warmwatersphere of the North Atlantic Ocean", ed. W. Krauss; Gebrüder Bornträger, Berlin-Stuttgart, 444 pp.

Drijfhout, S. S., E. Maier-Reimer, and U. Mikolajewicz, 1996: Tracing the conveyor belt in the Hamburg large-scale geostrophic ocean general circulation model. J. Geophys. Res., 101, 22563-22575.

Düing, W., P. Hisard, E. Katz, J. Meincke, L. Miller, K. V. Moroshkin, G. Philander, A. A. Ribnikov, K. Voigt, and R. Weisberg, 1975: Meanders and long waves in the equatorial Atlantic. Nature, London, 257(5524), 280-284.

England, M. H., 1992: On the formation of Antarctic Intermediate and Bottom Water in Ocean General Circulation models. J. Phys. Oceanogr., 22,918-926.

England, M. H., 1993: Representing the global-scale water masses in ocean general circulation models. J. Phys. Oceanogr., 23, 1523-1552.

England, M. H. and V. C. Garcon, 1993: South Atlantic circulation in a world ocean model. Ann. Geophysicae, 12, 812-825.

England, M. H., J. S. Godfrey, A. H. Hirst, and M. Tomczak, 1993: The Mechanism for Antarctic Intermediate Water Renewal in a World Ocean Model. J. Phys. Oceanogr., 23, 1553-1560.

Fieux, M., R. Molcard, and A. G. Ilahude, 1996: Geostrophic transport of the Pacific-Indian Oceans throughflow. J. Geophys. Res., 101(C5), 12421-12432.

Flato, G. M. and W. D. Hibler III, 1995 : Ridging and strength in modeling the thickness distribution of Arctic sea ice. J. Geophys. Res., 100(C9), 18611-18626.

Frey, H., M. Latif, and T. Stockdale, 1997: The Coupled GCM ECHO-2. Part I: The Tropical Pacific. Mon. Wea. Rev., 125, No. 5, 703-720.

Fu, L.-L. , 1986: Mass, heat, and freshwater fluxes in the South Indian Ocean. J. Phys. Oceanogr., 16, 1683-1693.

Garzoli, S. L. and A. L. Gordon, 1997: Origins and variability of the Benguela Current. J. Geophys. Res., 101, 897-906.

Gates, W. L., 1992: AMIP: The Atmosphere Model Intercomparison Project. Technical Report 7, Program for Climate Model Diagnosis and Intercomparison, Lawrence Livermore National Laboratory, L-264, PO Box 808, Livermore, CA, 94550, USA.

Gent, P. R., J. Willebrand, T. J. McDougall, and J. C. McWilliams, 1995: Parameterizing eddy-induced tracer transports in ocean circulation models. J. Phys. Oceanogr., 25, 463-474.

Gent, P. R., F. O. Bryan, G. Danabasoglu, W. R. Holland, W. G. Large, and J. C. McWilliams, 1998: The NCAR climate system model global ocean component. J. Climate, 11(6), 1287-1306.

Gloersen, P., W. J. Campbell, D. J. Cavalieri, J. C. Comiso, C. L. Parkinson, and H. J. Zwally, 1992: Arctic and Antarctic Sea Ice, 1978-1987, Scientific and Technical Information Program, NASA, Washington, D. C..

Godfrey, J. S., 1989: A Sverdrup-model of the depth-integrated flow for the world ocean allowing for island circulations. Geophys. Astrophys. Fluid Dyn., 45, 89-112.

Gordon, A. L., 1981: Seasonality of Southern Ocean Sea Ice. J. Geophys. Res., 86(C5), 4193-4197.

Gordon, A. L., 1986: Inter-ocean exchange of thermocline water. J. Geophys. Res., 91(C4), 5037-5046.

Gordon, A. L., R. F. Weiss, W. M. Smethie, and M. J. Warner, 1992: Thermocline and intermediate water communication between the South Atlantic and Indian Oceans. J. Geophys. Res., 97, 7223-7240.

Gordon, A.L., B. A. Huber, H. H. Hellmer, and A. Ffield, 1993: Deep and bottom water of the Weddell Sea's western rim. Science, 262, 95-97.

Gordon, A. L., 1995: When is 'appearance' reality ? Indoneasian Throughflow is primarily derived from North Pacific water masses. J. Phys. Oceanogr., 25, 1560-1567.

Harris, T. F. W., 1972: Sources of the Agulhas Current in the spring of 1964. Deep-Sea Res., 19, 633-650.

Hasselmann, K., 1993: Optimal fingerprints for the detection of time dependent climate change. J. Climate, 6, 1957-1971.

Hastenrath, S., 1982: On meridional heat transports in the world oceans. J. Phys. Oceanogr., 12, 922-927.

Hastenrath, S. and L. L. Greischar, 1989: Climatic Atlas of the Indian Ocean. Part III: Upper-Ocean Structure. Univ. of Wisconsin Press.

Hastenrath, S. and L. L. Greischar, 1991: The Monsoonal Current Regimes of the Tropical Indian Oceans: Observed Surface Flow Fields and their Geostrophic and Wind-driven Components. J. Geophys. Res., 96 (C7), 12619-12633.

Hegerl, G. C., H. von Storch, K. Hasselmann, B. D. Santer, U. Cubasch and P. D. Jones, 1996: Detecting greenhouse-gas-induced climate change with an optimal fingerprint method. J. Climate, 10, 2281-2306.

Hellerman, S. and M. Rosenstein, 1983: Normal monthly wind stress over the world ocean with error estimates. J. Phys. Oceanogr., 13, 1093-1104.

Hibler III, W.D., 1979: A dynamic thermodynamic sea ice model. J. Phys. Oceanogr., 9, 815-846.

Hirst, A. C. and W. Cai, 1993: Sensitivity of a world ocean GCM to changes in subsurface mixing parameterization. J. Phys. Oceanogr., 24, 1256-1279.

Hirst, A. C. and J. S. Godfrey, 1993: The Role of Indonesian Throughflow in a Global Ocean GCM. J. Phys. Oceanogr., 23, 1057-1086.

Joyce, T. M. and W. J. Schmitz Jr., 1988: Zonal Velocity Structure and Transport in the Kuroshio Extension. J. Phys. Res., 18, 1484-1494.

Kim, S. J. and A. Stössel, 1998: On the representation of the Southern Ocean water masses in an ocean climate model. J. Geophys. Res., 103(C11), 24891-24906.

Kim, S. J., T. J. Crowley, and A. Stössel, 1998 :Local orbital forcing of Antarctic climate change during the last interglacial.Science, 280(5364), 728-730.

Latif, M., T. Stockdale, J. -O. Wolff, G. Burgess, E. Maier-Reimer, M. M. Junge, K. Arpe, and L. Bengtsson, 1994: Climatology and variability in the ECHO coupled GCM. Tellus, 46A, 351-366.

Legates, D. R. and C. J. Willmott, 1990: Mean seasonal and spatial variability in gauge-corrected, global precipitation. Int. J. Climatol., 10, 111-127.

Legutke, S., E. Maier-Reimer, A. Stössel, and A. Hellbach, 1997: Ocean - sea-ice coupling in a global general circulation model. Annals of Glaciology, 25, 116-120.

Levitus, S., R. Burgett, and T. P. Boyer, 1994: World Ocean Atlas. Vol. 3, Salinity and Vol. 4, Temperture. NOAA Atlas NESDIS 3/4, U. S. Government Printing Office, Washington, DC.

Macdonald, A.M., 1993: Property fluxes at 30^{o}S and their implications for the Pacific-Indian Throughflow and the global heat budget. J. Geophys. Res., 98, 6851-6868.

Macdonald, A.M. and C. Wunsch, 1996: An estimate of global ocean circulation and heat fluxes. Nature, 382(6590), 436-439.

Maier-Reimer, E., U. Mikolajewicz, and K. Hasselmann, 1993: Mean circulation of the Hamburg LSG OGCM and its sensitivity to the thermohaline surface forcing. J. Phys. Oceanogr., 23(4), 732-757.

Manabe S., R. J. Stouffer, 1996: Low Frequency Variability of Surface Air Temperature in a 1000 year Integration of a Coupled Ocean-Atmosphere Model. J. Climate, 9 , 376-393.

Mantyla, A. W. and J. L. Reid, 1995: On the origins of deep and bottom waters of the Indian Ocean. J. Geophys. Res., 100, 2417-2439.

Marsland, S. J. and J.-O. Wolff, 1999: On the sensitivity of Southern Ocean sea ice to the surface freshwater flux: A model study. submitted to J. Geophys. Res.

Martinson, D.G., 1990: Evolution of the Southern Ocean winter mixed layer and sea ice: Open ocean deepwater formation and ventilation. J. Geophys. Res., 95(C7), 11641-11654.

Mauritzen, C., 1996 : Production of dense overflow waters feeding the North Atlantic across the Greenland-Scotland Ridge. 1. Evidence for a revised circulation scheme. Deep-Sea Res., 43(6), 769-806.

Meehl, G. A., W. M. Washington, D. J. Erickson III, B. P. Brielb, and P. J. Jaumann, 1996: Climate change from increased CO2 and direct and indirect effects of sulfate aerosols. Geophys. Res. Lett., 23(25), 3755-3758.

Mitchell, J. F. B. and T. J. Johns, 1997: On the modification of greenhouse gas warming by sulfate aerosols. J. Climate, 10, 245-267.

Molinari, R. L. ,1982: Observations of eastward currents in the tropical South Atlantic Ocean: 1978-1980. J. Geophys. Res., 87, 9707-9714.

Molinari, R. L., B. Voituriez, and P. Duncan, 1981: Observations in the subsurface thermocline undercurrent of the equatorial South Atlantic Ocean : 1978-1980. Oceanologica Acta, 4, 451-456.

Nowlin, W. D. Jr. and J. M. Klinck, 1986: The Physics of the Antarctic Circumpolar Current. Rev. Geophys., 24(3), 469-491.

Oberhuber, J. M., 1988: An Atlas Based on the COADS Data Set: The Budgets of Heat, Buoyancy, and Turbulent Kinetic Energy at the Surface of the Global Ocean. Max-Planck Institut für Meteorology, Report 15.

Pacanowski, R. C. and S. G. H. Philander, 1981: Parameterization of vertical mixing in numerical models of tropical oceans. J. Phys. Oceanogr., 11, 1443-1451.

Parkinson, C. L. and W. M. Washington, 1979: A large-scale numerical model of sea ice. J. Geophys. Res., 84(C1), 311-337.

Peterson, R. G. and L. Stramma, 1991: Upper-level circulation in the South Atlantic Ocean. Prog. Oceanogr., 26, 1-73.

Qiu, B. and T. M. Joyce, 1992: Interannual variability in the mid- and low-latitude western North Pacific. J. Phys. Oceanogr., 22, 1062-1079.

Reid, J. L., 1986: On the total geostrophic circulation of the South Pacific Ocean: Flow patterns, tracers, and transports. Prog. Oceanogr., 16, 1-61.

Ridgway, K. R. and J. S. Godfrey, 1994: Mass and heat budget in the East Australian Current: A direct approach. J. Geophys. Res., 99, 3231-3248.

Rintoul, S. R., 1991: South Atlantic Interbasin Exchange. J. Geophys. Res., 96, 2675-2692.

Roach, A. T., K. Aagaard, C. Pease, S. A. Salo, T. Weingartner, V. Pavlov, and M. Kulakov, 1995: Direct measurements of transport and water properties through the Bering Strait. J. Geophys. Res., 100(C9), 18443-18457.

Robbins, P. E. and J. M. Toole, 1997: The dissolved silicat budget as a constraint on the meridional overturning circulation of the Indian Ocean. Deep-Sea Res., 44(5):879-906.

Rodgers, K.B. , M.Latif, and S. Legutke, 1999: Sensitivity of Equatorial Pacific and Indian Ocean Watermasses to the Position of the Indonesian Throughflow Opening. Geophys. Res. Lett., submitted.

Roeckner, E., K. Arpe, L. Bengtsson, M. Christoph, M. Claussen, L. Dümenil, M. Esch, M. Giorgetta, U. Schlese, and U. Schulzweida, 1996: The atmospheric general circulation model ECHAM-4: Model description and simulation of present-day climate. Reports of the Max-Planck-Institute, Hamburg, No. 218, 90 pp.

Schiller, A., J. S. Godfrey, P. C. McIntosh, G. Meyers, S. E. Wijffels, 1998: Seasonal near-surface dynamics and thermodynamics of the Indian Ocean and Indonesian throughflow in a global ocean general circulation model. J. Phys. Oceanogr., 8(11), 2288-2312.

Schmitz, W. J. Jr., 1995: On the interbasin-scale thermohaline circulation. Rev. Geophys., 33(2), 151-173.

Schmitz, W. J. and M. S. McCartney, 1993: On the North Atlantic circulation. Rev. Geophys., 31(1), 29-49.

Schott, F., J. Reppin, J. Fischer, and D. Quadfasel, 1994: Currents and transports of the monsoon current south of Sri Lanka. J. Geophys. Res., 99(C12), 25127-25141.

Semtner, A. J. and R. M. Chervin, 1992: Ocean general circulation from a global eddy-resolving model. J. Geophys. Res., 97, 5493-5550.

Smith, R. L., A. Huyer, J. S. Godfrey, and J. A. Church, 1991: The Leeuwin Current off western Australia. J. Phys. Oceanogr., 21, 322-345.

Stössel, A., S. J. Kim, and S. S .Drijfhout, 1998: The Impact of Southern Ocean Sea Ice in a Global Ocean Model. J. Phys. Oceanogr., 28(10), 1999-2018.

Stössel, A. and S. J. Kim 1998: An interannual Antarctic sea-ice - ocean mode. Geophys. Res. Lett., 25(7), 1007-1010.

Stramma L. and J. R. E. Lutjeharms, 1997: The flow field of the subtropical gyre of the South Indian Ocean. J. Geophys. Res., 102 (C3), 5513-5530.

Stramma, L. and R. G. Peterson, 1989: Geostrophic transport in the Benguela Current region. J. Phys. Oceanogr., 19, 1440-1448.

Stramma, L., Y. Ikeda, and R. G. Peterson, 1990: Geostrophic transport in the Brazil Current region north of 20^{o} S. Deep-Sea Res., 37, 1875-1886.

Tabata, S., 1975: The general circulation of the Pacific Ocean and a brief account of the oceanographic structure of the North Pacific, Part I-Circulation and volume transports. Atmosphere, 13, 133-168.

Talley, L., 1984: Meridional heat transport in the Pacific Ocean. J. Phys. Oceanogr., 14, 231-241.

Thomas, D., S. Martin, D. Rothrock, and S. Steele, 1996: Assimilating satellite concentration data into an Arctic sea ice mass balance model, 1979-1985. J. Geophys. Res., 101(C9), 20849-20868.

Toole, J. M. and B. A. Warren, 1993: A hydrographic section across the subtropical South Indic Ocean. Deep-Sea Res., 40, 1973-2019.

Toggweiler, J. R. and B. Samuels, 1994 : New radiocarbon constraints on the upwelling of abyssal water to the ocean's surface. In : The Global Carbon Cycle, M. Heimann, ed., NATO ASI Series, Springer Verlag Berlin, 333-366.

Toggweiler, J. R. and B. Samuels, 1995: Effect of Sea Ice on the Salinity of Antarctic Bottom Waters. J. Phys. Oceanogr., 25, 1980-1997.

Trenberth, K. E., 1979: Mean annual poleward energy transport by the oceans in the southern hemisphere. Dyn. Atmos. Oceans, 4, 57-64.

Trenberth, K. E. and A. Solomon, 1994: The global heat balance: Heat transports in the atmosphere and the ocean. Climate Dyn., 10, 107-134.

UNESCO, 1983: Algorithms for computation of fundamental properties of sea water. UNESCO Technical Papers in Marine Science, No. 44.

Venzke, S., M. Latif, and A. Villwock, 1999: The Coupled GCM ECHO-2. Part II: Indian Ocean Response to ENSO. J. of Climate, submitted.

Warner, M. J. and R. F. Weiss, 1992: Clorofluoromethanes in South Atlantic Antarctic Intermediate Water. Deep-sea Res., 39, 2053-2075.

Wijffels, S. E., J. M. Toole, H. L. Bryden, R. A. Fine, W. J. Jenkins, and J. L. Bullister, 1996: The Water masses and circulation at 10-degrees-N in the Pacific. Deep-Sea Res., 43(4), 501-544.

Whitworth III, T., and R. G. Peterson, 1985: The volume transport of the Antarctic Circumpolar Current from 3-year bottom pressure measurements. J. Phys. Oceanogr., 15(6), 810-816.

Wolff, J.-O., E. Maier-Reimer, and S. Legutke, 1997: The Hamburg Ocean Primitive Equation Model. Technical report, No. 13, German Climate Computer Center (DKRZ), Hamburg, 98 pp.

Wyrtki, K., 1973: An equatorial jet in the Indian Ocean. Science, 181, 262-264.

Wyrtki, K. and B. Kilonsky, 1983: Mean Water and Current Structure during the Hawaii-to-Tahiti Shuttle Experiment. J. Phys. Oceanogr., 14, 242-254.

Zhang, X.-H., J. M. Oberhuber, A. Bacher, and E. Roeckner, 1998: Interpretation of interbasin exchange in an isopycnal ocean model. Climate Dynamics, 14, 725-740.

7 Figures

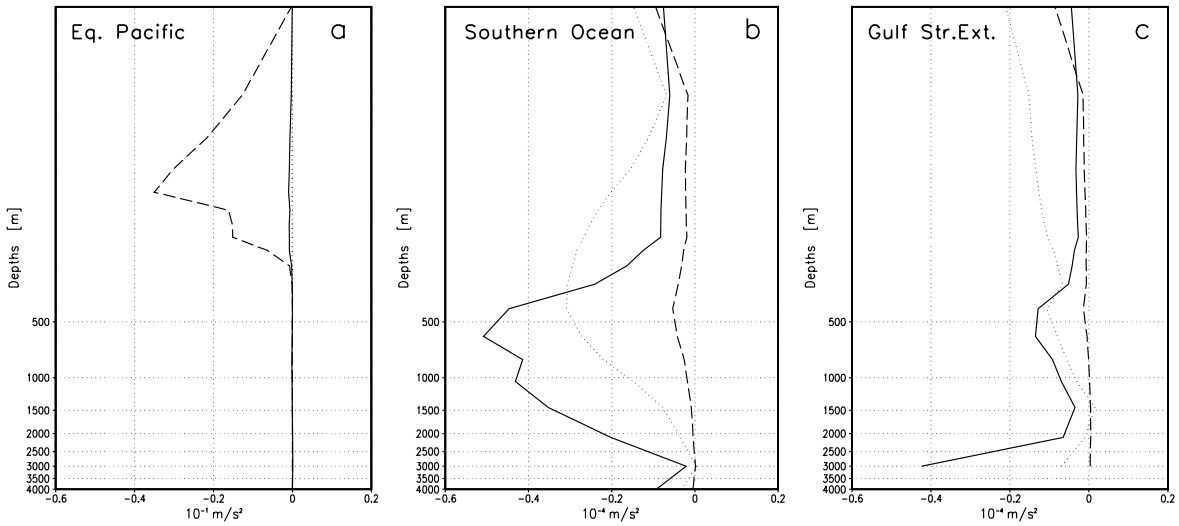

Figure 1: Annual-mean vertical profiles of effective horizontal viscosity in the zonal momentum equation in (a) the equatorial Pacific, (b) the Southern Ocean, and (c) the Gulf Stream Extension. The dashed, full, and dotted curves show the shear-dependent, harmonic, and biharmonic terms of eq. 2.1.1 respectively. The units of the Pacific profiles are 10^{-1}m s^{-2}. All other curves have unit 10^{-4}m s^{-2}.

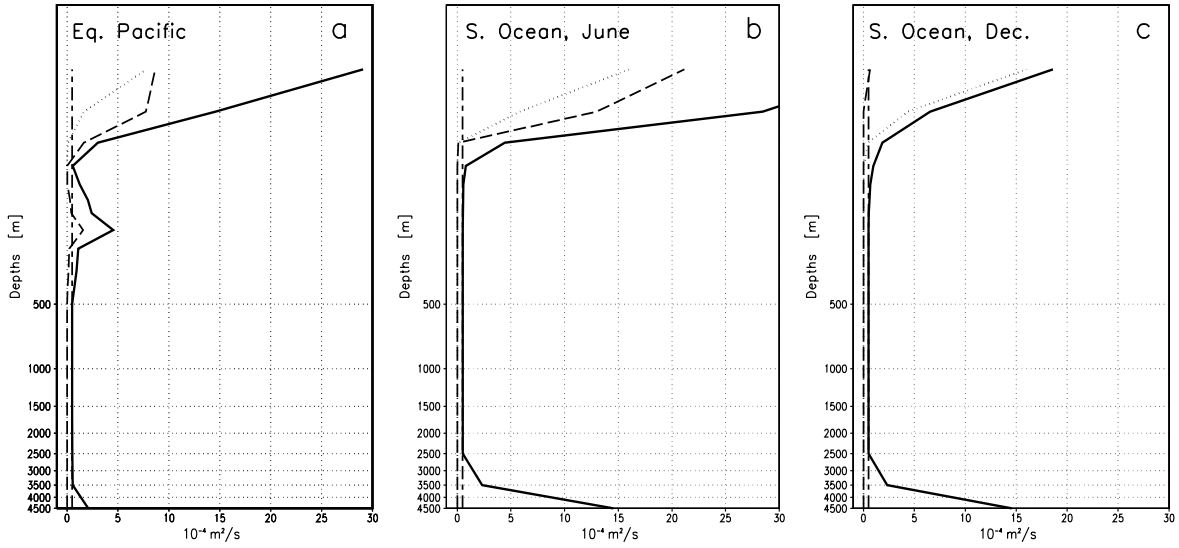

Figure 2: Vertical profiles of effective vertical eddy viscosity coefficients in June in (a) the equatorial Pacific and (b) the Southern Ocean. (c) Same as (b) in December. The full, dashed, dotted, and short-long-dashed curves are for the total, the Richardson-no.-dependent, the mixed-layer, and background coefficients respectively.
Units are 10^{-4}m^2 s^{-1}.

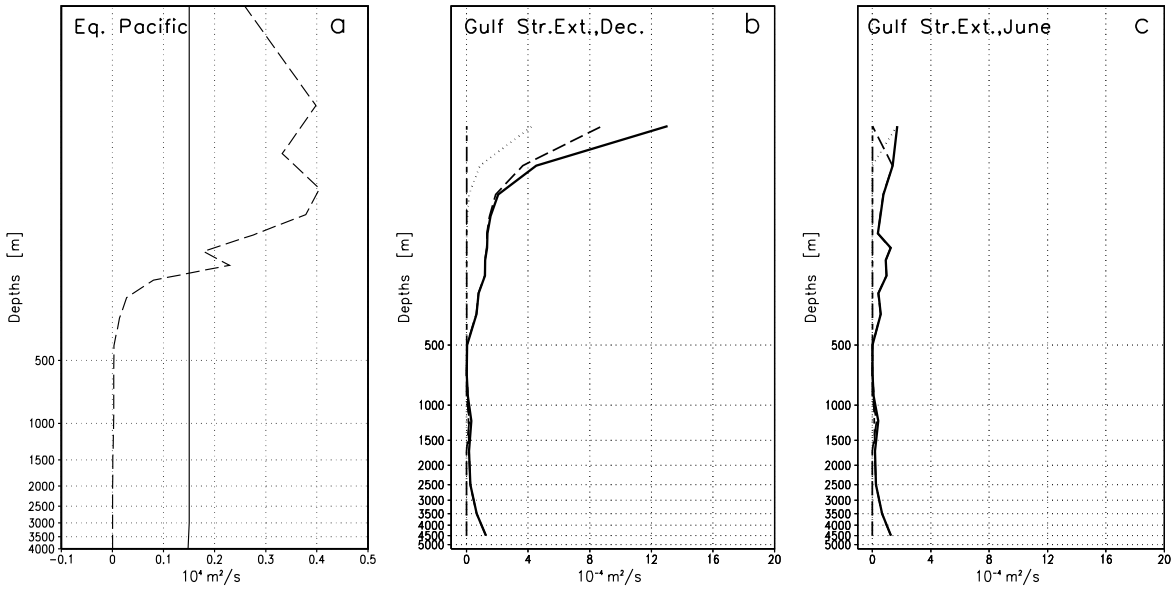

Figure 3: (a) Annual-mean vertical profiles of shear-dependent (dashed curve) and harmonic (full curve) effective horizontal diffusivity coefficients in the equatorial Pacific. Units are $10^4 m^2\ s^{-1}$. (b) Vertical profiles of total (full curve), Richardson-no.-dependent (dashed curve), mixed-layer (dotted curve), and background (short-long-dashed curve) vertical effective eddy diffusivity coefficients in the Gulf Stream Extension in December.
(c) Same as (b) in June. Units are $10^{-4} m^2\ s^{-1}$.

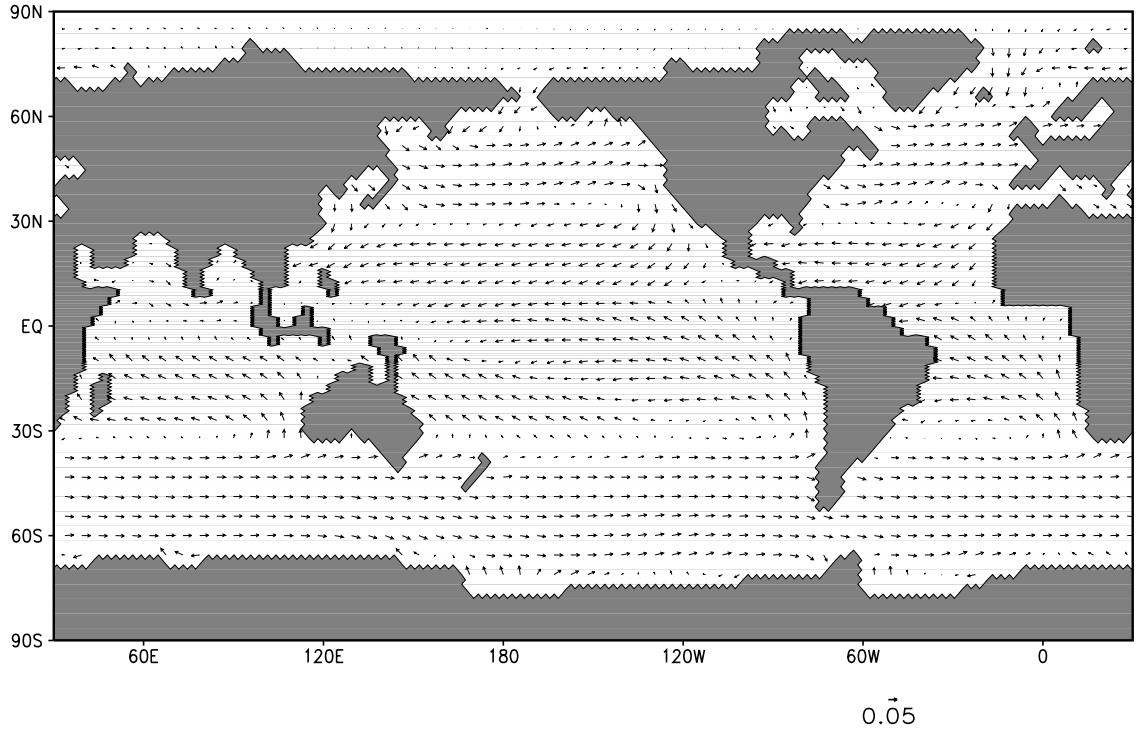

Figure 4: 15-year-mean annual surface stress as it is applied to the ocean. In high latitudes, the ECHAM4-generated forcing data are modified by the water/ice interfacial stress computed prognostically in the model. The arrow lengths vary linearly with the magnitude of the wind stress for values below 0.05 Pa. Higher values have all the same arrow length of a half zonal gridpoint distance.

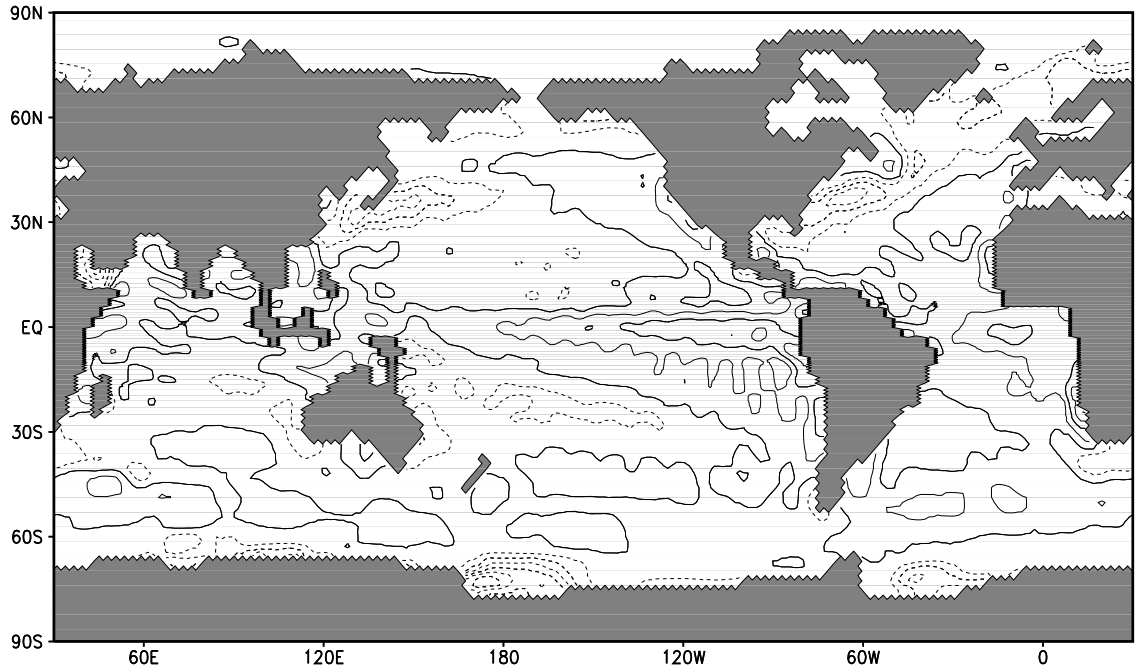

Figure 5: 15-year-mean annual atmospheric surface heat flux as it is applied to the ocean. In high latitudes, the flux is computed with bulk-formulas using near-surface atmosphere variables. Units are $\mathrm{W\ m^{-2}}$, contour interval is $40\ \mathrm{W\ m^{-2}}$, negative (upward flux) contours are dashed.

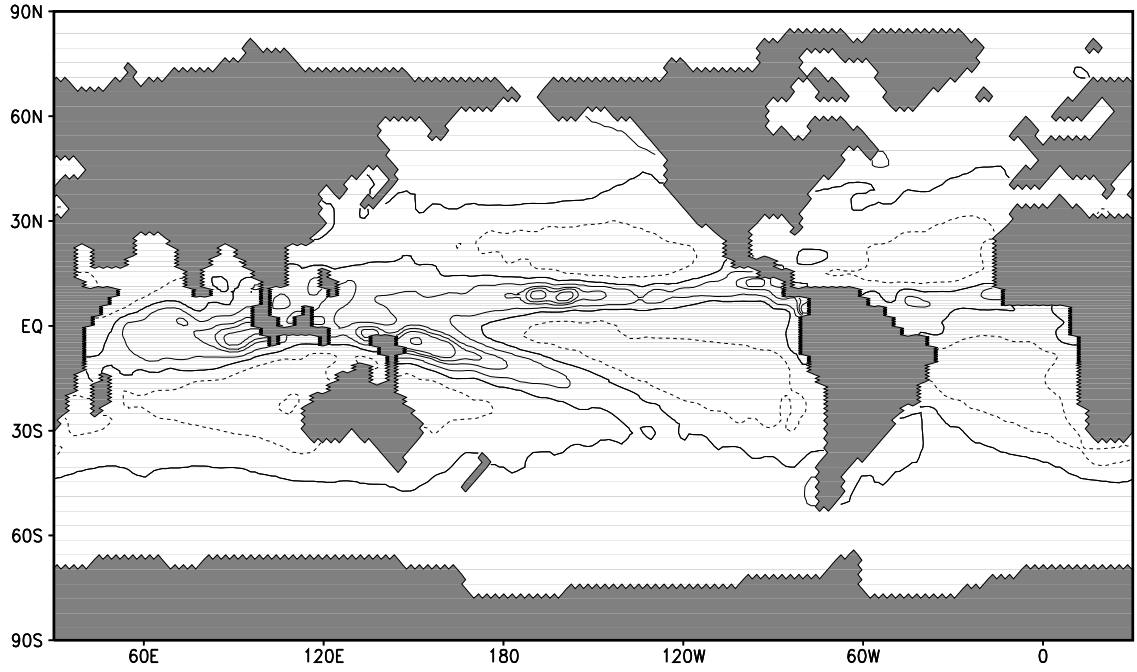

Figure 6: 15-year-mean annual atmospheric freshwater flux (without runoff) as it is applied to the ocean. In high latitudes, the precipitation is modified by the net local snow fall or melt. Units are $\mathrm{m\ a^{-1}}$, contour interval is $1\ \mathrm{m\ a^{-1}}$, negative (upward flux) contours are dashed.

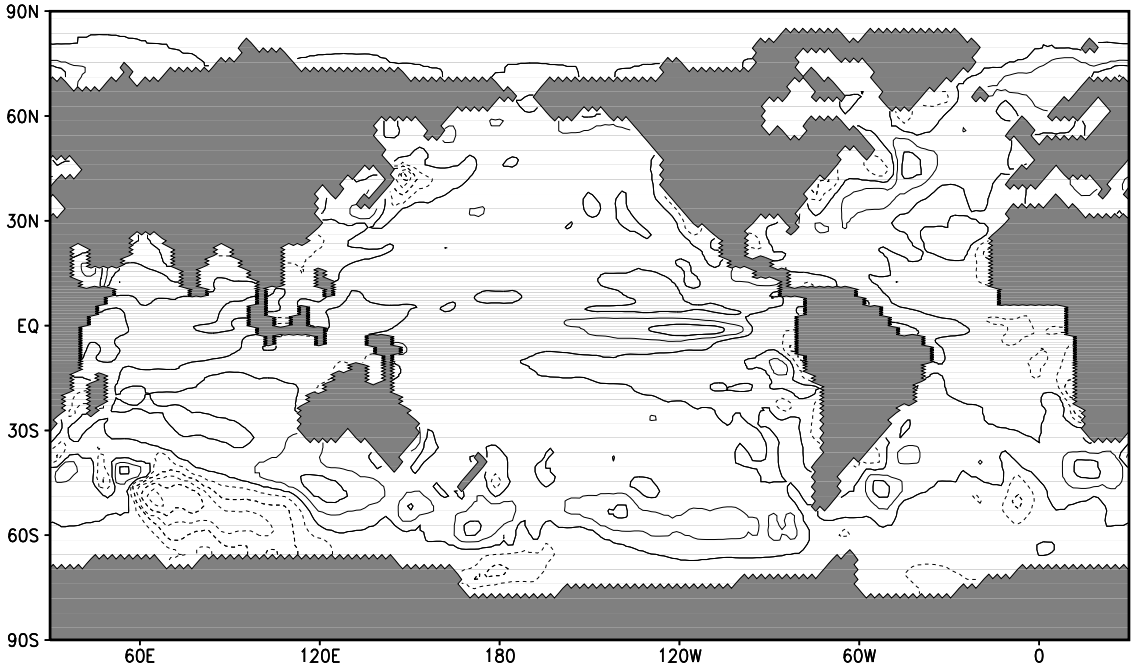

Figure 7: 15-year-mean annual surface heat flux diagnosed from the SST relaxation. Units are W m^{-2}, contour interval is 40 W m^{-2}, negative (upward flux) contours are dashed.

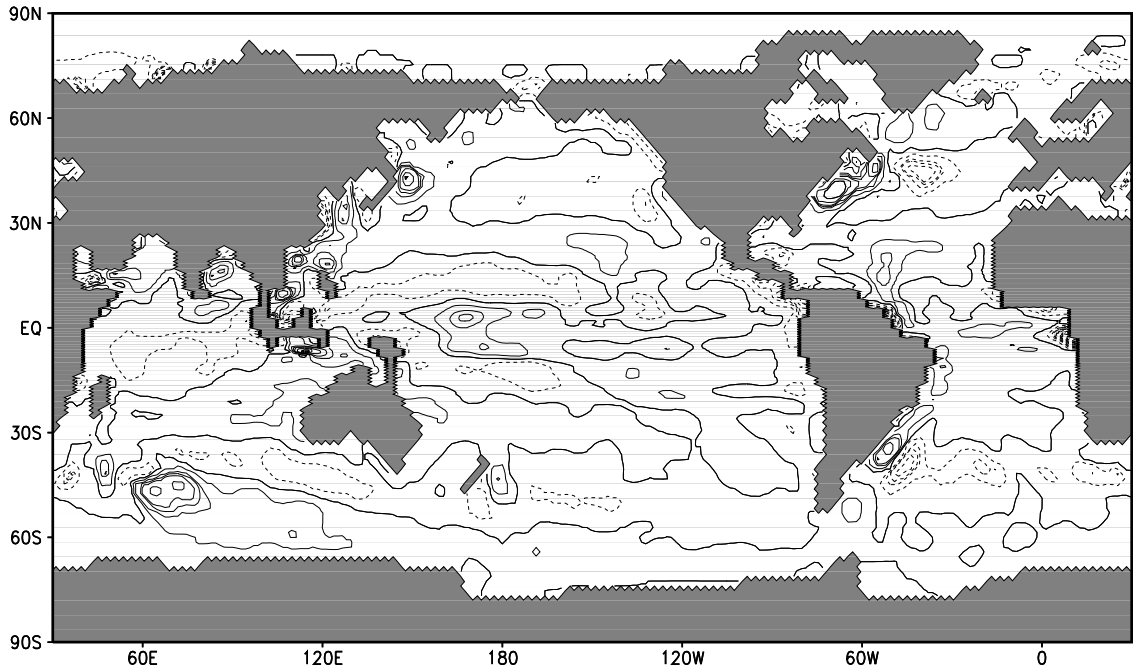

Figure 8: 15-year-mean freshwater flux corresponding to the SSS relaxation. Units are m a^{-1}, contour interval is 1m a^{-1}, negative (upward flux) values are dashed.

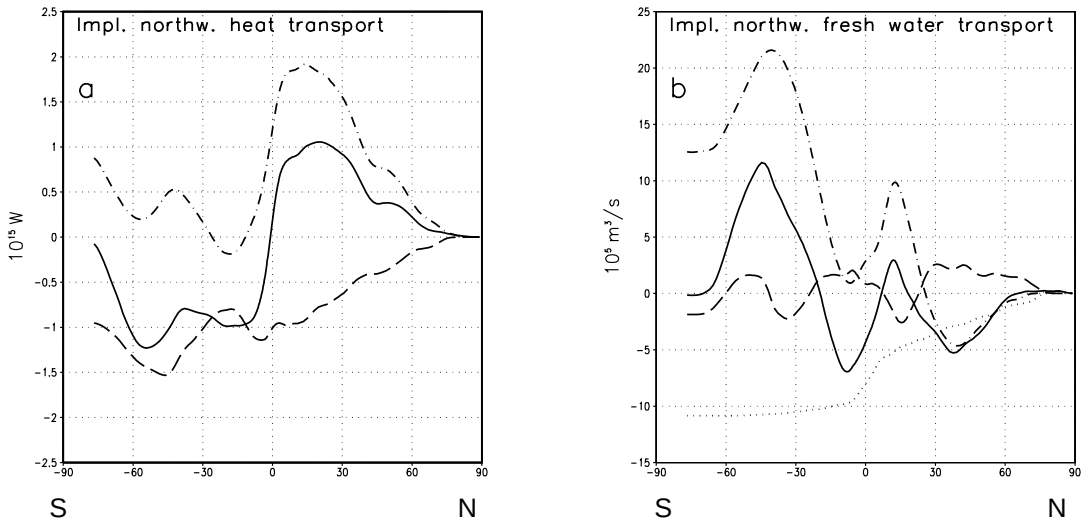

Figure 9: Northward global transport of (a) heat and (b) fresh water as implied by the net atmospheric surface fluxes (dash-dotted curve) and by the fluxes stemming from the surface relaxation (dashed curve). The dotted line shows the effect of the continental runoff. The total implied transport is given by the full curve. Units are 10^{15}W and $10^5 m^3\ s^{-1}$ respectively.

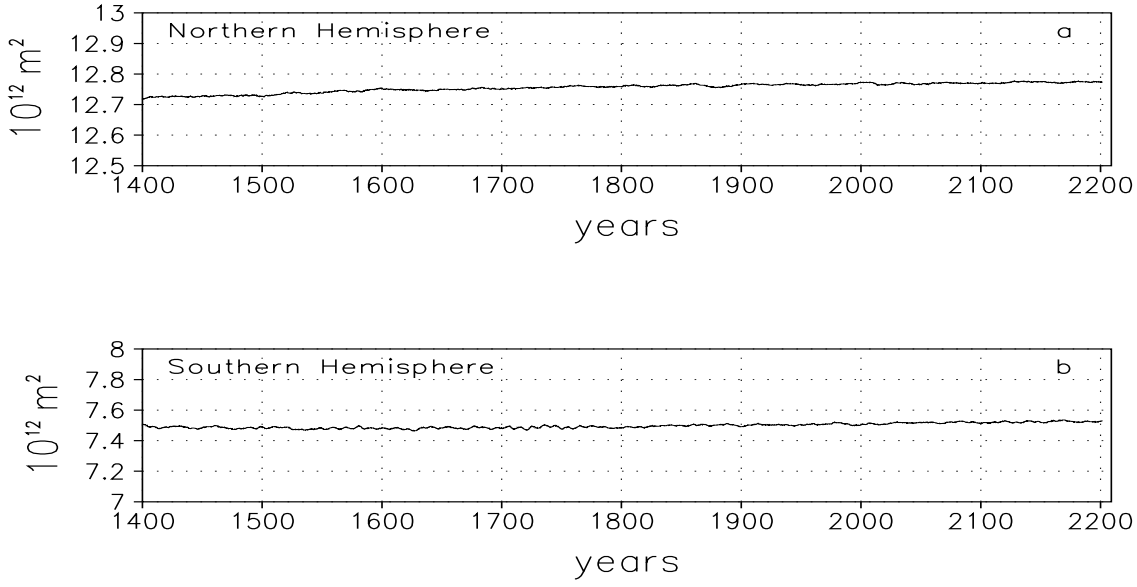

Figure 10: Time series of 15-year-mean annual ice extent in (a) the Arctic and (b) the Southern Ocean. Units are $10^{12} m^2$. The trend of the Arctic sea-ice extent is 0.2% per 90 years, and that of the SO is 0.6% per 90 years at the end of the integration.

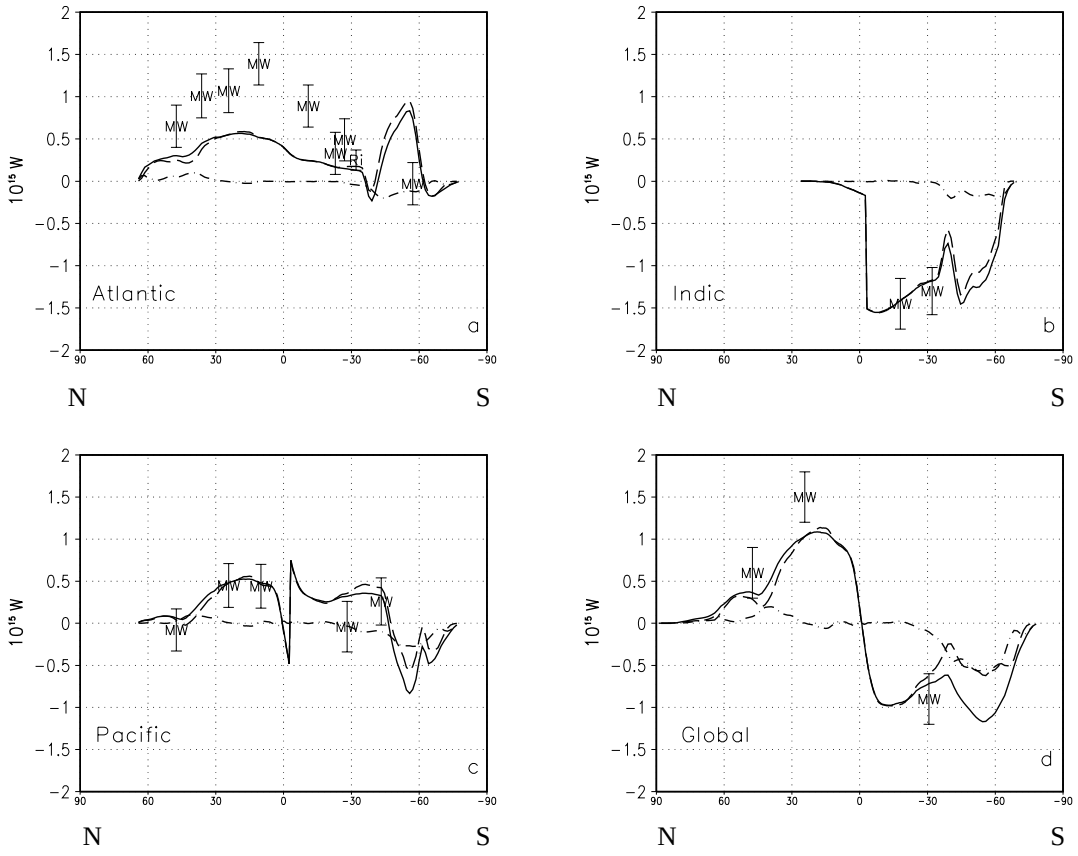

Figure 11: Northward heat transport in the ocean for the (a) Atlantic, (b) Indian, (c) Pacific, and (d) Global Ocean by advection (dashed curve) and diffusion (dash-dot curve). The full line is the total transport. Units are 10^{15}W. Error bars labelled with MW give the results of Macdonald and Wunsch (1996), the one labelled with RI is taken from Rintoul (1991).

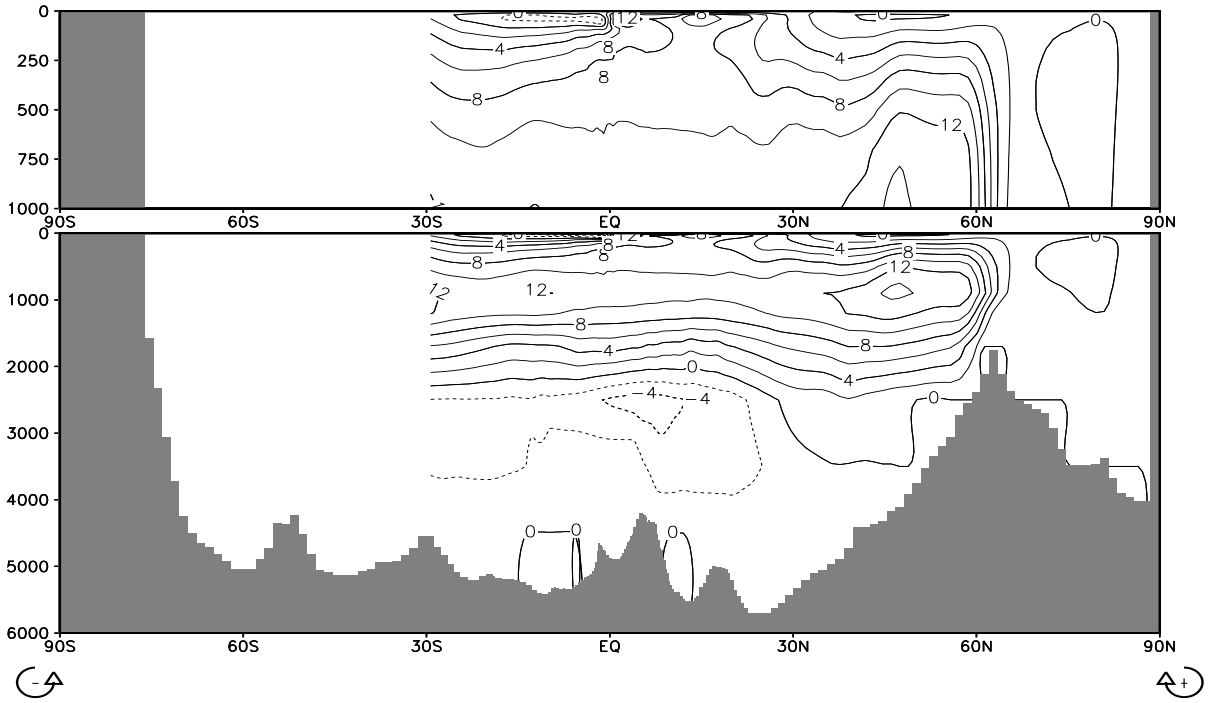

Figure 12a: Streamfunction of the zonally integrated velocity in the Atlantic Ocean.
Contour interval is 2.0 x 10^6 m^3s^{-1}.

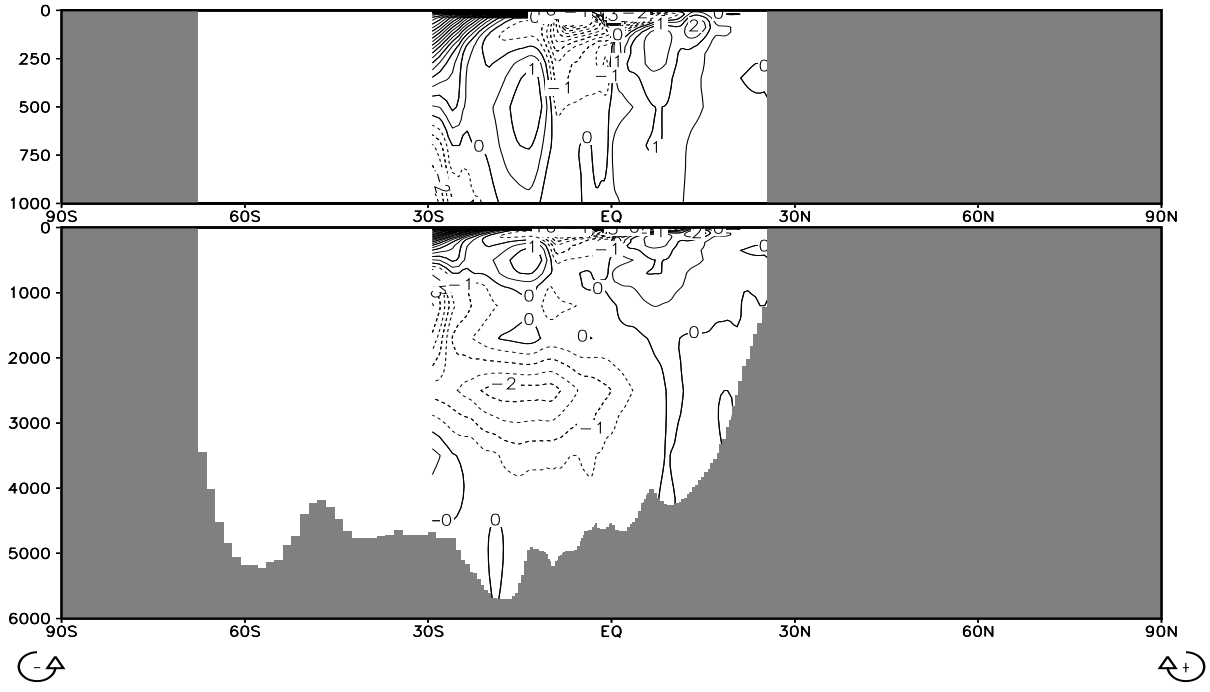

Figure 12b: Streamfunction of the zonally integrated velocity in the Indian Ocean.
Contour interval is 0.5 x 10^6 m^3s^{-1}.

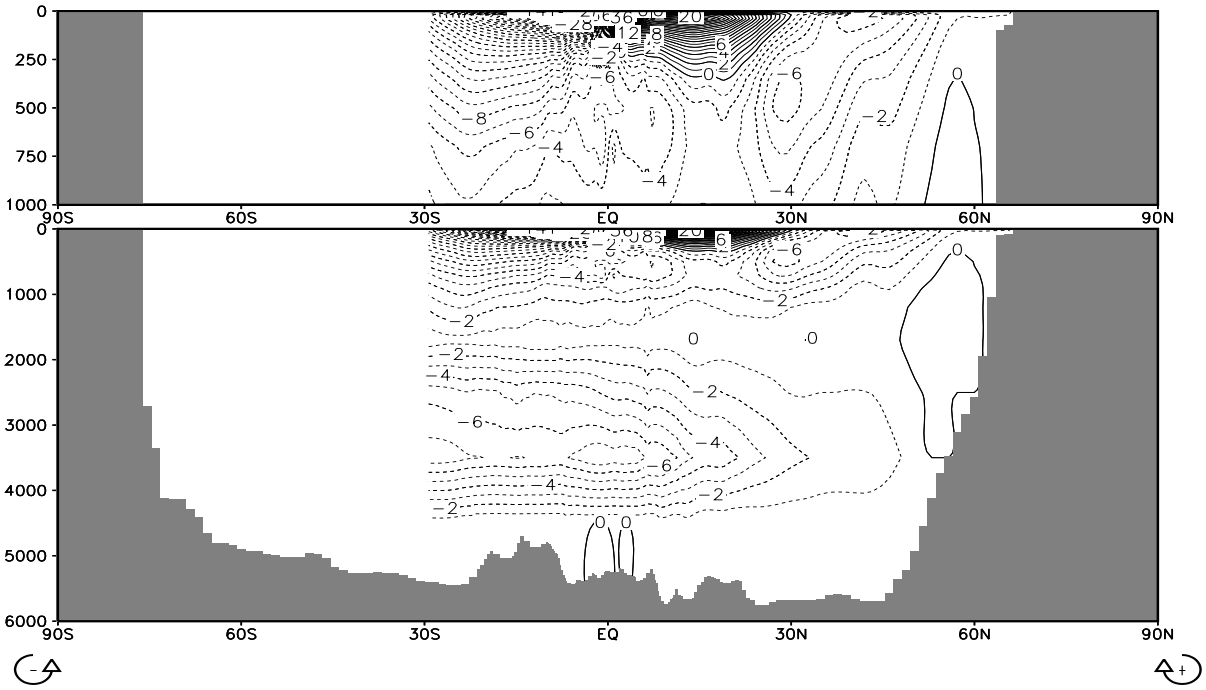

Figure 12c: Streamfunction of the zonally integrated velocity in the Pacific Ocean.
Contour interval is 1.0 x 10^6 m^3s^{-1}.

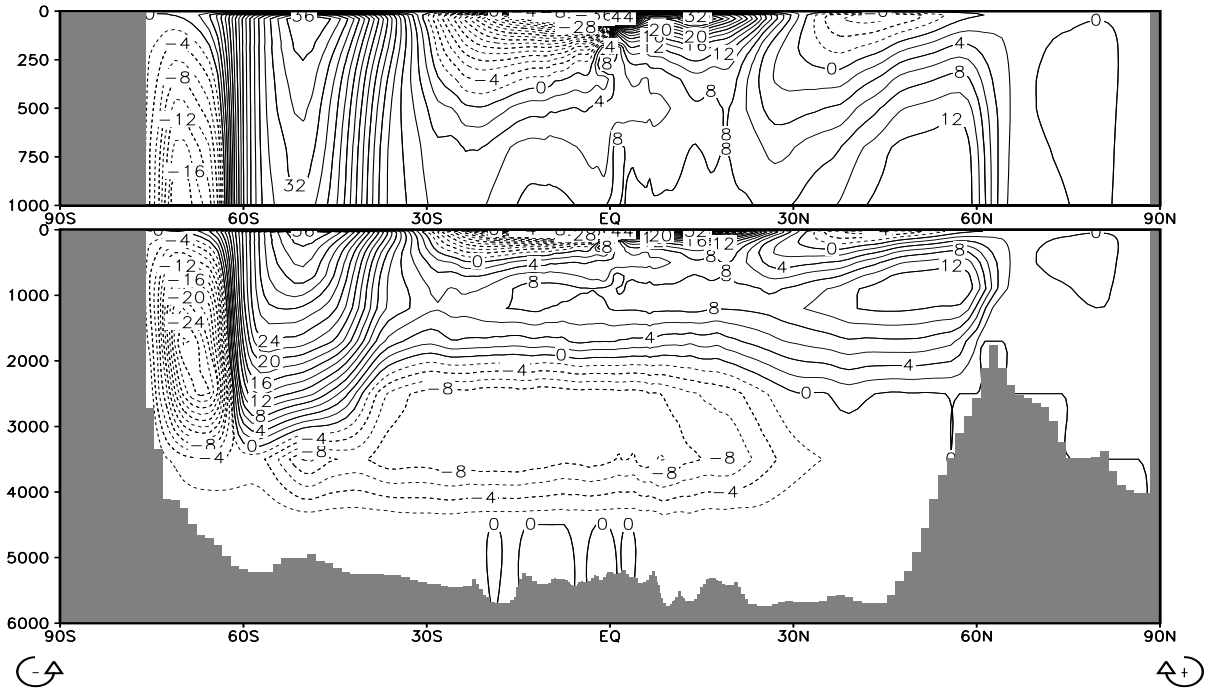

Figure 12d: Streamfunction of the zonally integrated velocity in the Global Ocean.
Contour interval is 2.0 x 10^6 m^3s^{-1}.

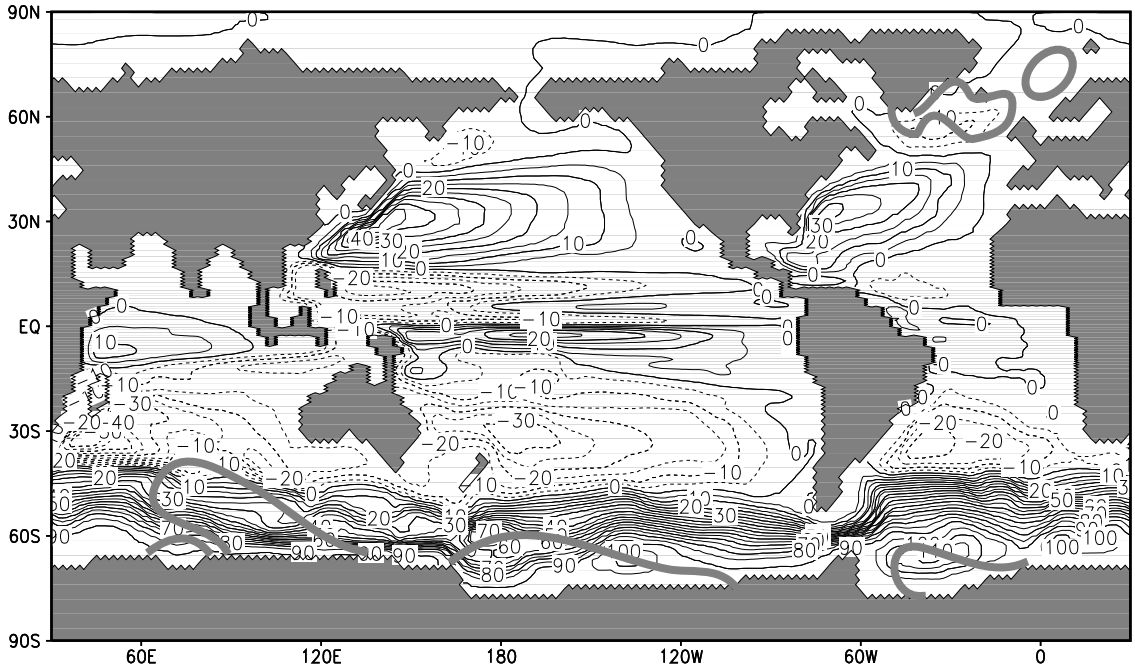

Figure 13: Streamfunction of the vertically integrated horizontal velocity field. Contour interval is 5 x 10^6 m^3s^{-1}. Thick gray lines enclose regions with significant release of potential energy by convective overturning (adjustment).

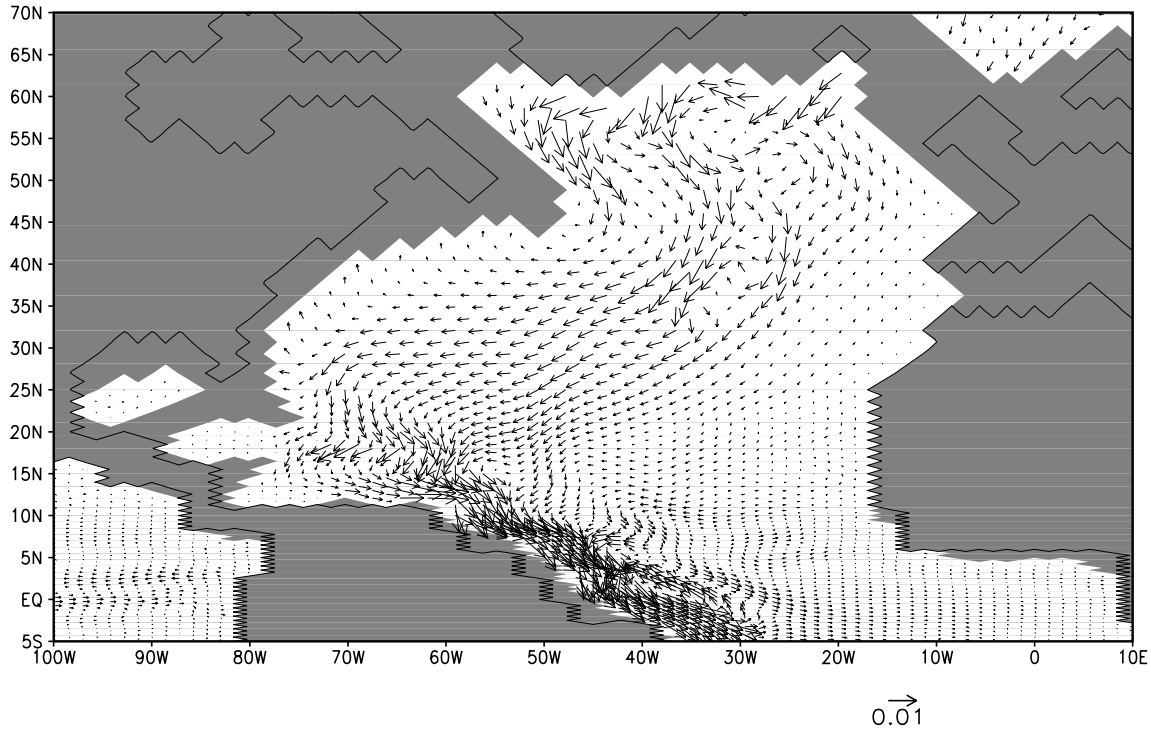

Figure 14a: Horizontal velocities in the North Atlantic (vertical mean between 1200 and 2500 m , level 16-17). The speed is proportional to the arrow length if it is below 1 cm s^{-1}. Higher speeds have an arrow length of 1 zonal gridpoint distance.

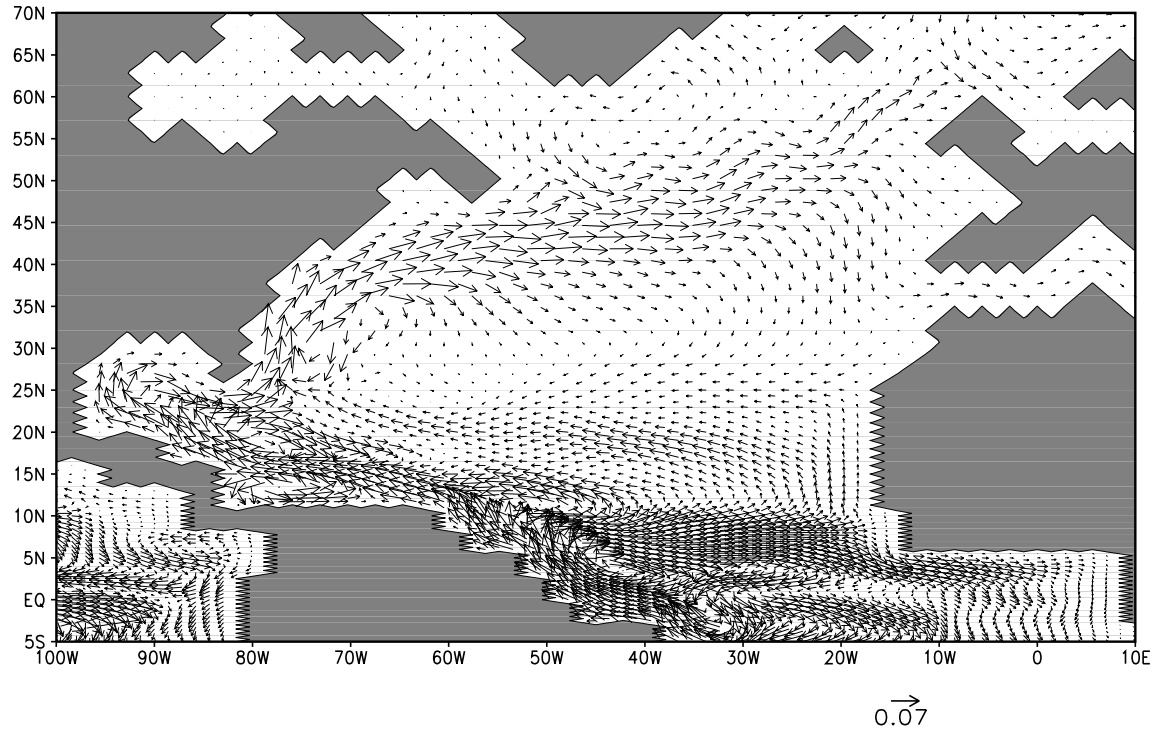

Figure 14b: Horizontal velocities in the North Atlantic above 88 m (level 1-4). The speed is proportional to the arrow length if it is below 7.5 cm s^{-1}. Higher speeds have an arrow length of 1 zonal gridpoint distance.

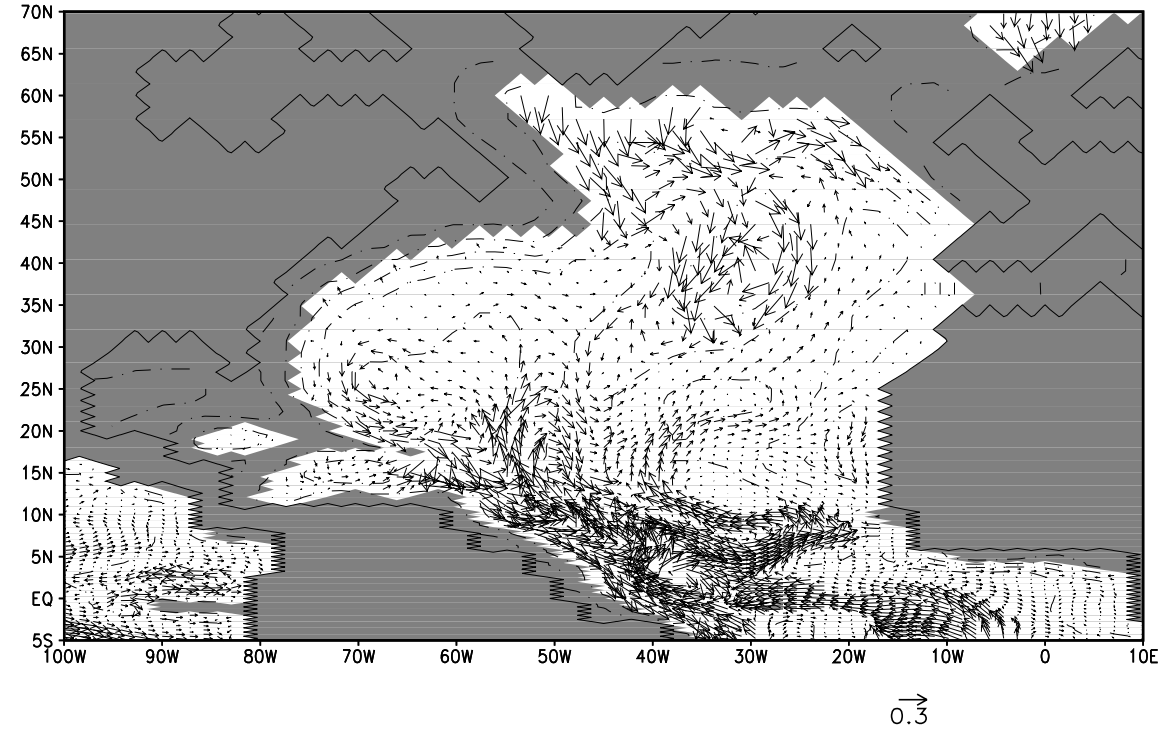

Figure 14c: Horizontal bottom velocities in the North Atlantic where the water depth is larger than 2100 m. The speed is proportional to the arrow length if it is below 0.3 cm s^{-1}. Higher speeds have an arrow length of 1 zonal gridpoint distance.

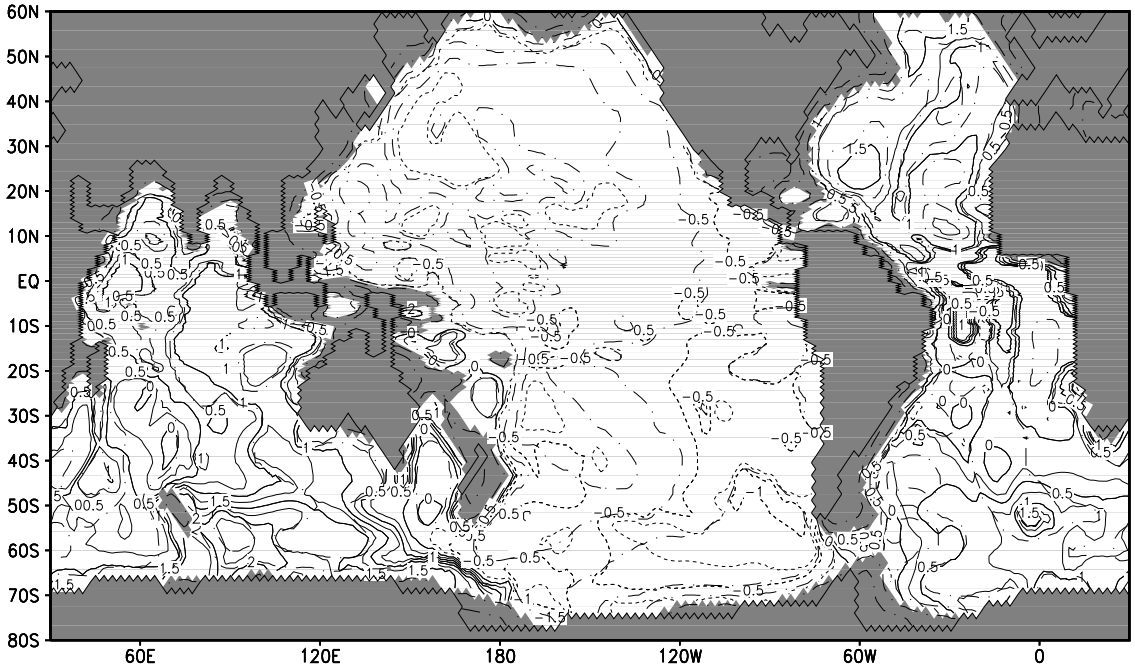

Figure 15a: Distribution of potential temperature error (model - observed) in the bottom layer.
Contour interval is 0.25^{o} C. Negative contours are short-dashed. The dot-dash contours show topographic isolines.

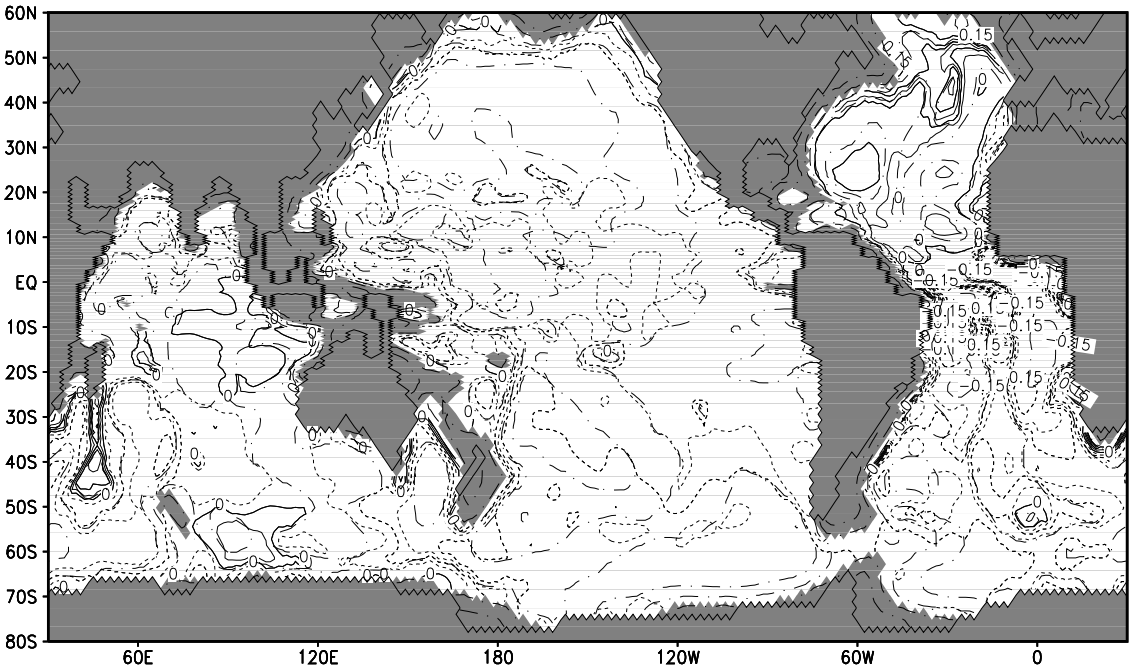

Figure 15b: Distribution of salinity error (model - observed) in the bottom layer. Contour interval 0.025 psu.
Negative contours are short-dashed. The dot-dash contours show topographic isolines.

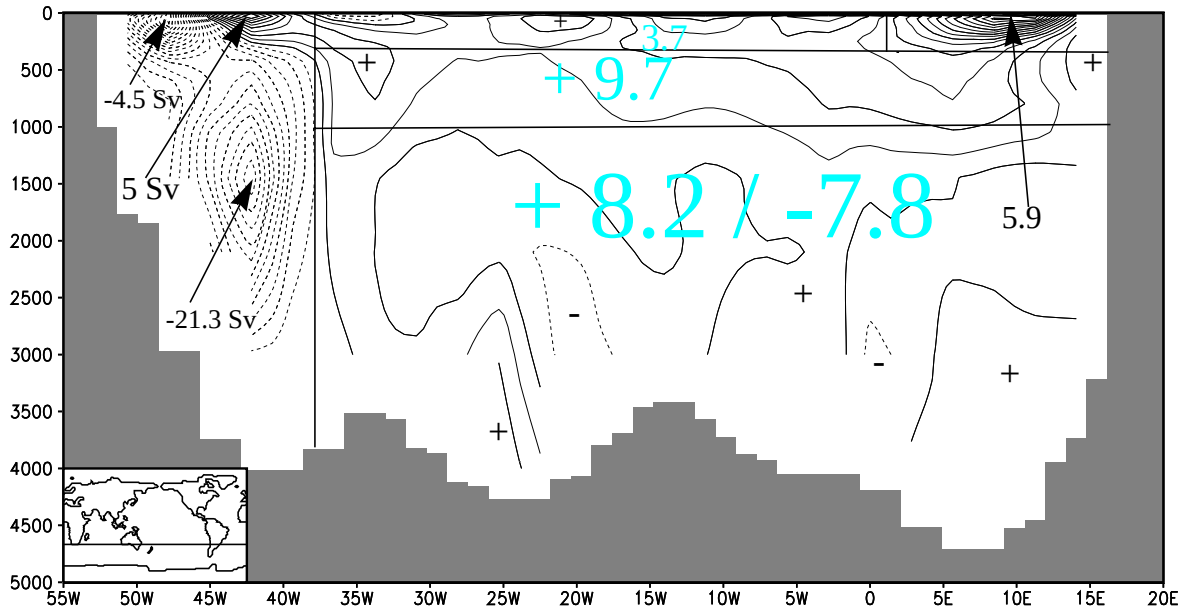

Figure 16a: Meridional velocity at 32^{o} S in the Atlantic Ocean. Contour interval is 0.2 cm s^{-1}. Dashed lines indicate a southward direction. The figures included give the volume transports of current branches and net flow through parts of the section defined by the horizontal and vertical lines.

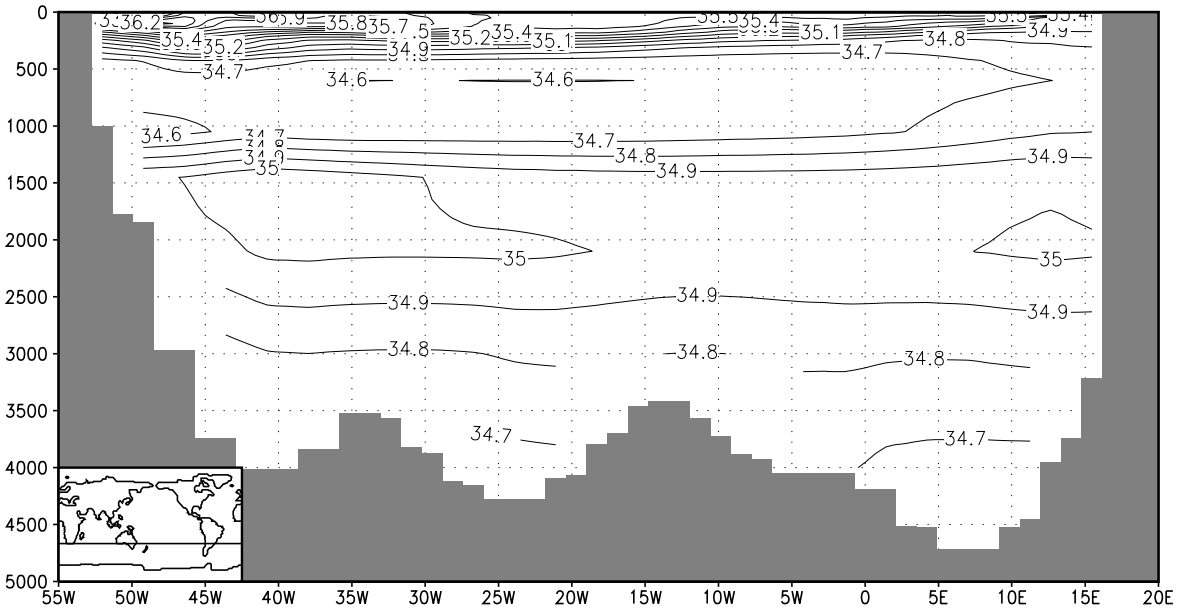

Figure 16b: Simulated salinity at 32^{o} S in the Atlantic Ocean. Contour interval is 0.1 psu.

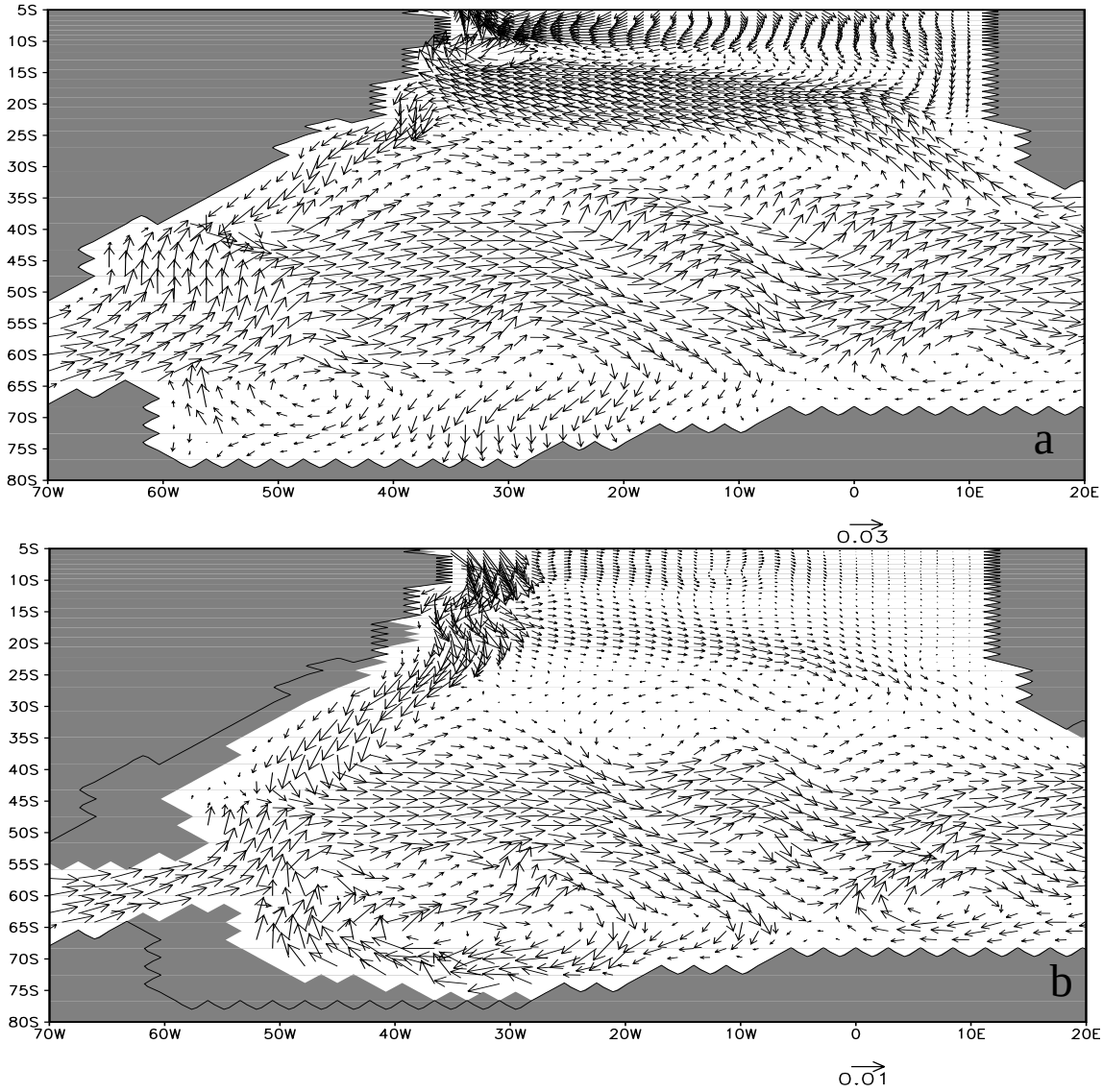

Figure 17: Horizonal velocities above 175 m (upper pannel) and between 1200 and 2500 m (lower pannel). Arrows representing velocities above 3 and 1 cm s^{-1} respectively are truncated to one zonal gridpoint distance.

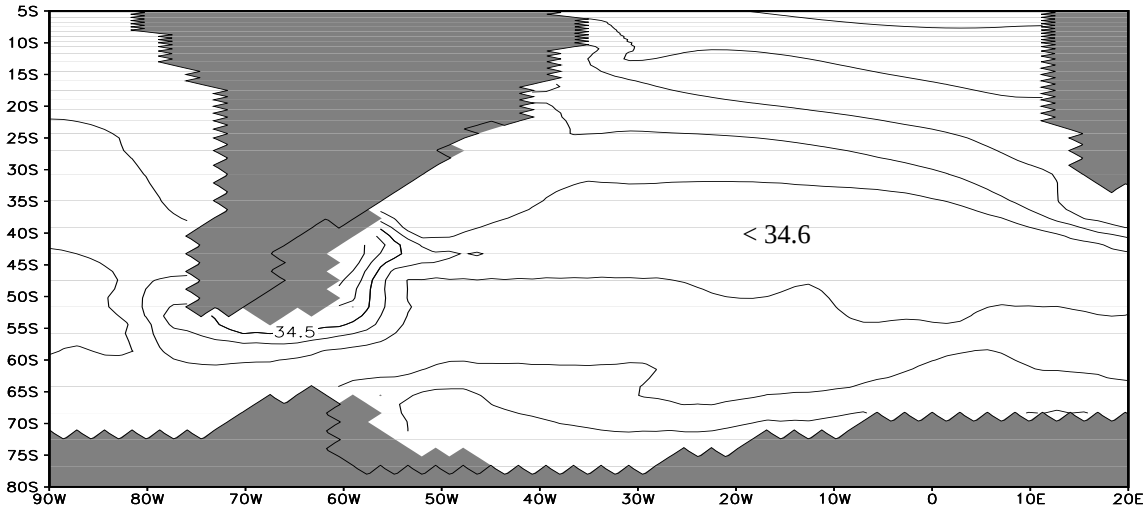

Figure 18: Salinity at 600 m (level 13) in the South Atlantic. Contour interval is 0.05 psu.

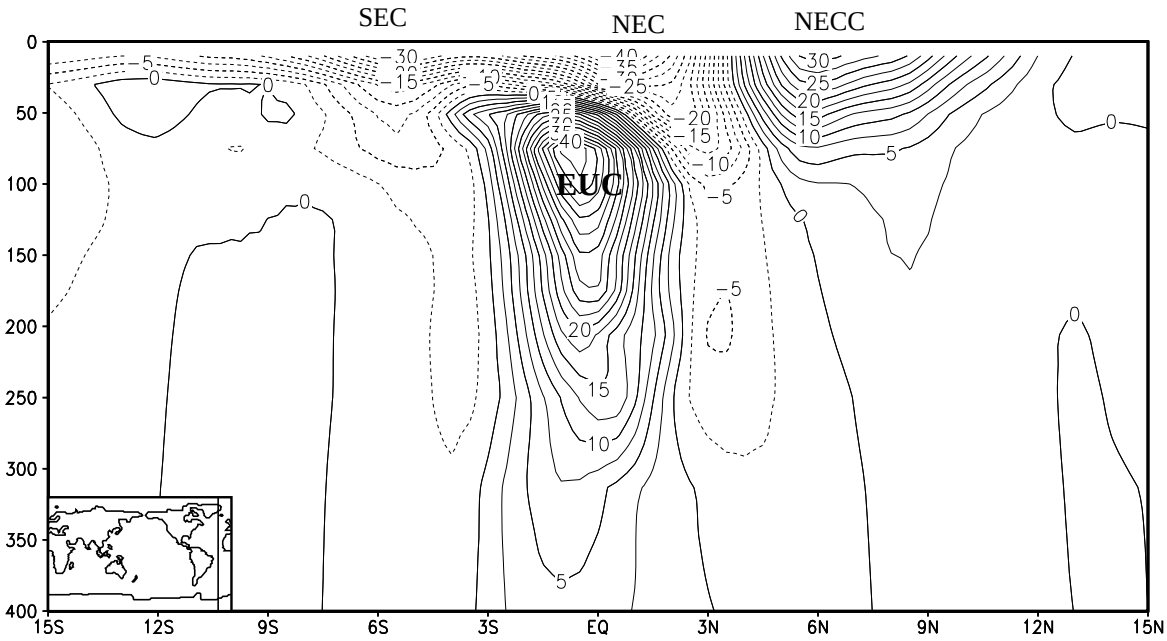

Figure 19a: Zonal velocity in the upper equatorial Atlantic Ocean at 26^{o} E in August.
Contour interval is 2.5 cm s^{-1}. Dashed lines indicate a western direction.

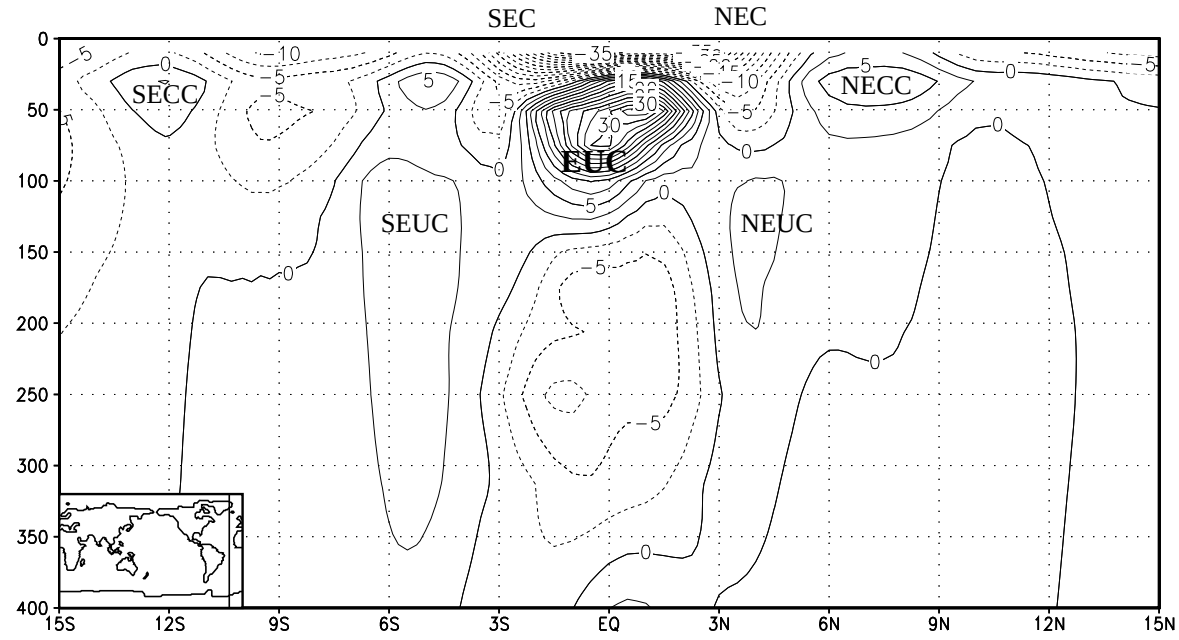

Figure 19b: Zonal velocity in the upper equatorial Atlantic Ocean at 26^{o} E in February.
Contour interval is 2.5 cm s^{-1}. Dashed lines indicate a western direction.

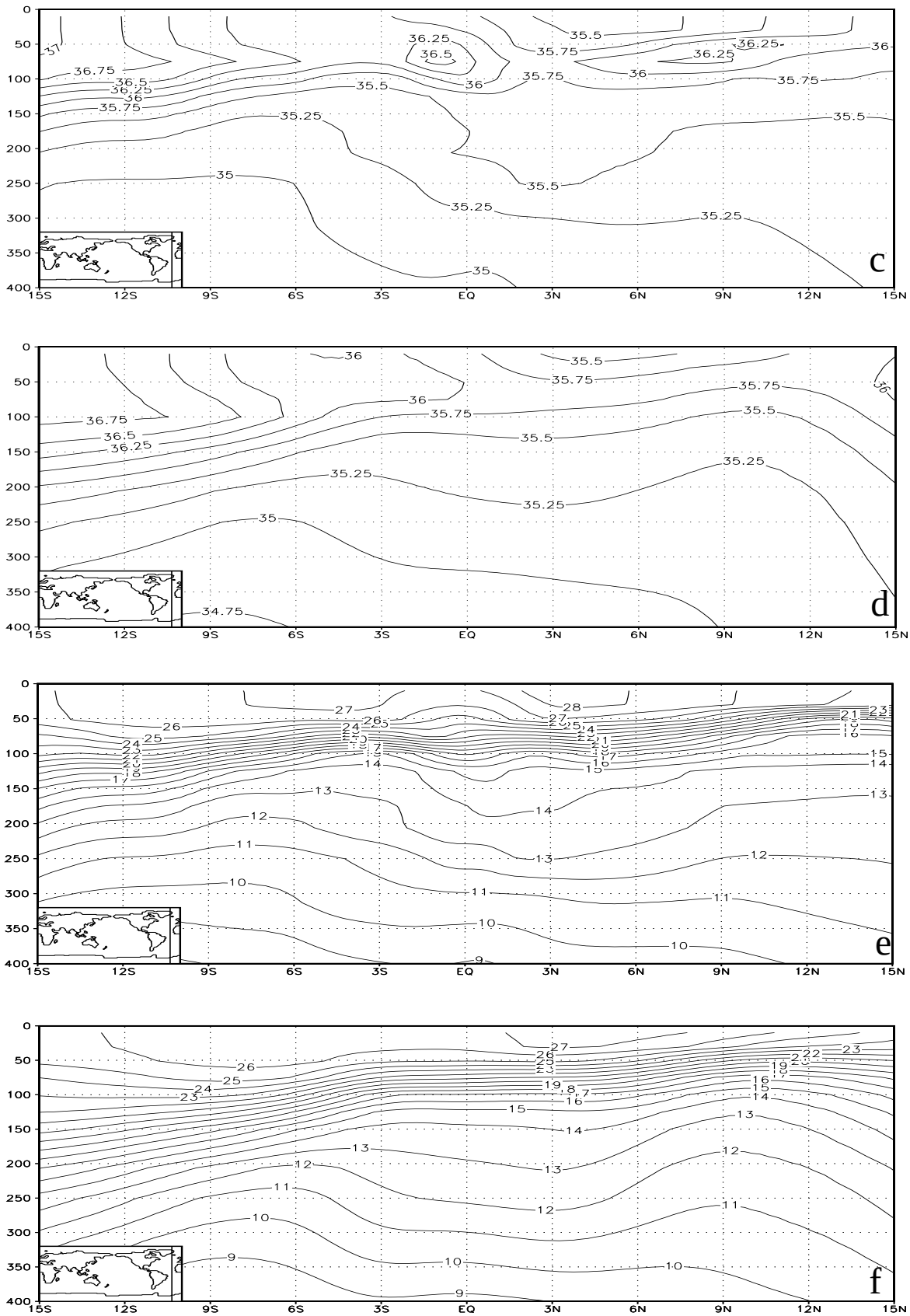

Figure 19: Annual mean (c) simulated and (d) observed salinity and (e) simulated and (f) observed potential temperature in the upper equatorial Atlantic Ocean at 26^{o} E.

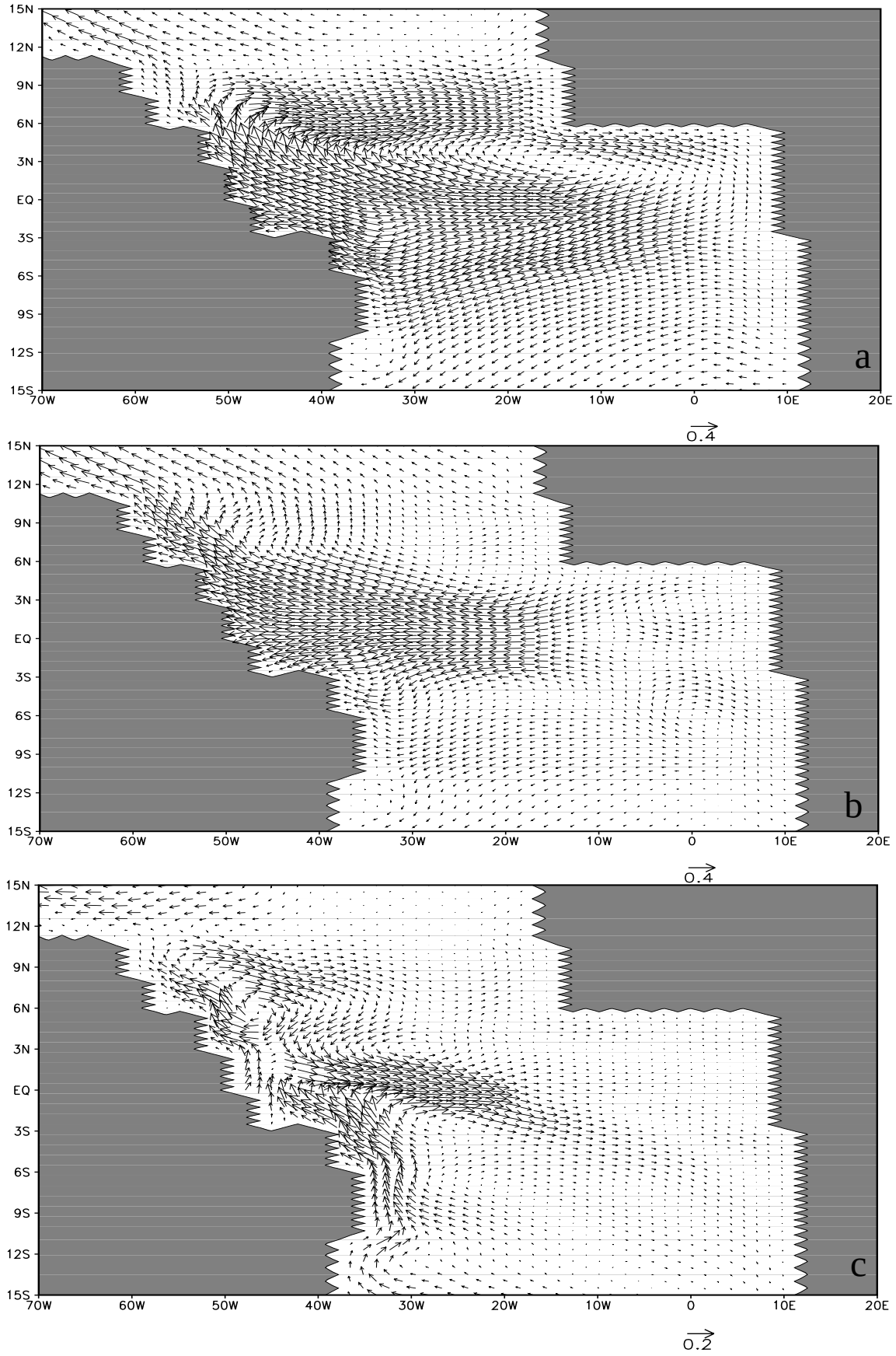

Figure 20: Horizontal velocities in the equatorial Atlantic at the surface in (a) August and (b) February and (c) at 75 m in February. Arrows, which represent a speed above 40, 40, and 20 cms $^{-1}$ respectively, are truncated to one zonal gridpoint distance.

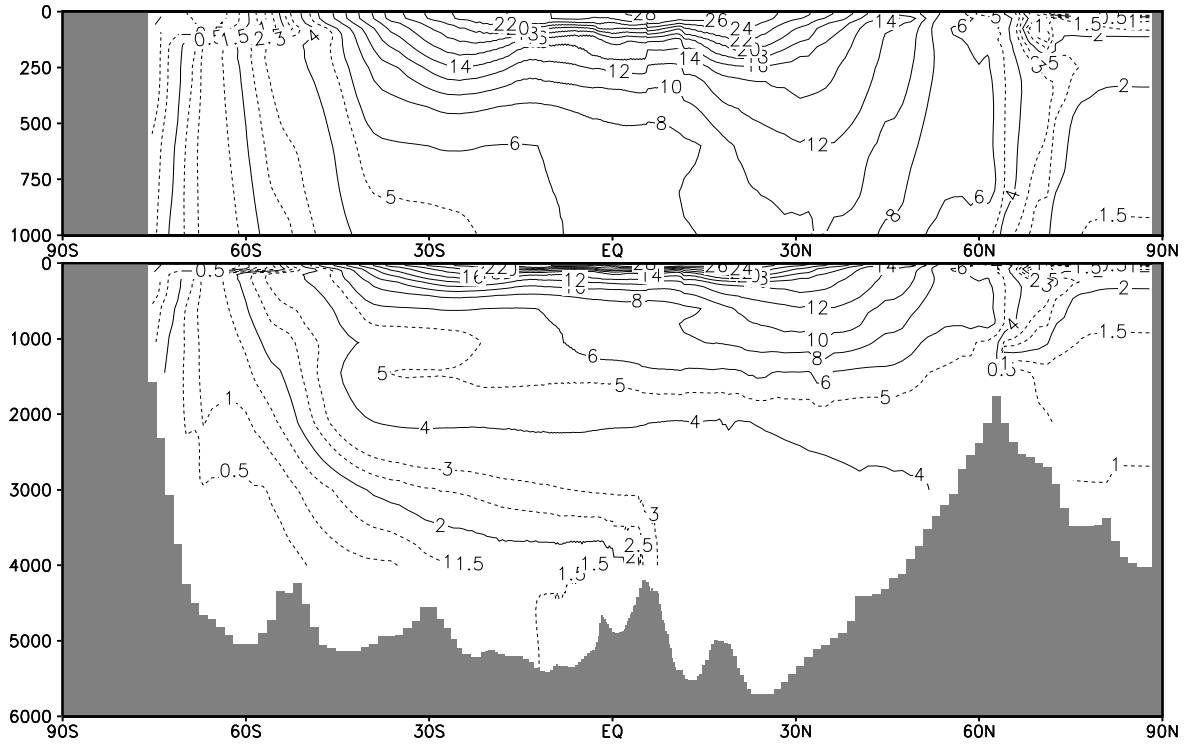

Figure 21a: Simulated zonal-mean temperature in the Atlantic Ocean.

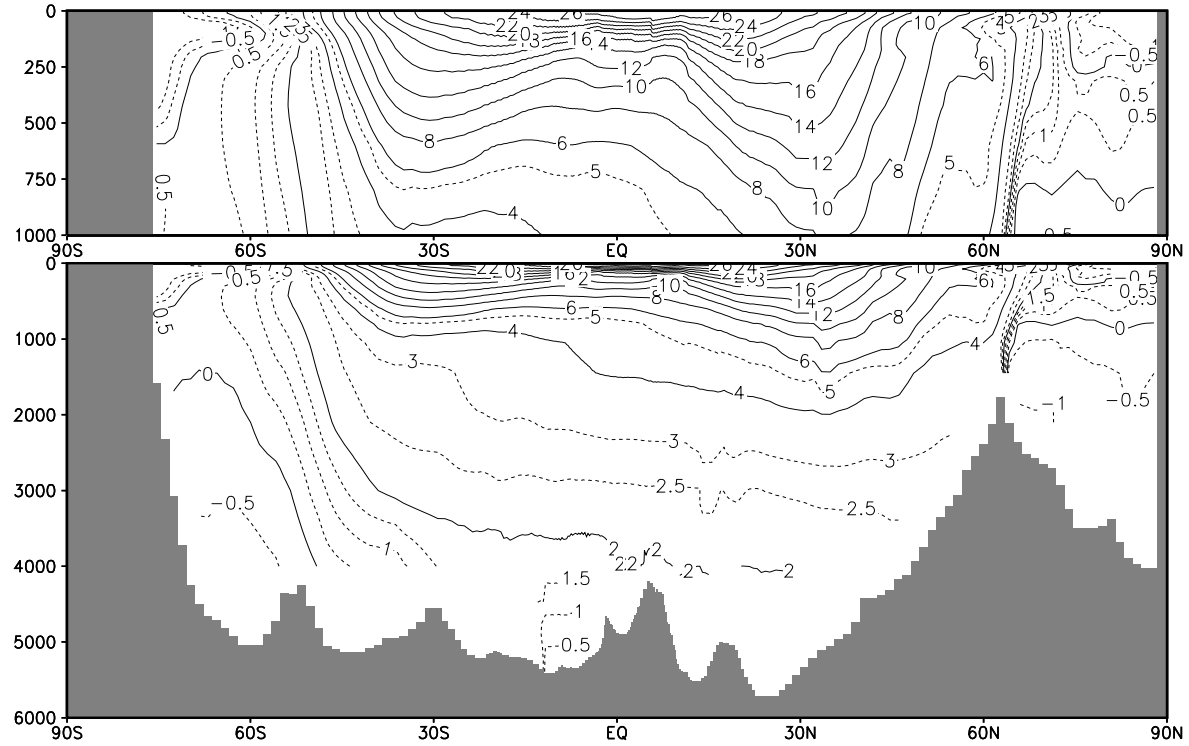

Figure 21b: Observed (Levitus et al. 1994) zonal-mean temperature in the Atlantic Ocean interpolated onto the model grid.

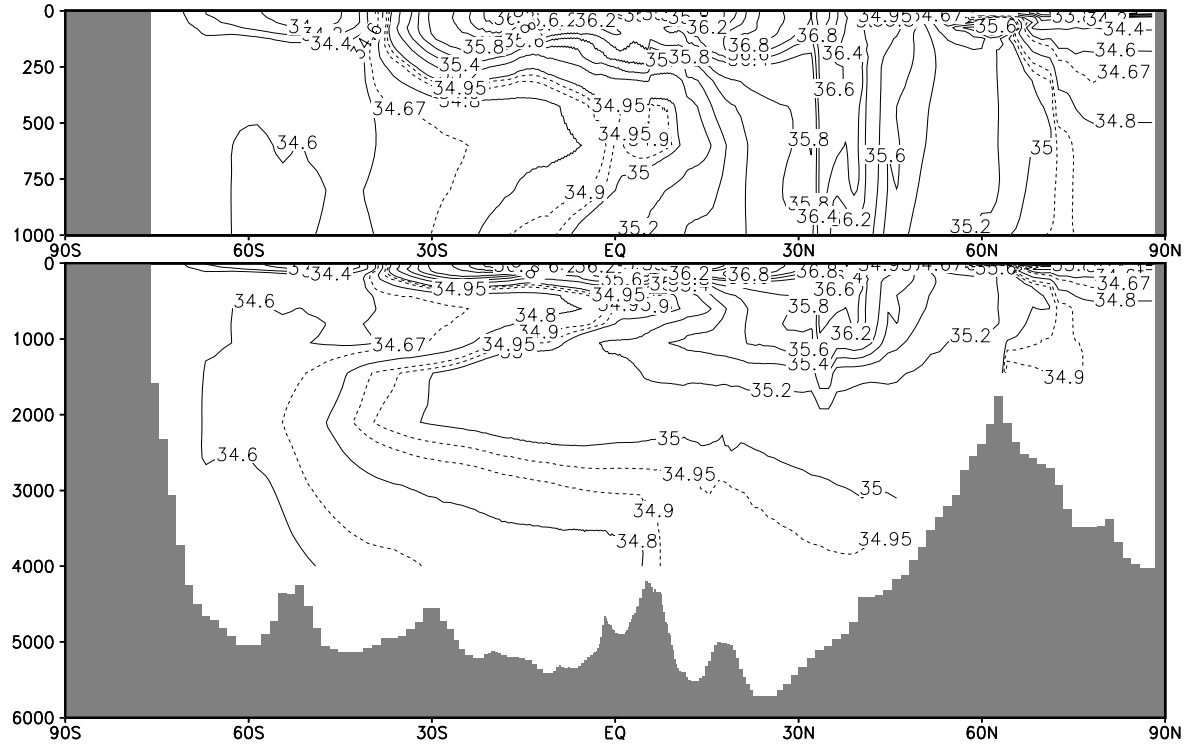

Figure 21c: Simulated zonal-mean salinity in the Atlantic Ocean.

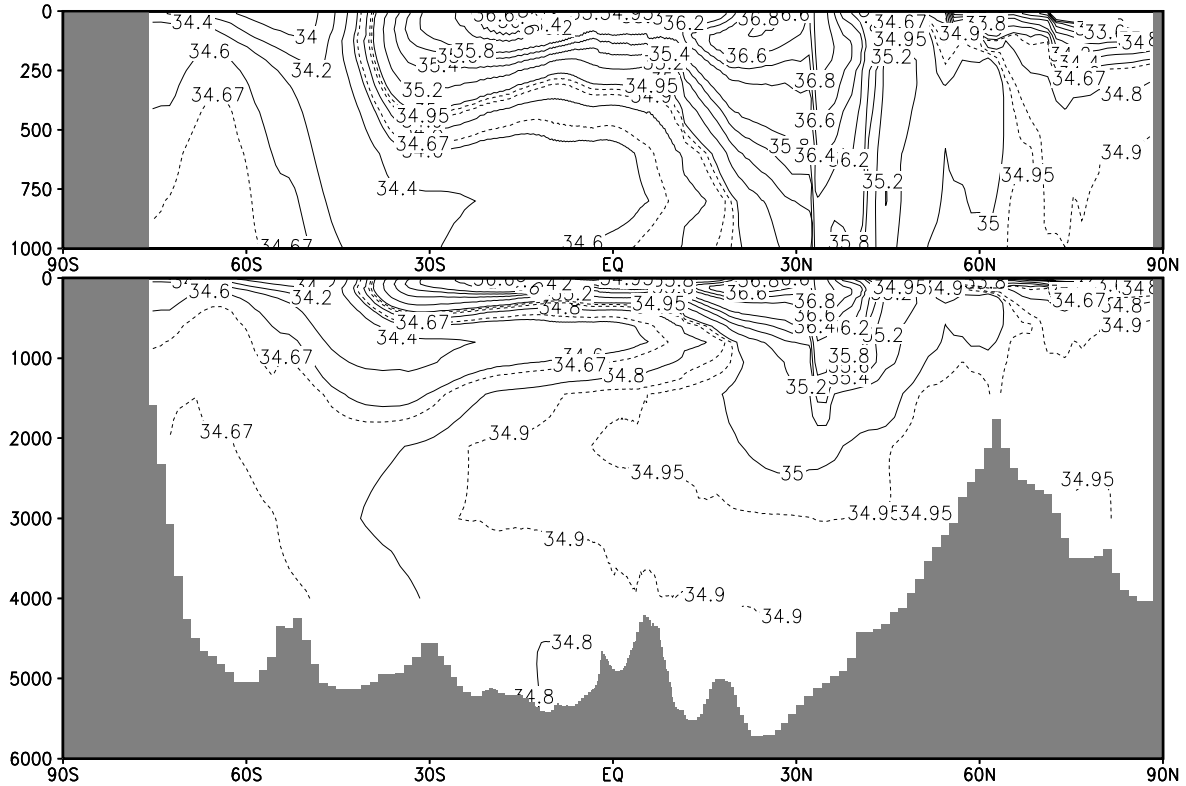

Figure 21d: Observed (Levitus et al. 1994) zonal-mean salinity in the Atlantic Ocean interpolated onto the model grid.

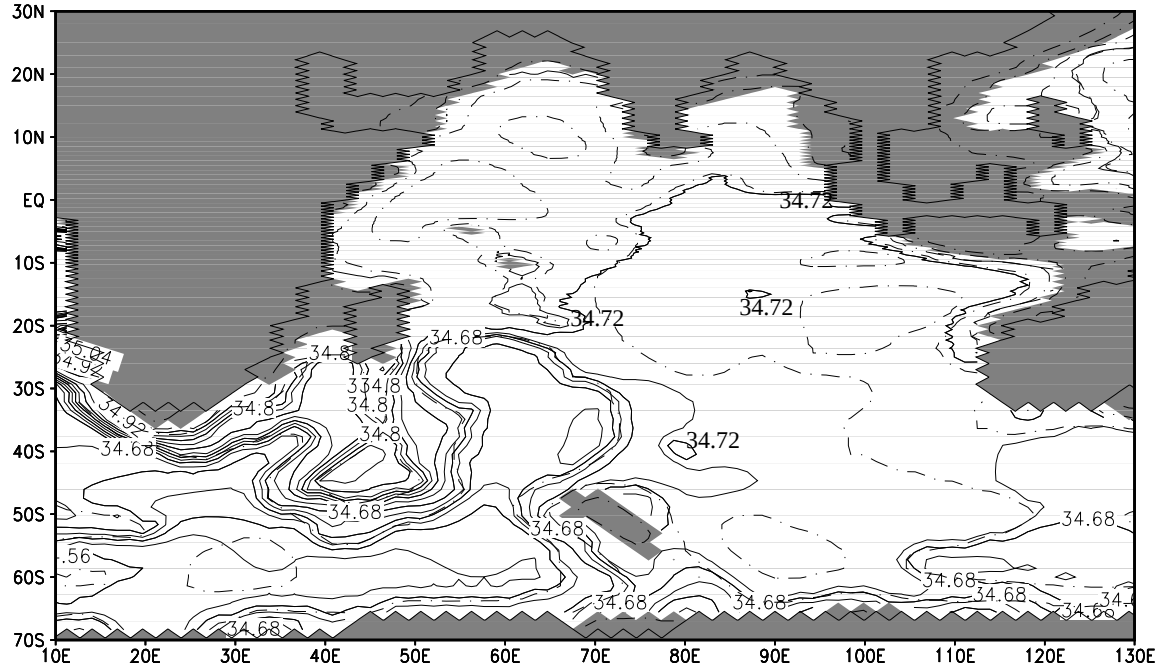

Figure 22a: Simulated bottom salinity for water depths > 2100 m in the Indian Ocean. Contour interval is 0.02 psu.

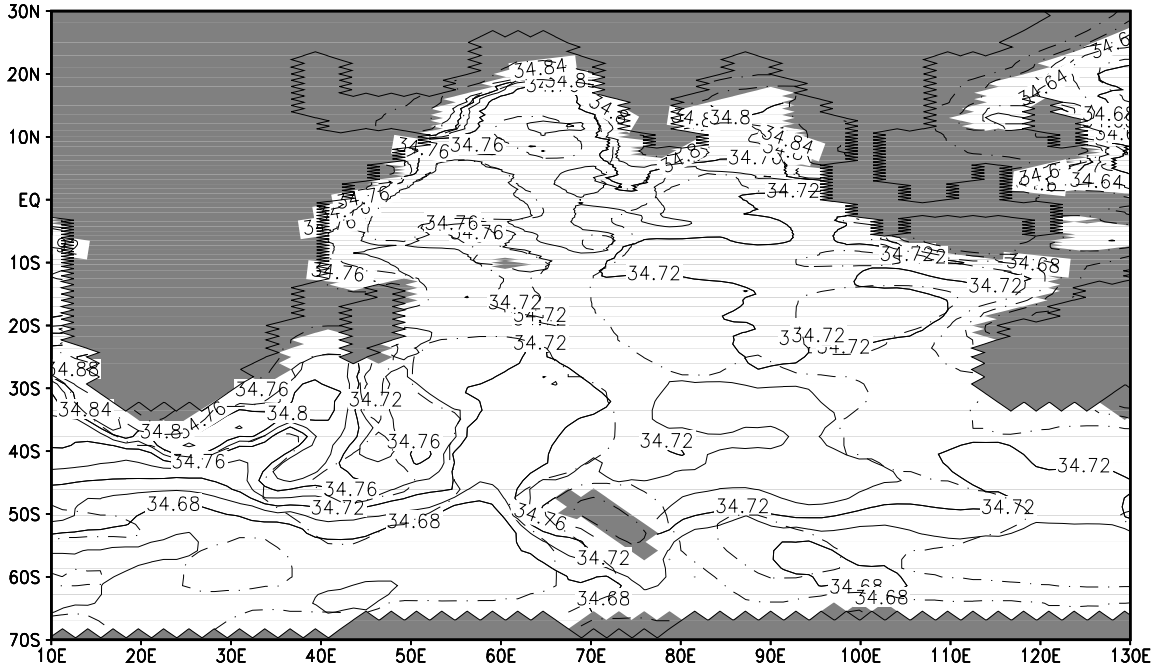

Figure 22b: Observed (Levitus et al. 1994) bottom salinity for water depths > 2100 m in the Indian Ocean. Contour interval is 0.02 psu.

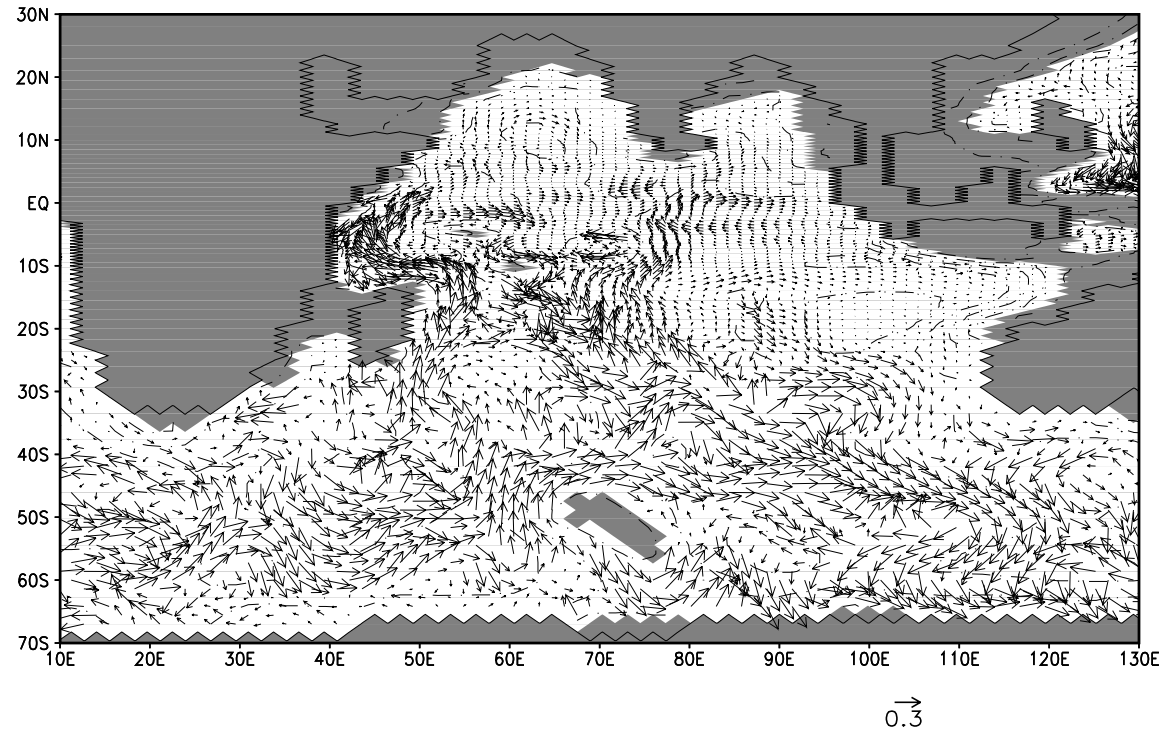

Figure 23: Horizontal bottom velocities for water depths > 2100 m in the Indian Ocean. The speed is proportional to the arrow length if it is below 0.3 cm s^{-1}. Higher speeds have an arrow length of 1 zonal gridpoint distance.

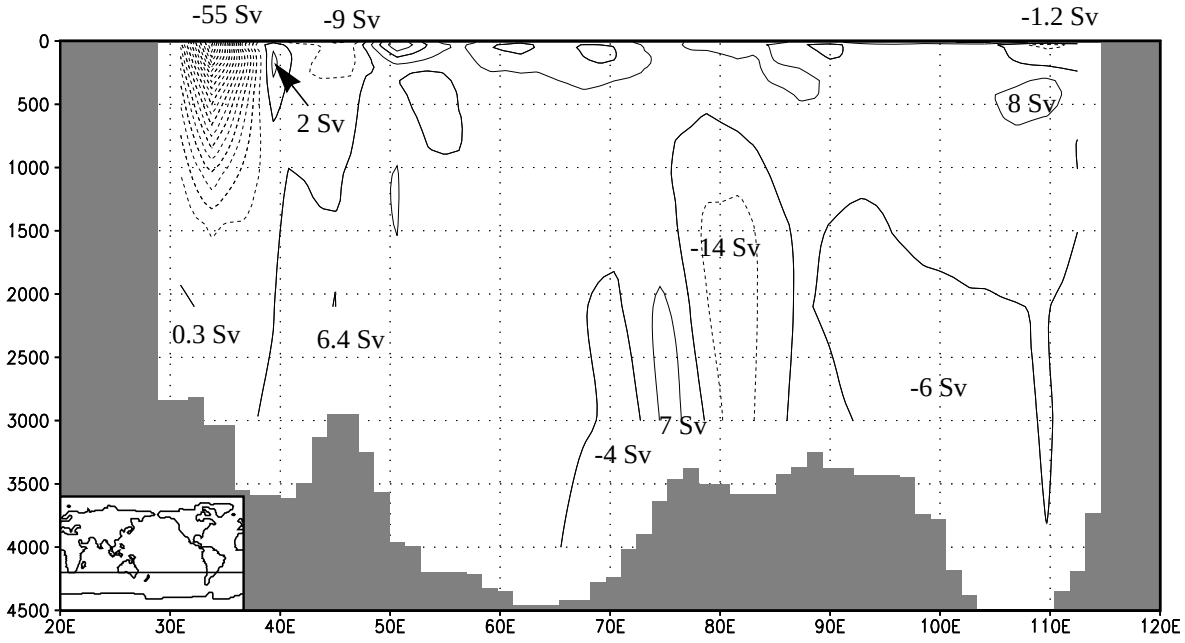

Figure 24: Meridional velocity at 32^o S in the Indian Ocean. Contour interval is 1 cm s^{-1}. Dashed lines indicate a southward direction. The figures give volume transports in 10^6 m^3 s^{-1}.

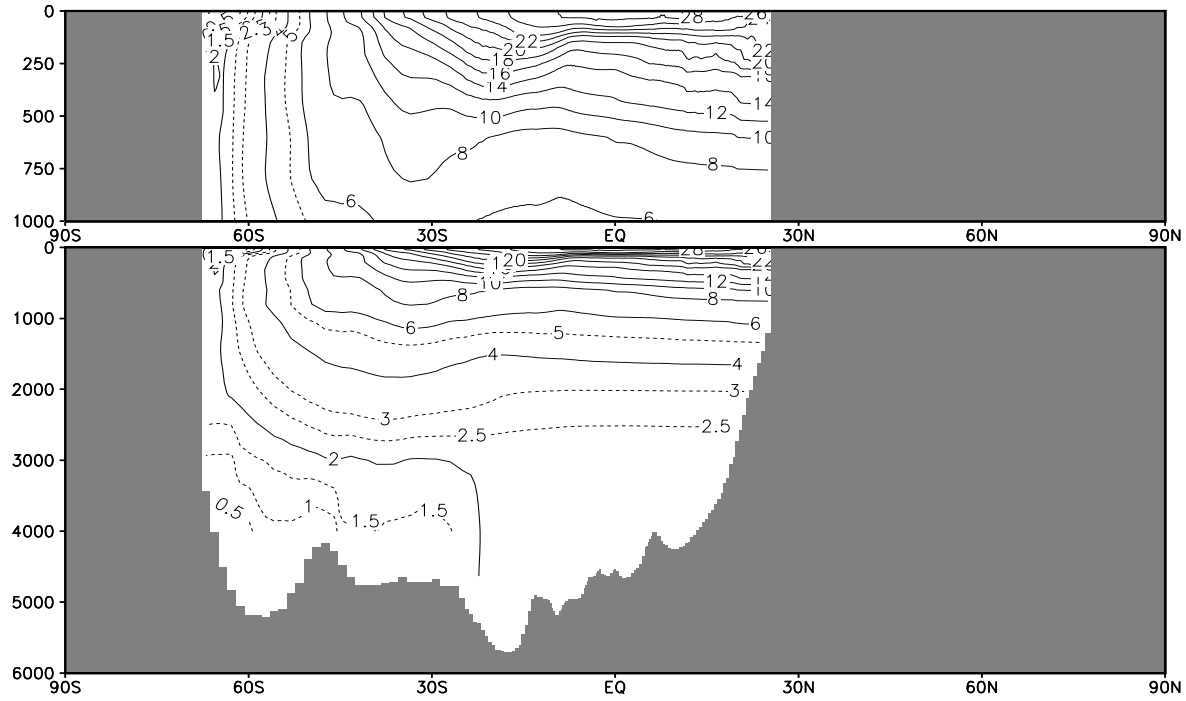

Figure 25a: Simulated zonal-mean temperature in the Indian Ocean.

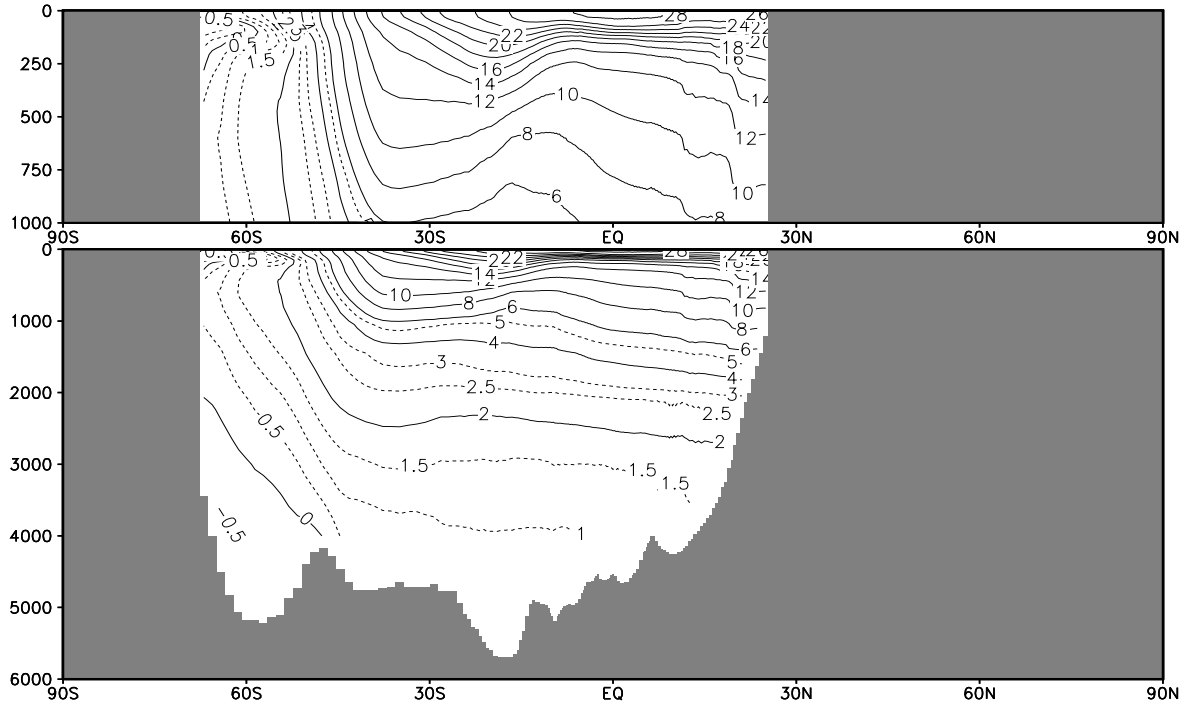

Figure 25b: Observed (Levitus et al. 1994) zonal-mean temperature in the Indian Ocean interpolated onto the model grid.

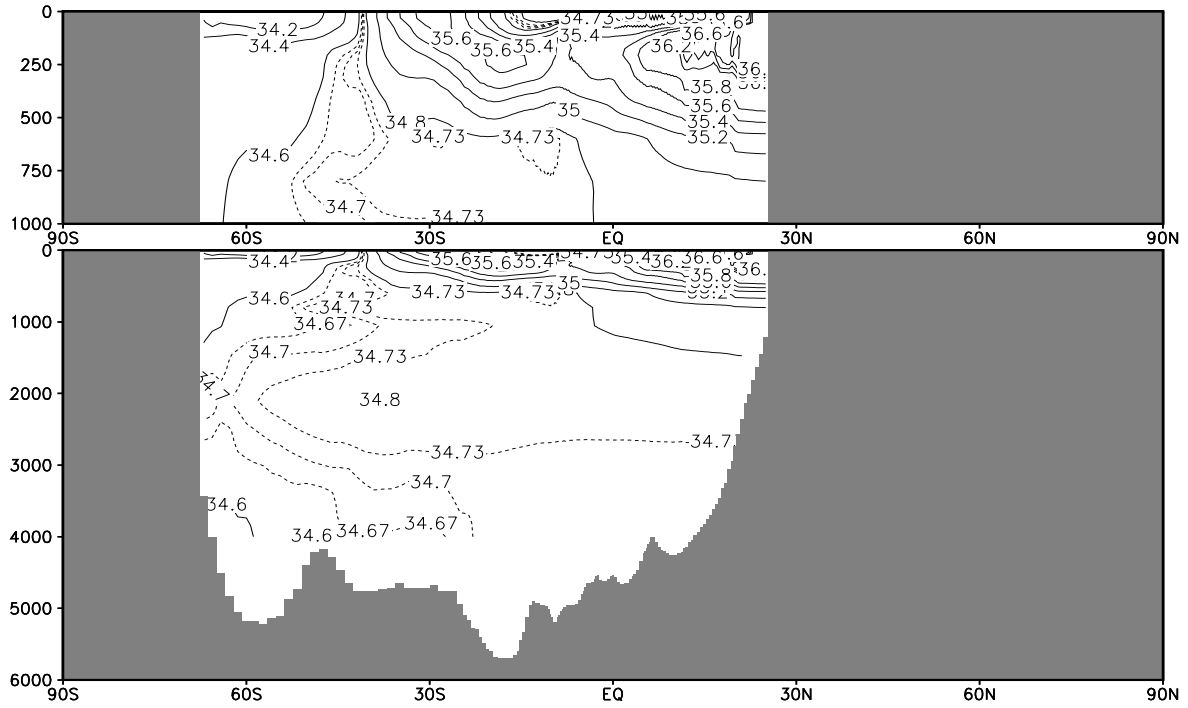

Figure 25c: Simulated zonal-mean salinity in the Indian Ocean.

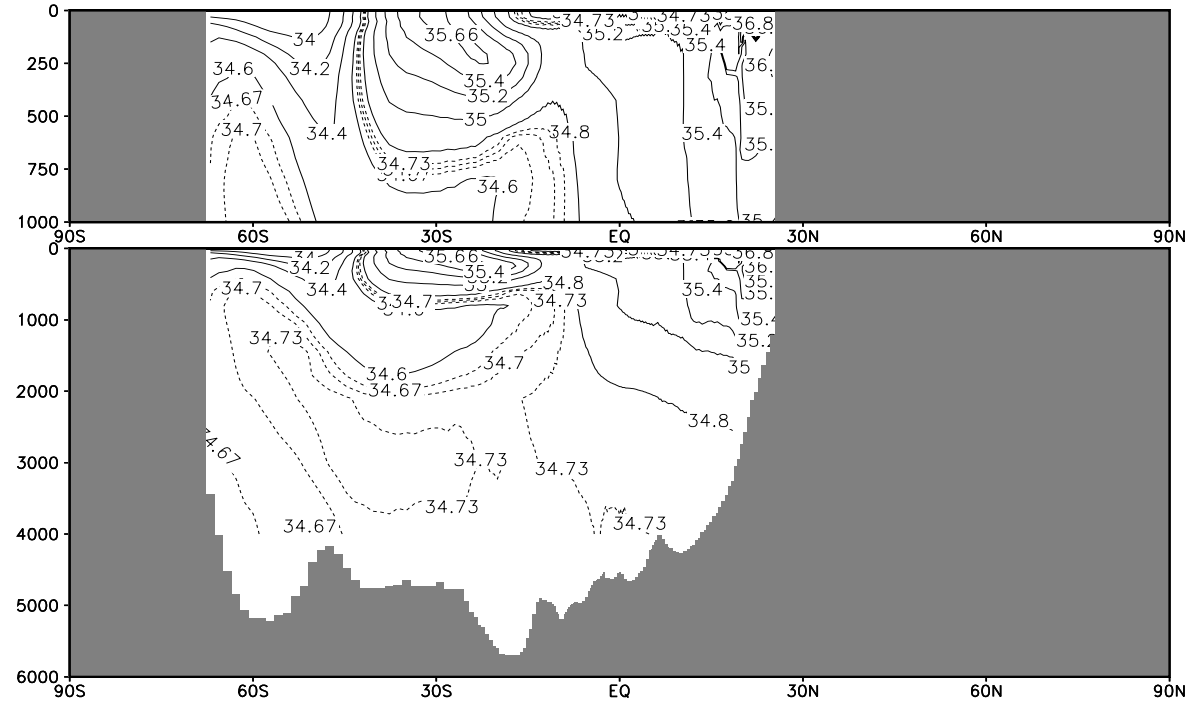

Figure 25d: Observed (Levitus et al. 1994) zonal-mean salinity in the Indian Ocean interpolated onto the model grid.

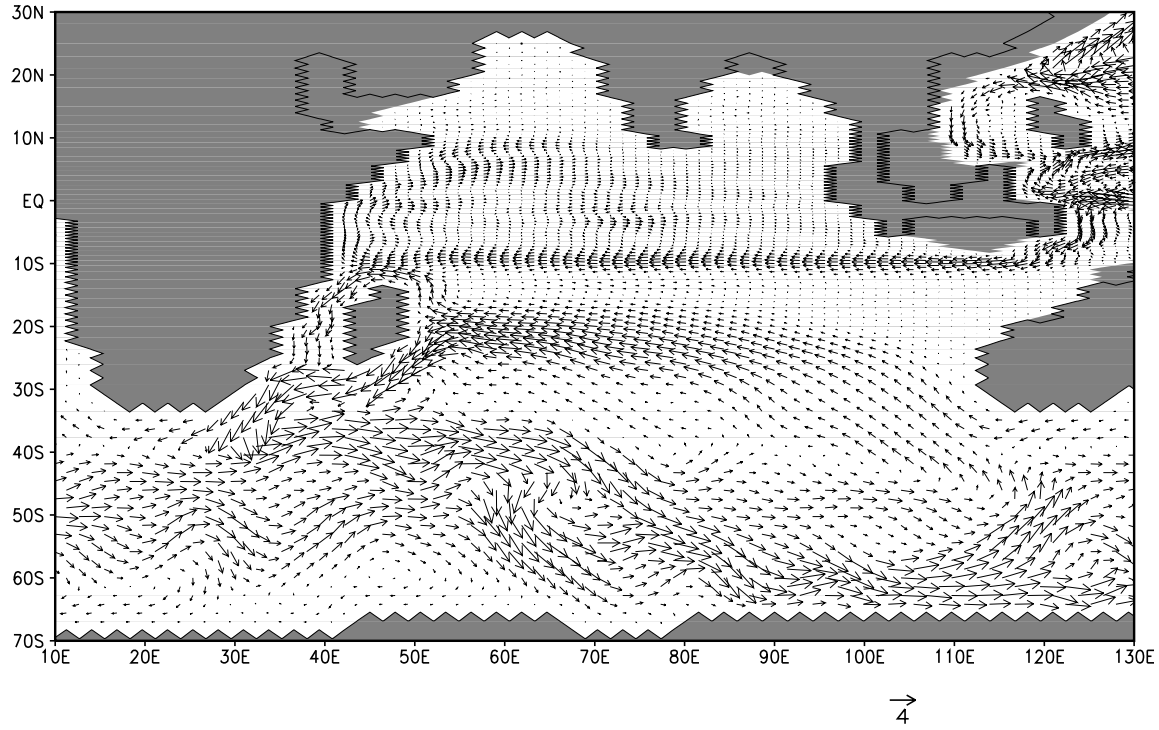

Figure 26a: Annual-mean horizontal velocity at 600 m in the Indian Ocean. Arrows which represent a speed of more than 4 cm s^{-1} are truncated to one zonal gridpoint distance.

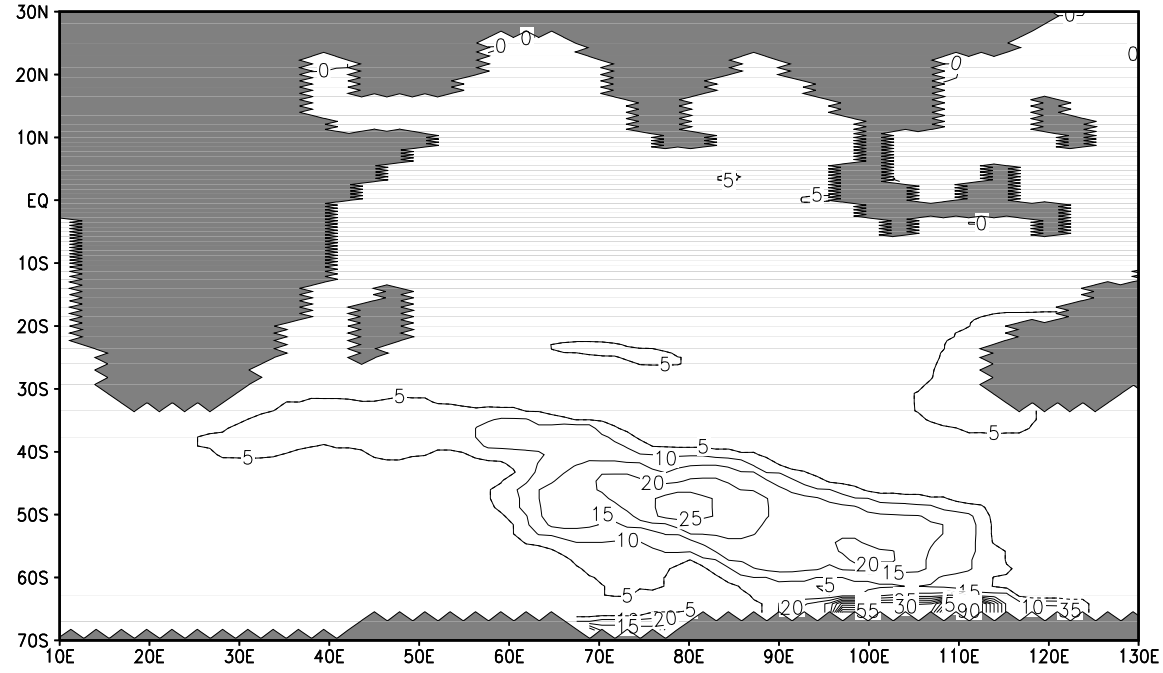

Figure 26b: Mean potential energy (10^{-3}W m^{-2}) lost by convective adjustment in July in the Indian Ocean.

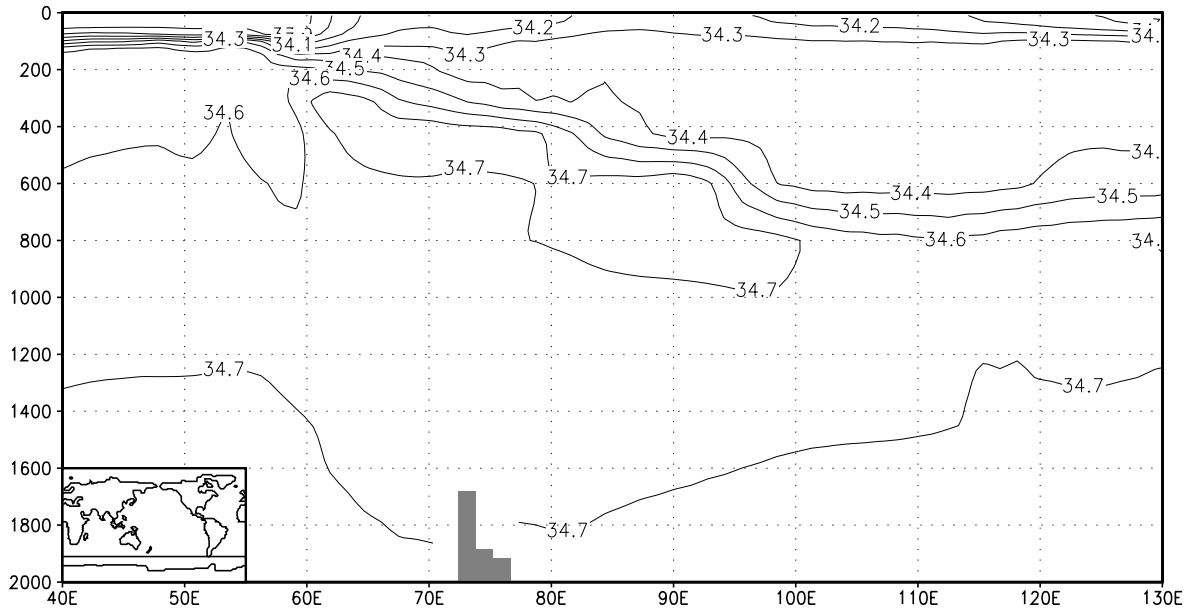

Figure 26c: Mean salinity in September at 53^{o} S in the Indian Ocean. Contour interval is 0.1 psu.

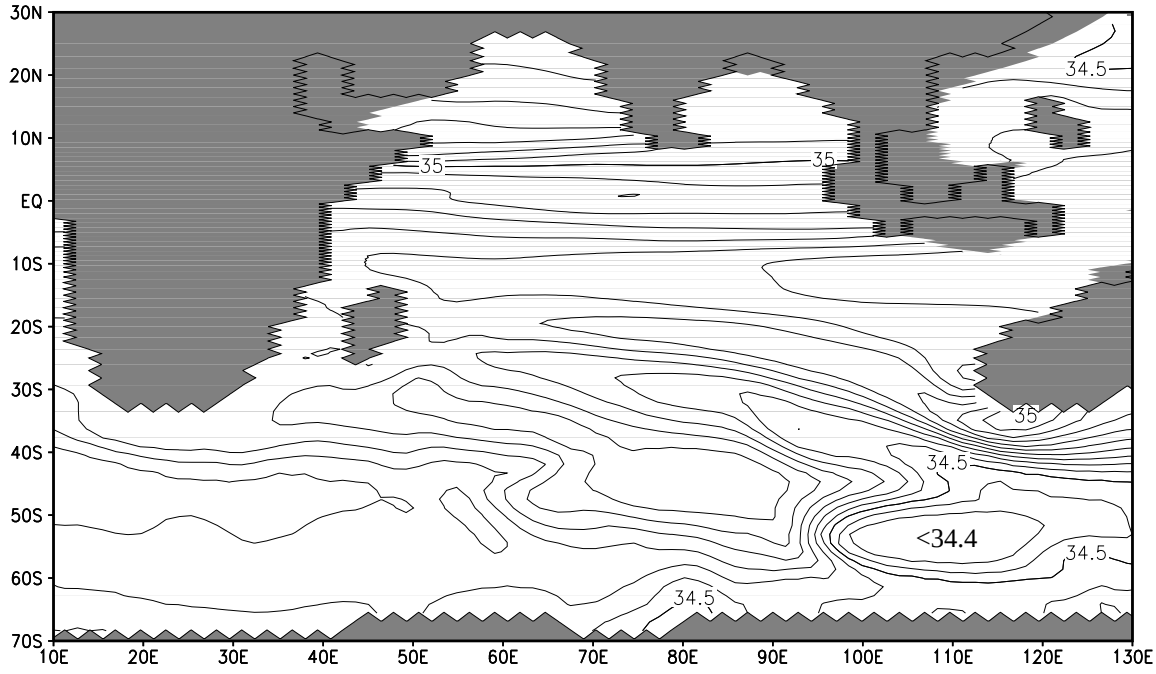

Figure 26d: Simulated mean salinity in September in 600 in the Indian Ocean. Contour interval is 0.05 psu.

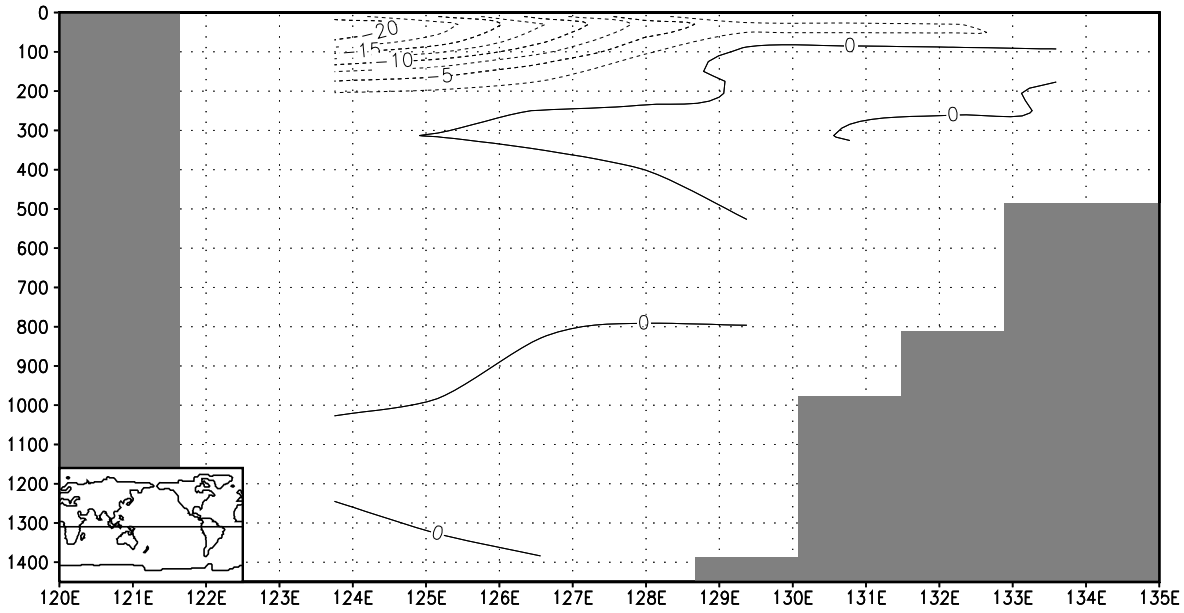

Figure 27: Simulated annual-mean meridional velocity (cm s^{-1}) at 3^{o} S in the Indonesian throughflow region. Contour interval is 2.5 cm s^{-1}. Contours are dashed for southward flow.

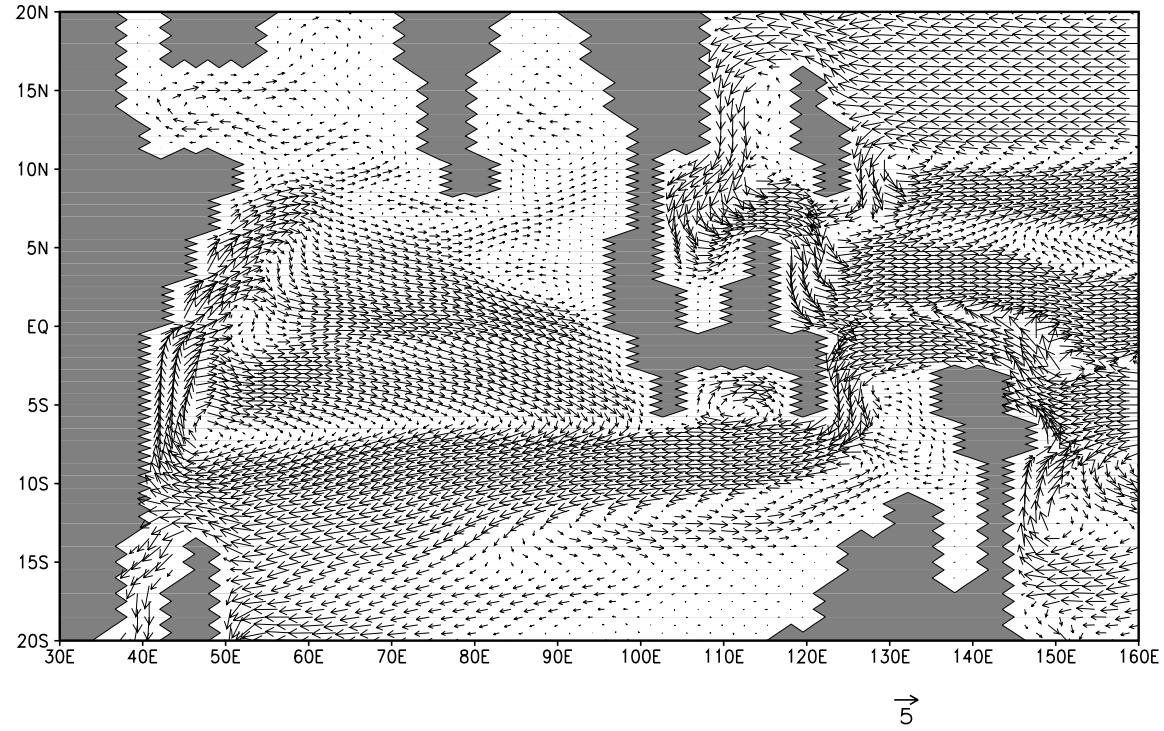

Figure 28a: Simulated annual-mean velocity in the upper (0-250 m) Indian Ocean and the Indonesian throughflow region. Arrows which represent a speed of more than 5 cm s^{-1} are truncated.

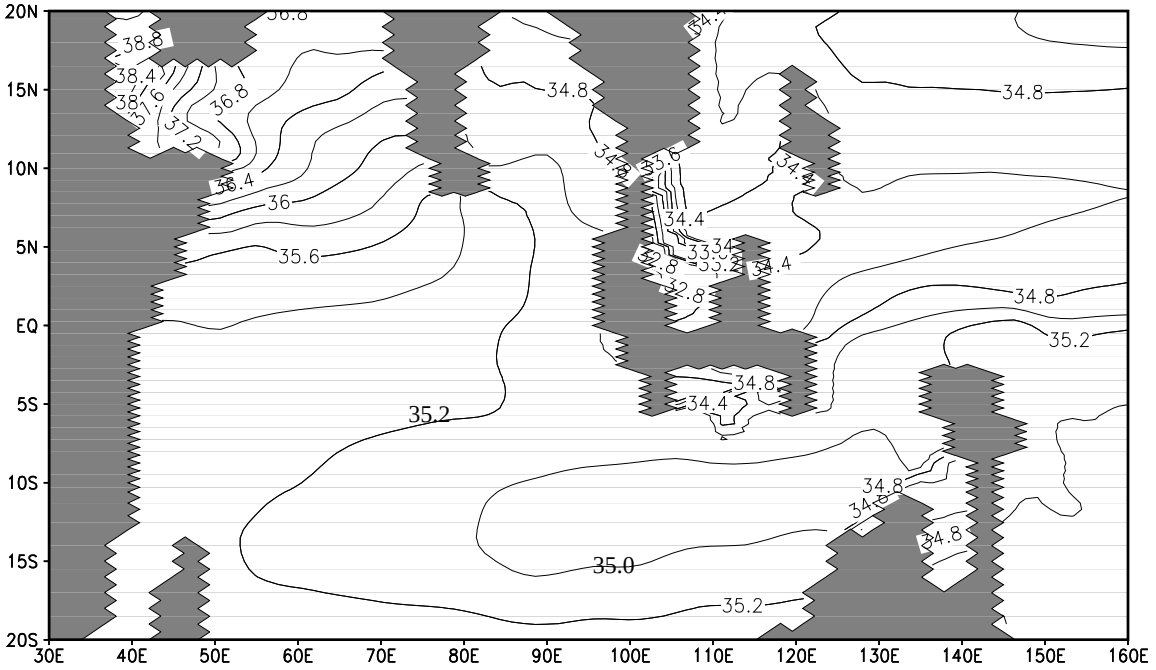

Figure 28b: Simulated annual-mean salinity in the upper (0-250 m) Indian Ocean and the Indonesian throughflow region. Contour intervall is 0.2 psu.

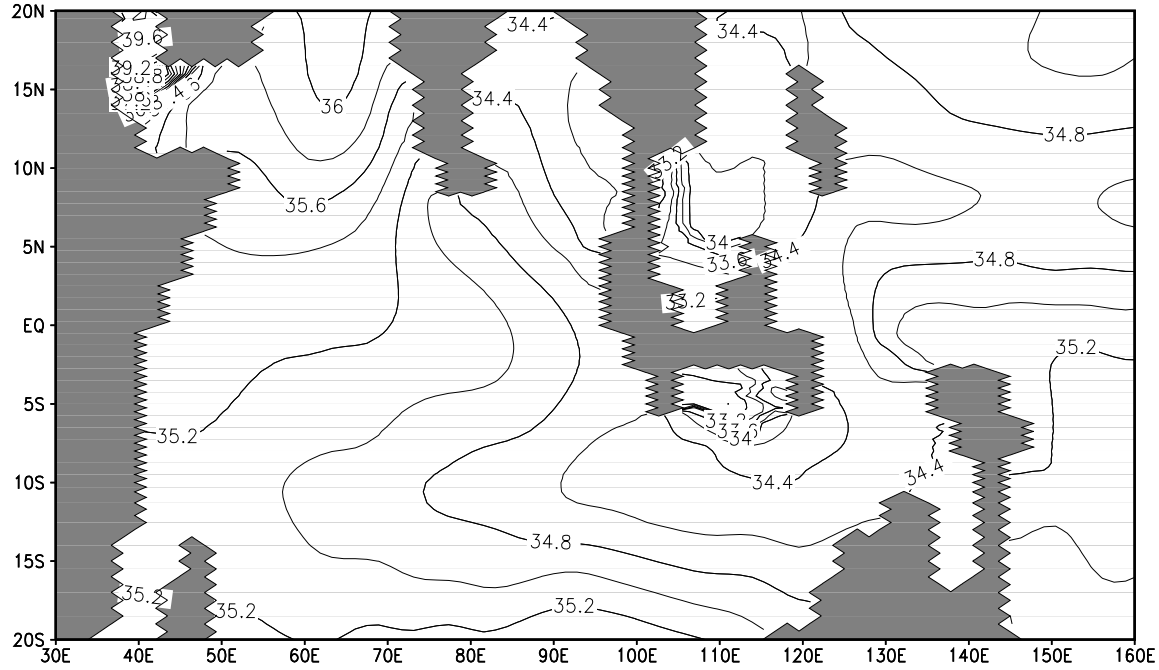

Figure 28c: Observed (Levitus et al. 1994) annual-mean salinity in the upper (0-250 m) Indian Ocean and the Indonesian throughflow region. Contour intervall is 0.2 psu.

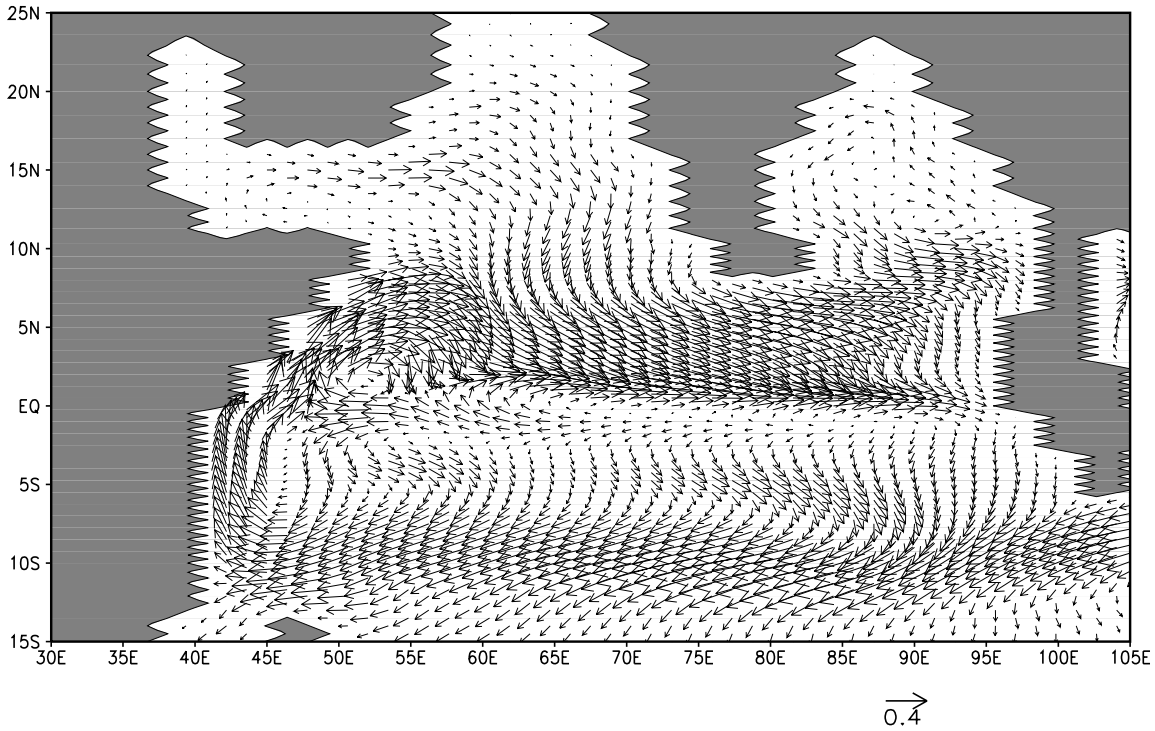

Figure 29a: Simulated mean upper-layer velocity in August in the Indian Ocean.
Arrows which represent a speed of more than 40 cm s^{-1} are truncated to one zonal gridpoint distance.

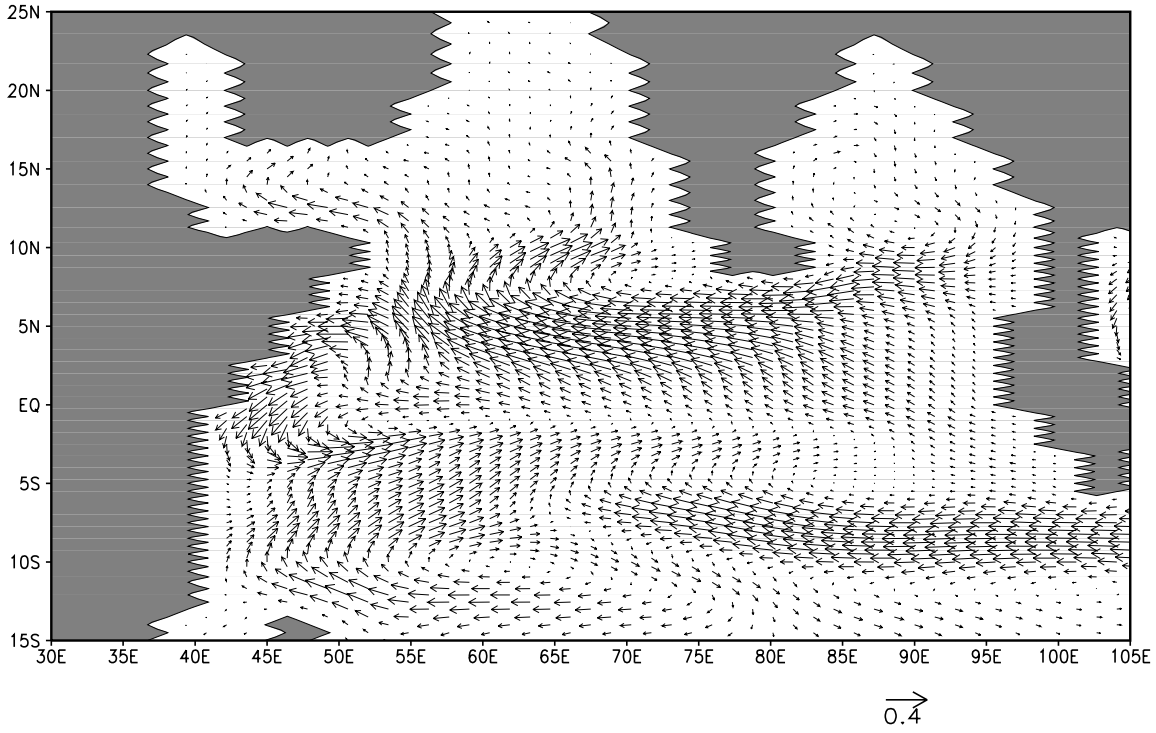

Figure 29b: Simulated mean upper-layer velocity in February in the Indian Ocean.
Arrows which represent a speed of more than 40 cm s^{-1} are truncated to one zonal gridpoint distance.

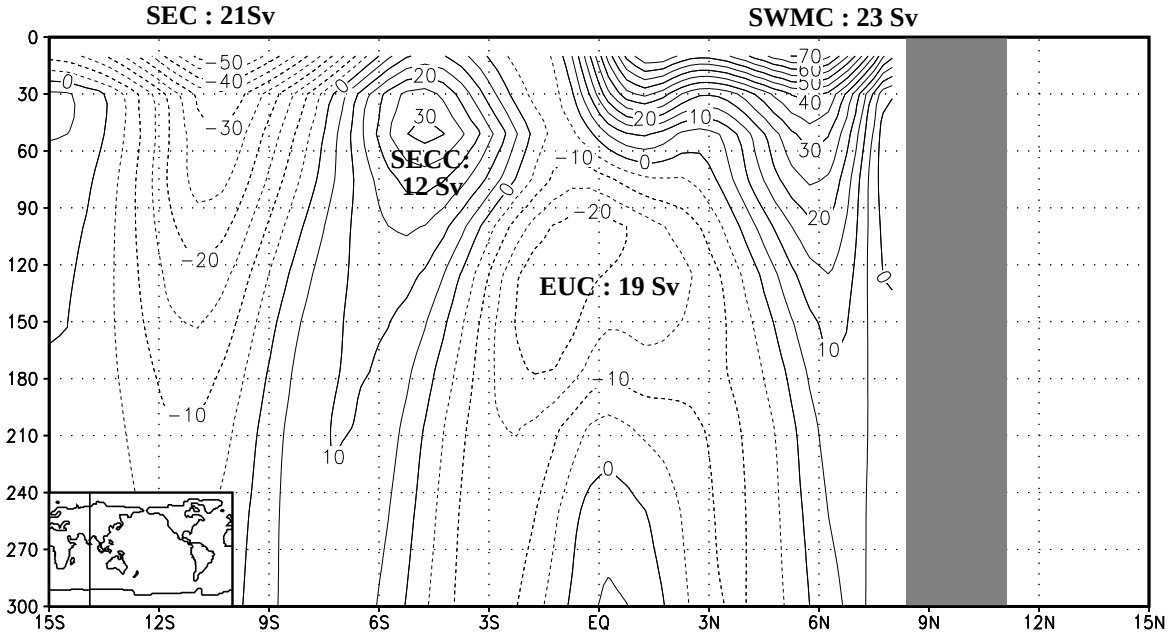

Figure 30a: Simulated zonal currents at 80^{o} E in the equatorial Indian Ocean in August . The figures included give zonal transports in 10^6 m^3 s^{-1}. Contour interval is 5 cm s^{-1}. Westward velocity contours are dashed. The abbreviations are explained in the text.

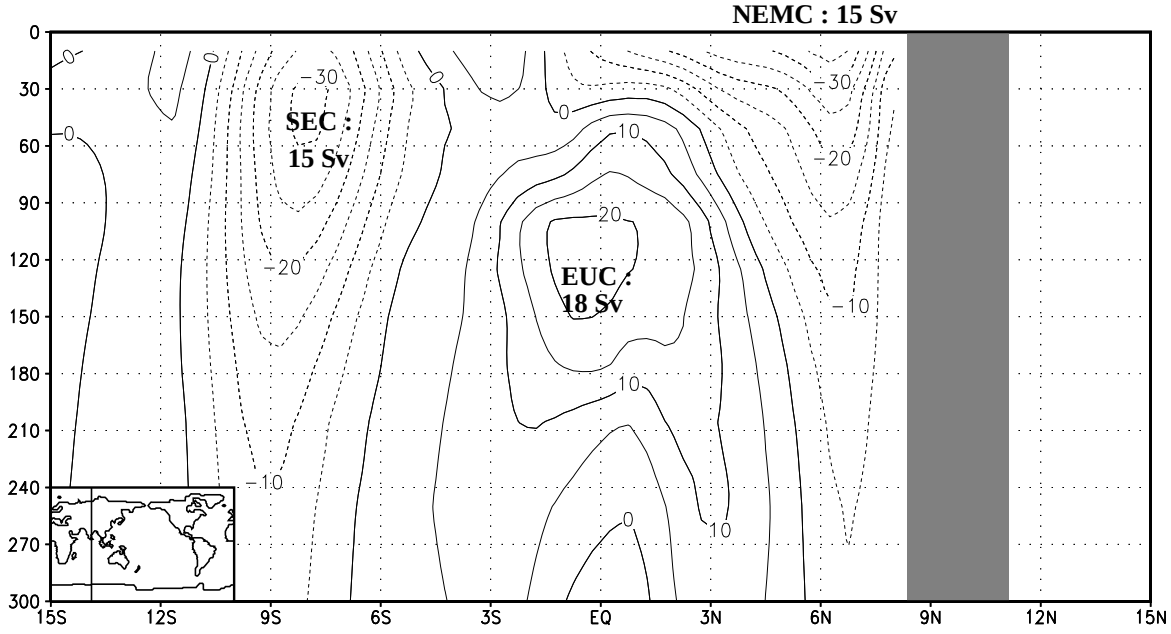

Figure 30b: Simulated zonal currents at 80^{o} E in the equatorial Indian Ocean in February. The figures included give zonal transports in 10^6 m^3 s^{-1}. Westward velocity contours are dashed. Contour interval is 5 cm s^{-1}. The abbreviations are explained in the text.

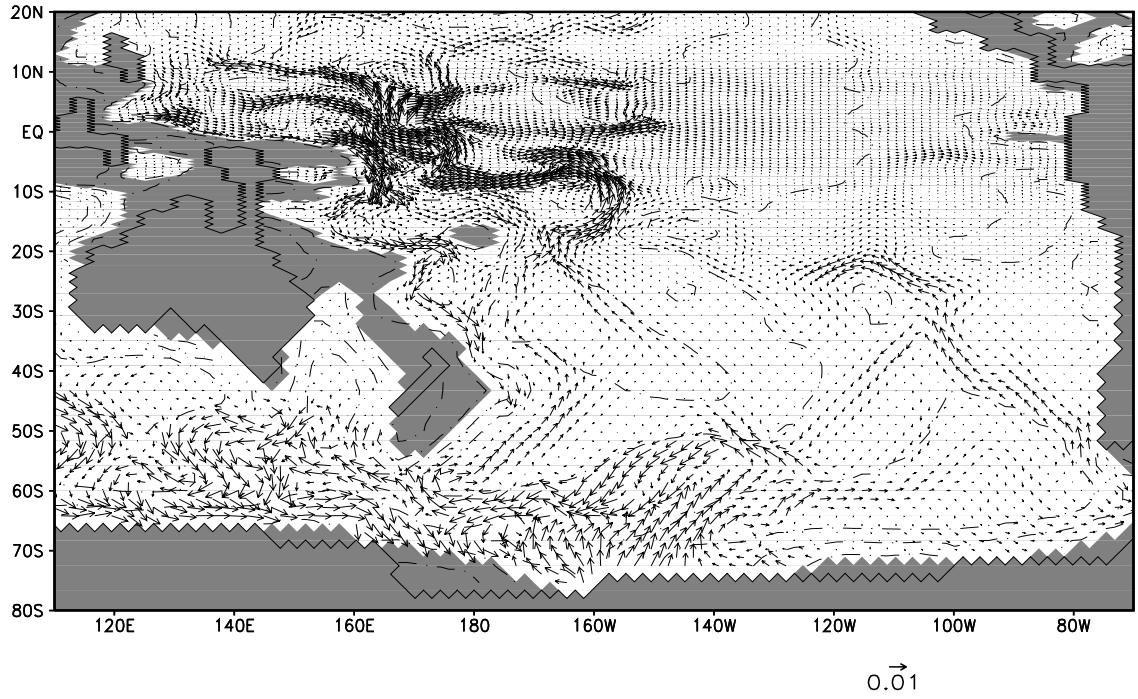

Figure 31: Horizontal bottom velocities for water depths > 2100 m in the Pacific Ocean. Arrows which represent a speed above 1 cm s^{-1} are truncated to one zonal gridpoint distance.

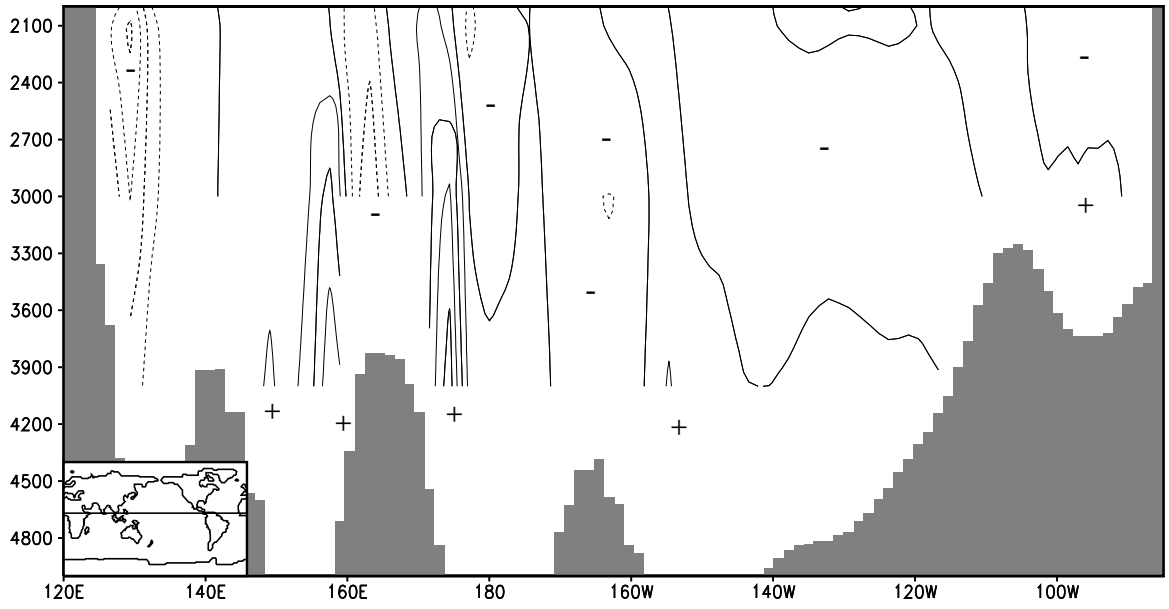

Figure 32: Meridional velocity below 2000 m at 10^{o} N in the Pacific Ocean.
Contour interval is 0.1 cm s^{-1}. Negative contours are dashed.

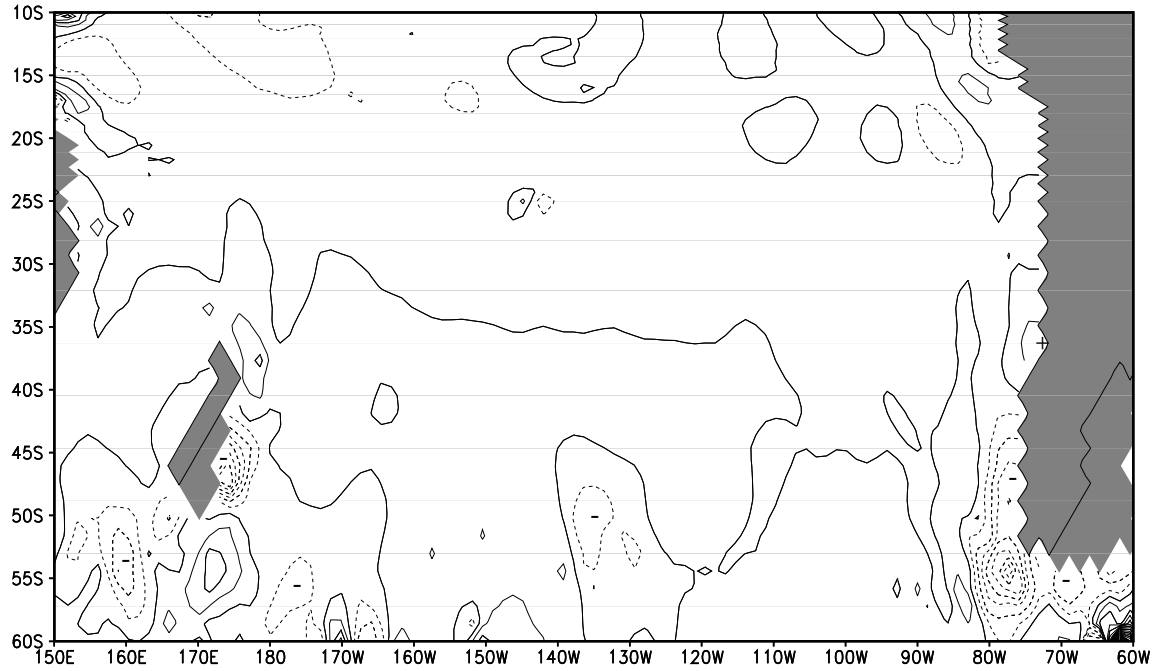

Figure 33a: Vertical velocityat 800 m depth in the South Pacific Ocean. C.I. = $2 \cdot 10^{-6} ms^{-1}$, negative (downward) contours are dashed.

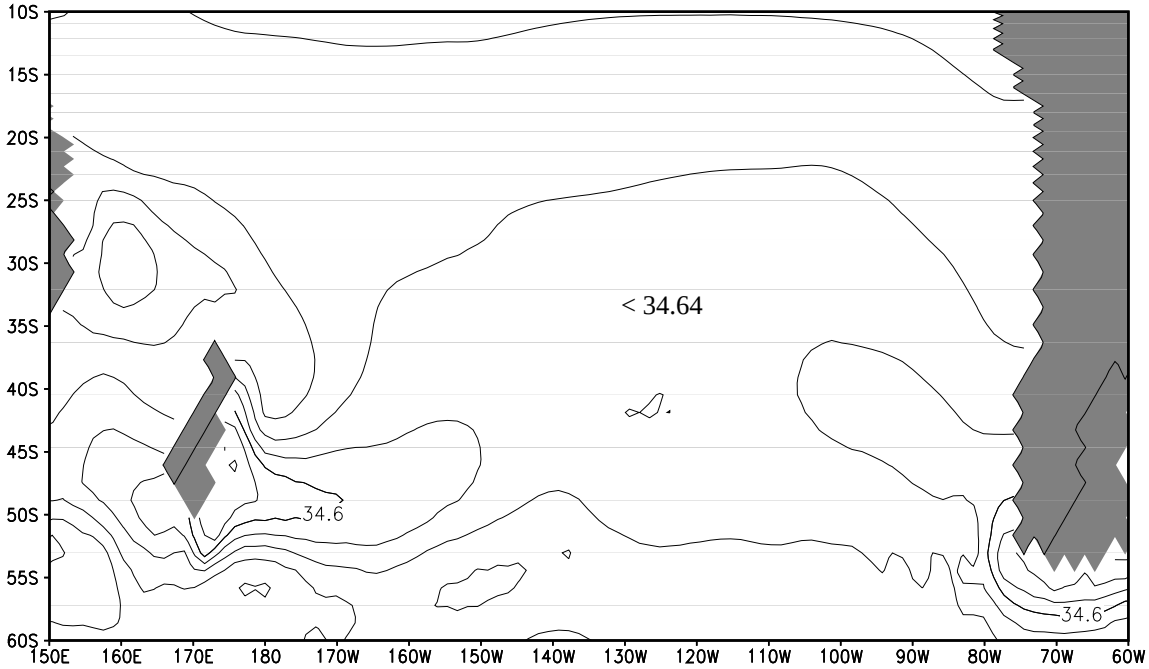

Figure 33b: Simulated salinity at 800 m depth in the South Pacific Ocean. C.I. = 0.02 psu.

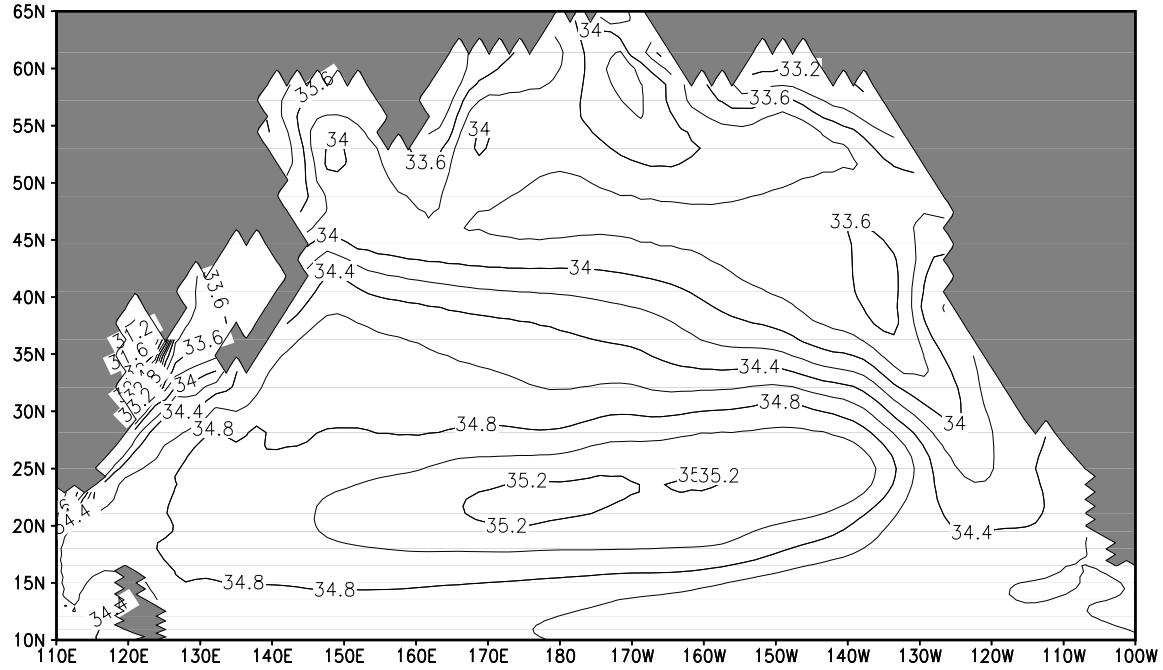

Figure 34a: Simulated annual-mean salinity in the upper 190 m of the North Pacific.

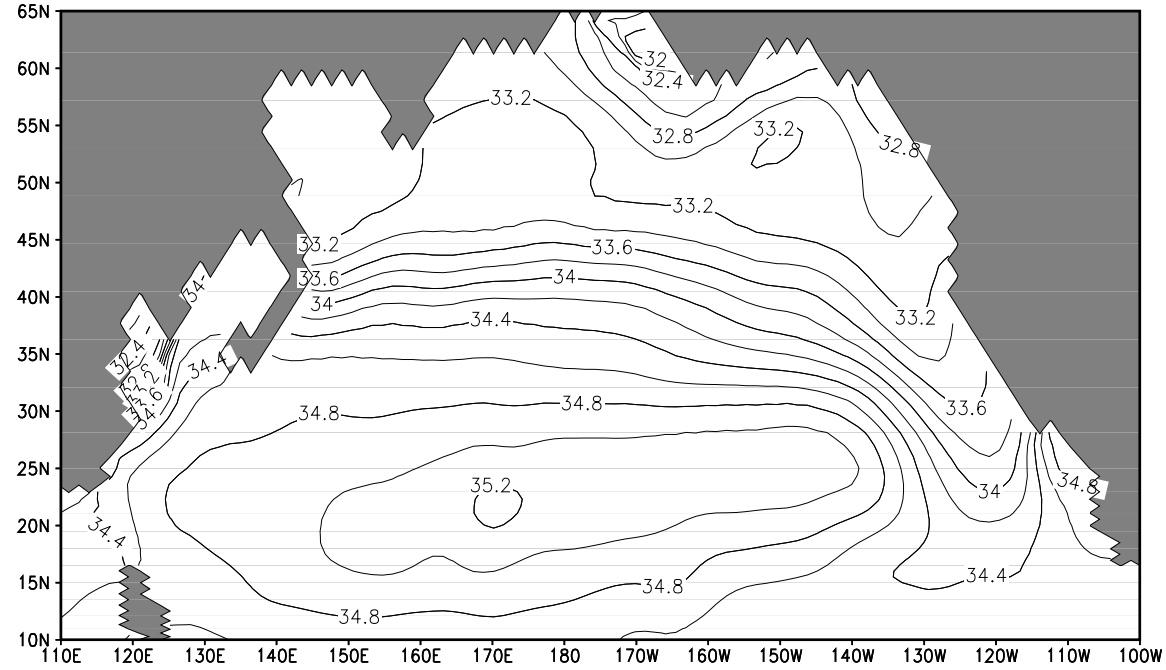

Figure 34b: Observed (Levitus et al. 1994) annual-mean salinity in the upper 190 m of the North Pacific.

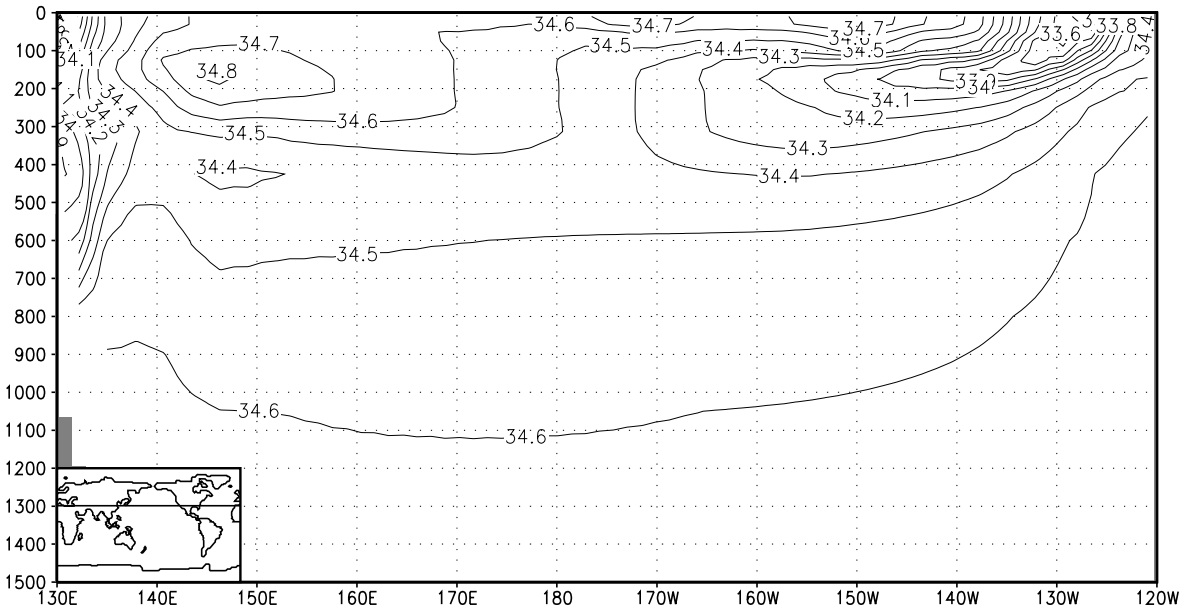

Figure 35a: Simulated annual-mean vertical distribution of salinity at 33^{o} N in the upper 1500 m of Pacific Ocean. C.I = 0.1 psu.

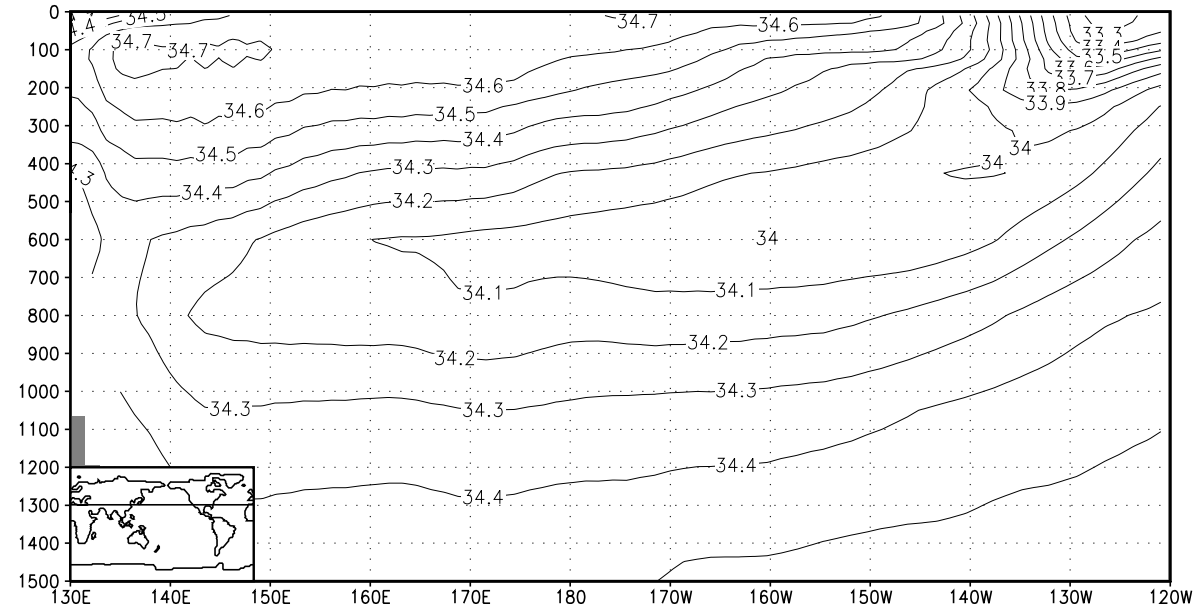

Figure 35b: Climatological (Levitus et al. 1994) annual-mean vertical distribution of salinity at 33^{o} N in the upper 1500 m of Pacific Ocean. C.I. = 0.1 psu.

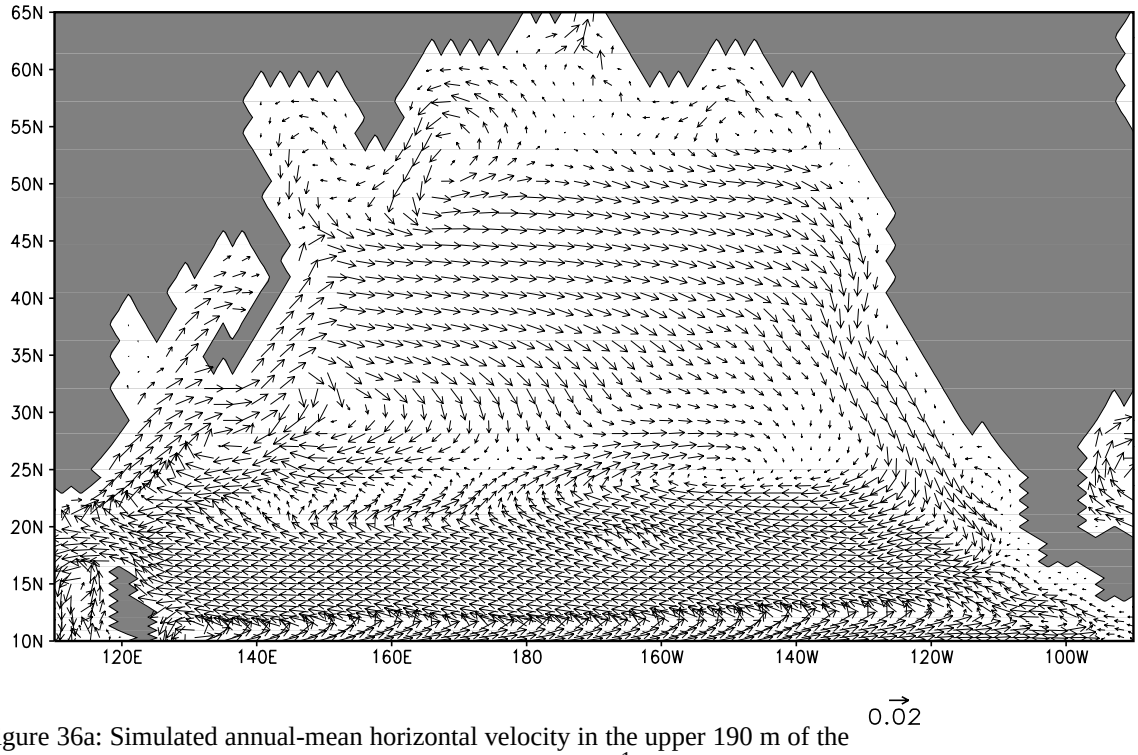

Figure 36a: Simulated annual-mean horizontal velocity in the upper 190 m of the North Pacific. Arrows which represent speeds above 2 cm s^{-1} are truncated to one zonal gridpoint distance.

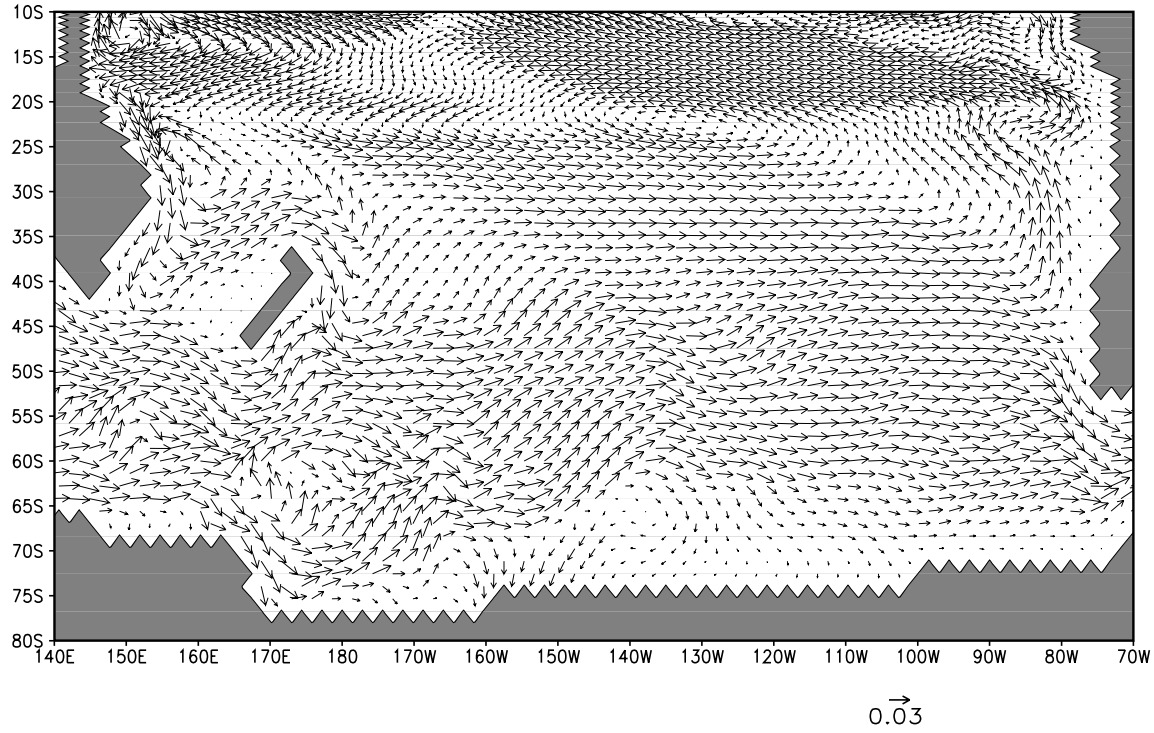

Figure 36b: Simulated annual-mean horizontal velocity in the upper 190 m of the South Pacific. Arrows which represent speeds above 3 cm s^{-1} are truncated to one zonal gridpoint distance.

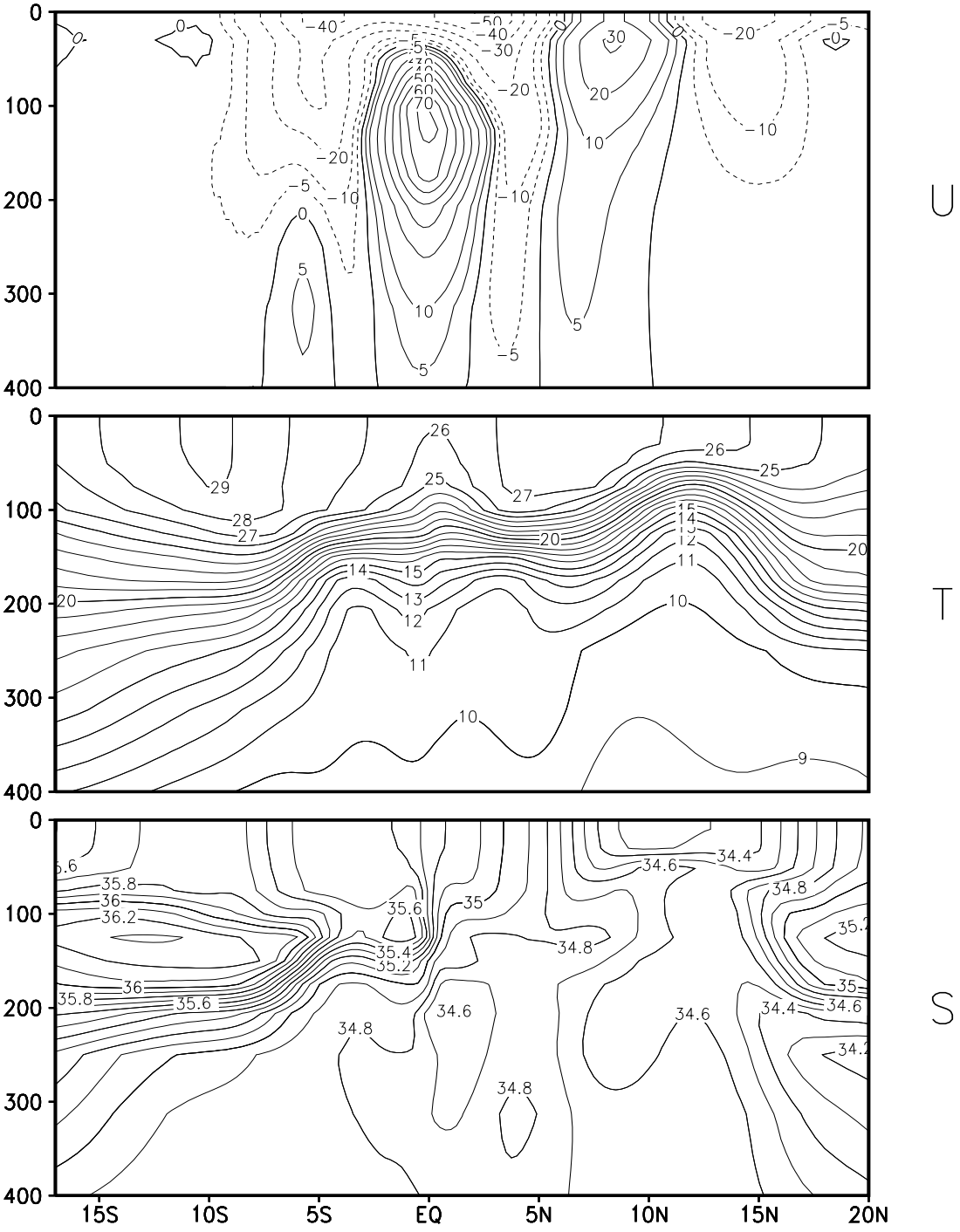

Figure 37: Simulated annual-mean zonal velocity, temperature, and salinity at 140^{o} W in the equatorial Pacific. Units are cm s^{-1}, ^{o}C, and psu. respectively.

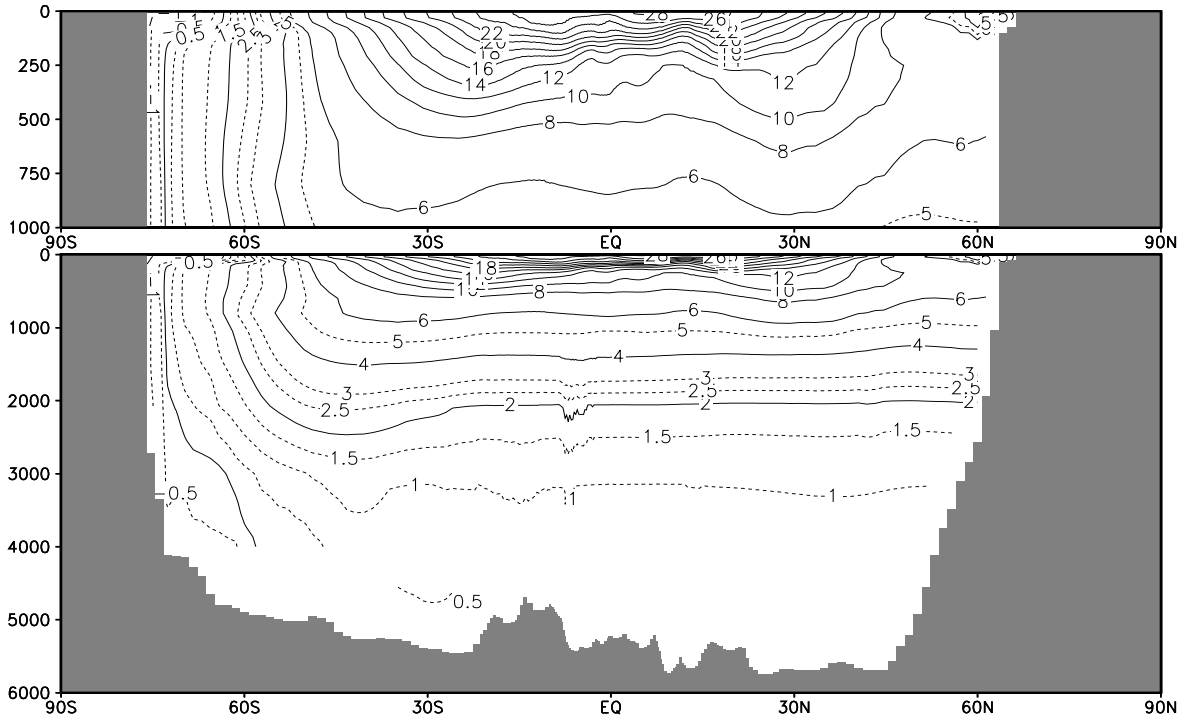

Figure 38a: Simulated zonal-mean potential temperature in the Pacific Ocean.

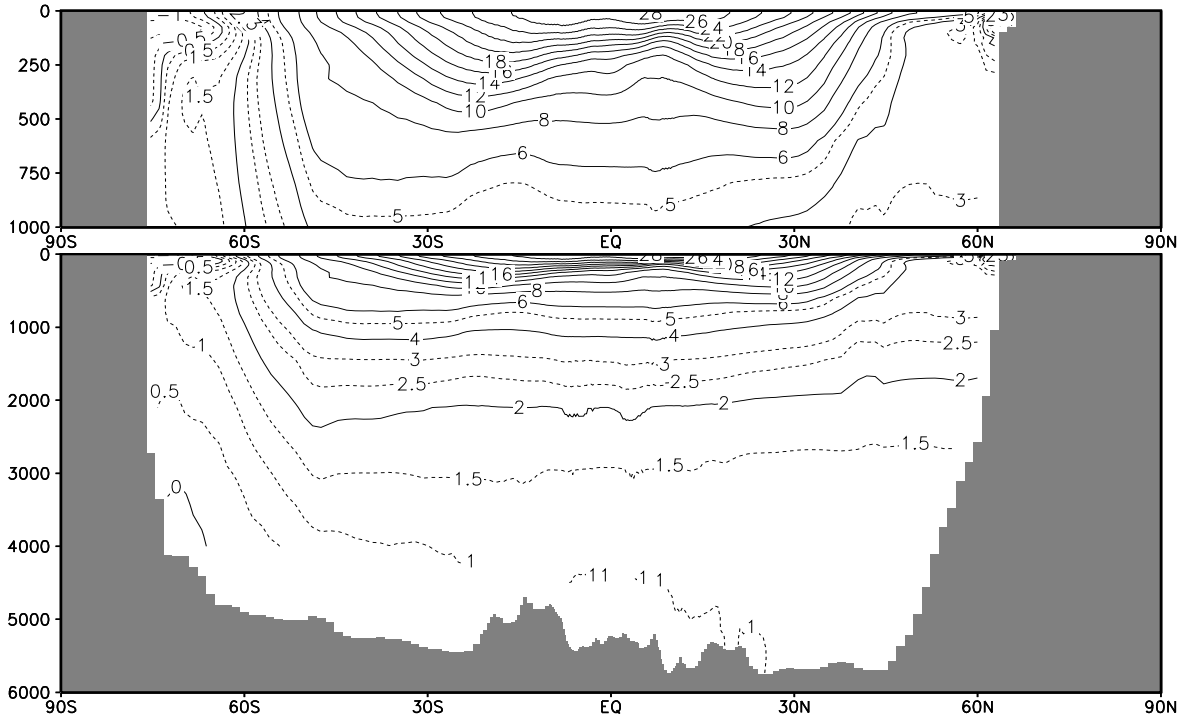

Figure 38b: Observed zonal-mean potential temperature in the Pacific Ocean calculated from the Levitus climatology (Levitus et al. 1994) and interpolated onto the model grid.

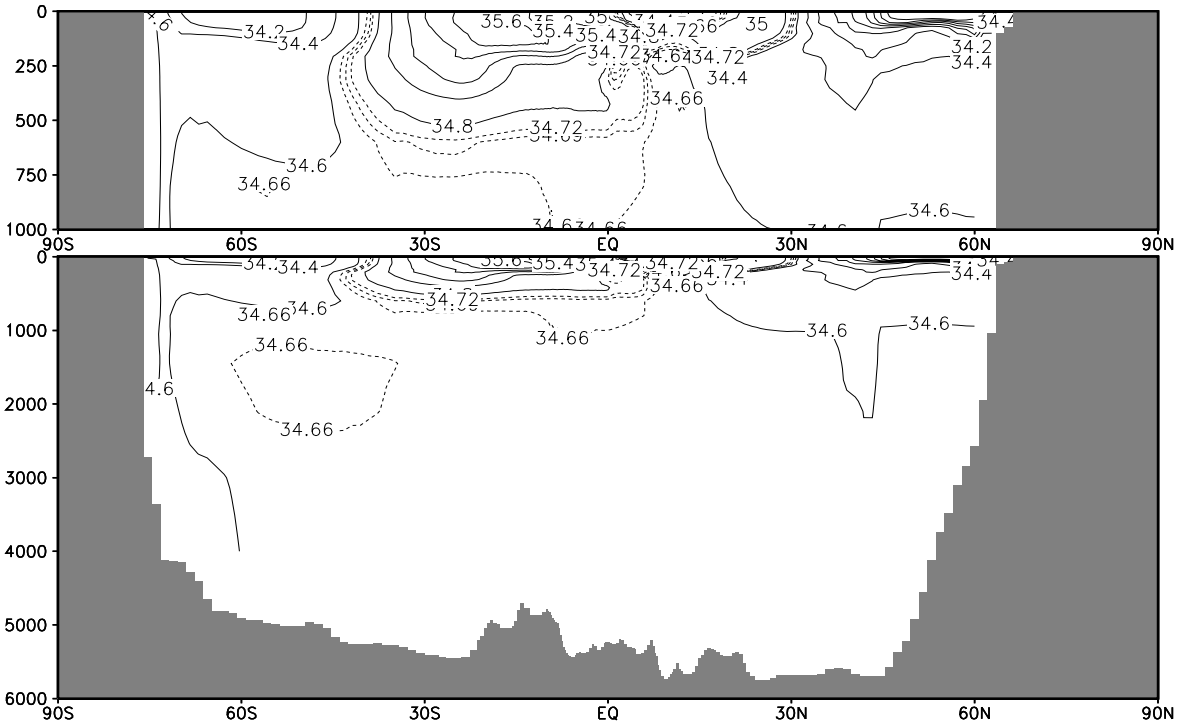

Figure 38c: Simulated zonal-mean salinity in the Pacific Ocean.

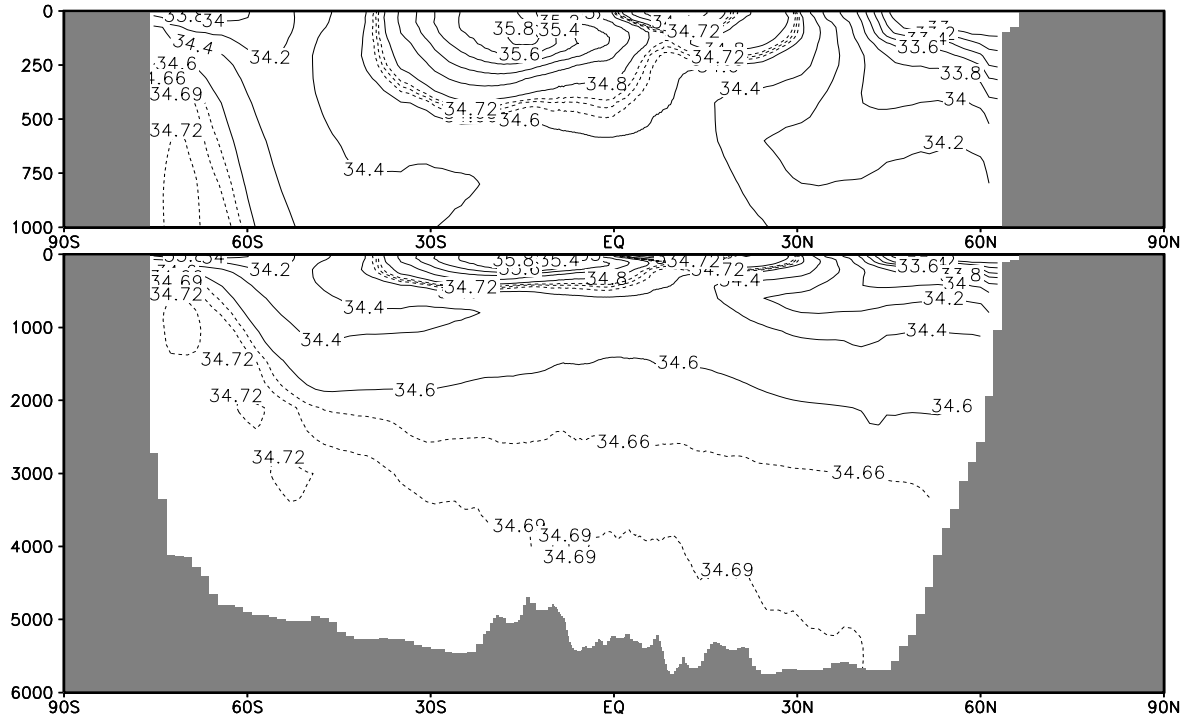

Figure 38d: Observed zonal-mean salinity in the Pacific Ocean calculated from the Levitus climatology (Levitus et al. 1994) and interpolated onto the model grid.

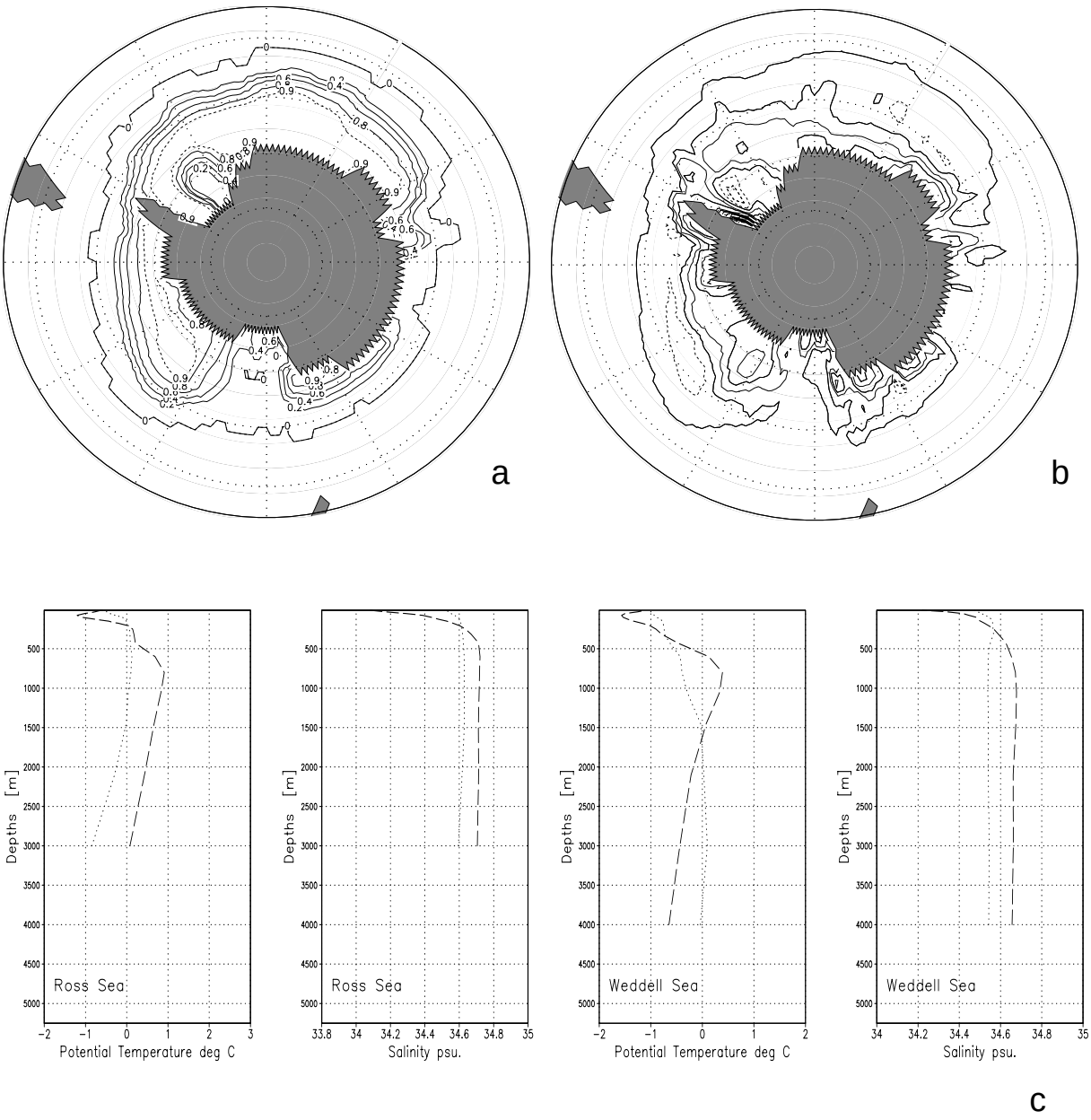

Figure 39: (a) Simulated mean sea-ice concentration in the Southern Ocean in September. Contour interval is 0.2. (b) Simulated annual net sea-ice growth in the Southern Ocean. Contour interval is 20 cm. Dashed contours are for ice melt. (c) Simulated (dotted) and observed (dashed) profiles of salinity and temperature in the Ross and Weddell Seas.

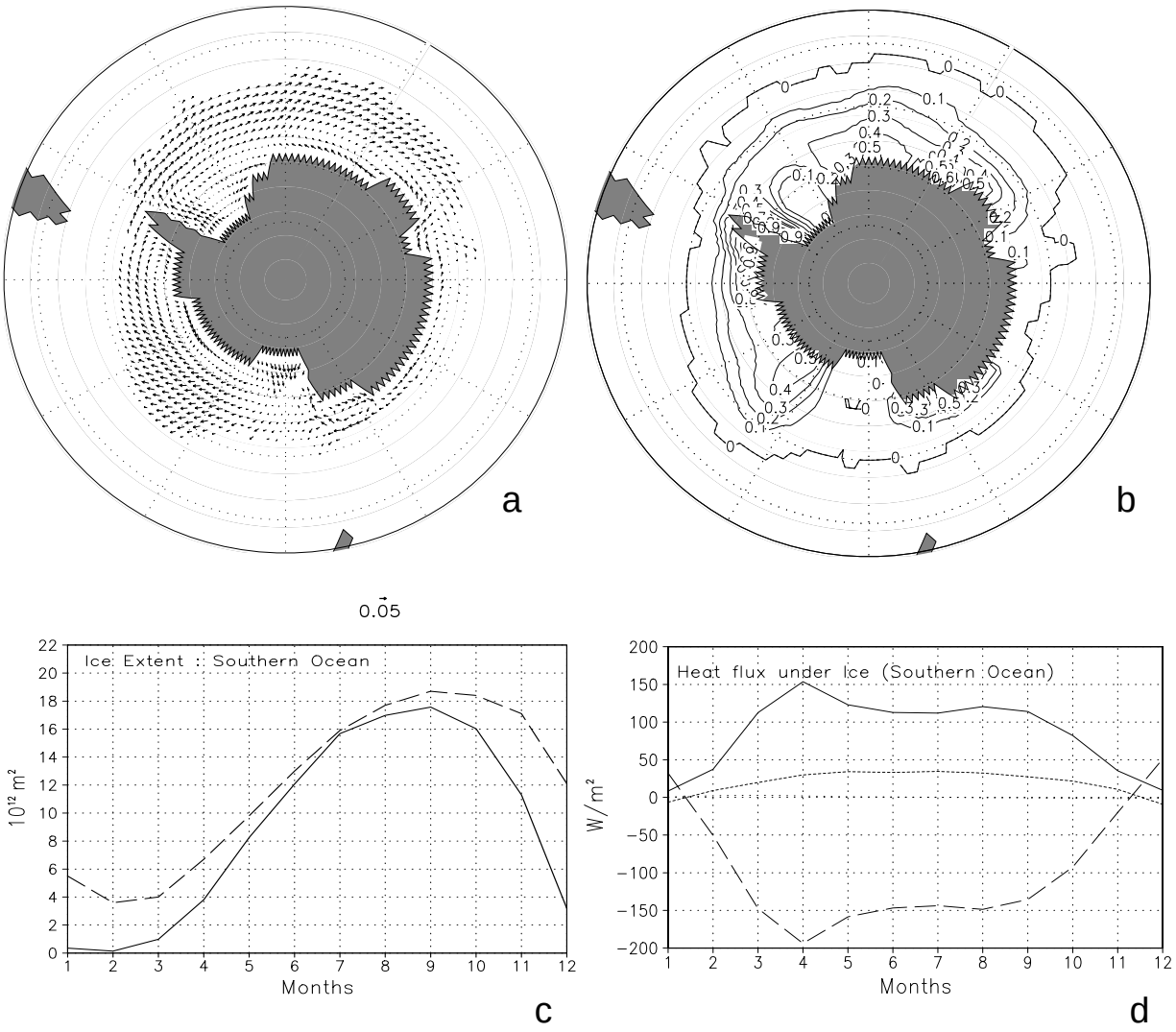

Figure 40: (a) Annual mean sea-ice drift in the Southern Ocean. Arrows which represent a speed above 5 cm s^{-1} are truncated to one zonal gridpoint distance. (b) Simulated September sea-ice thickness. The contour interval is 10 cm. The gridcell areal average is shown. (c) Seasonal cycle of sea-ice extent. The full curve shows the model simulation. The dashed curve is from Gloersen et al. (1992). (d) Seasonal cycle of heat flux into the mixed layer in the Southern Ocean ice region (atmospheric fluxes : long-dashed, convective adjustment : full, vertical diffusion : short-dashed, horizontal advection and diffusion : dotted).

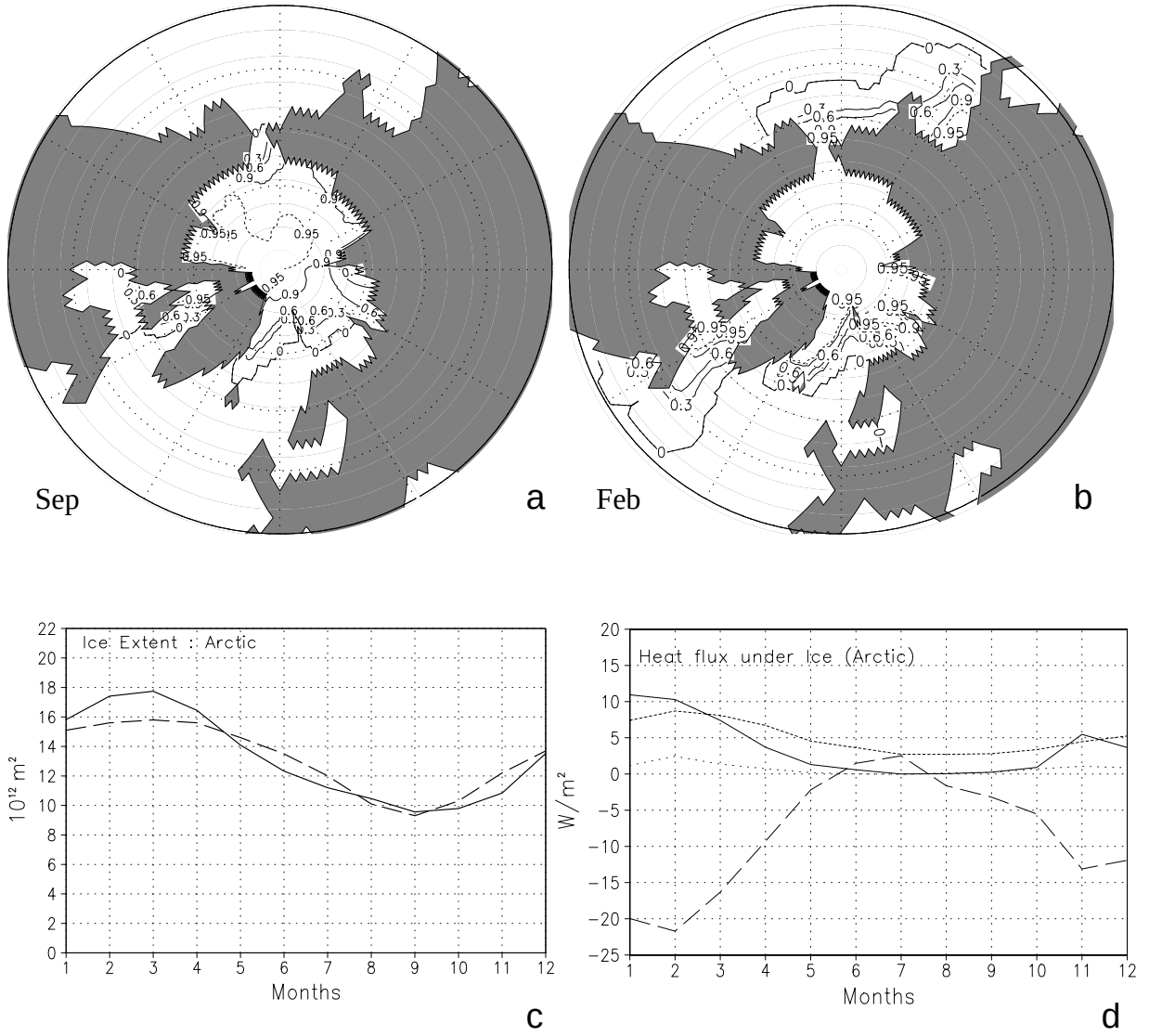

Figure 41: (a) Mean September sea-ice concentration. Note that the zero line is the envelope of all distributions in September of the last 15 years of integration. C.I. is 0.3. The 95% ice coverage is given by the dashed line. (b) Same as (a) for February. (c) Seasonal cycle of the simulated (full line) and observed (dashed line, Gloersen et al. 1992) ice extent. (d) Seasonal cycle of heat flux into the mixed layer in the northern hemisphere ice region (atmospheric fluxes : long-dashed, convective adjustment : full, vertical diffusion : short-dashed, horizontal advection and diffusion : dotted).

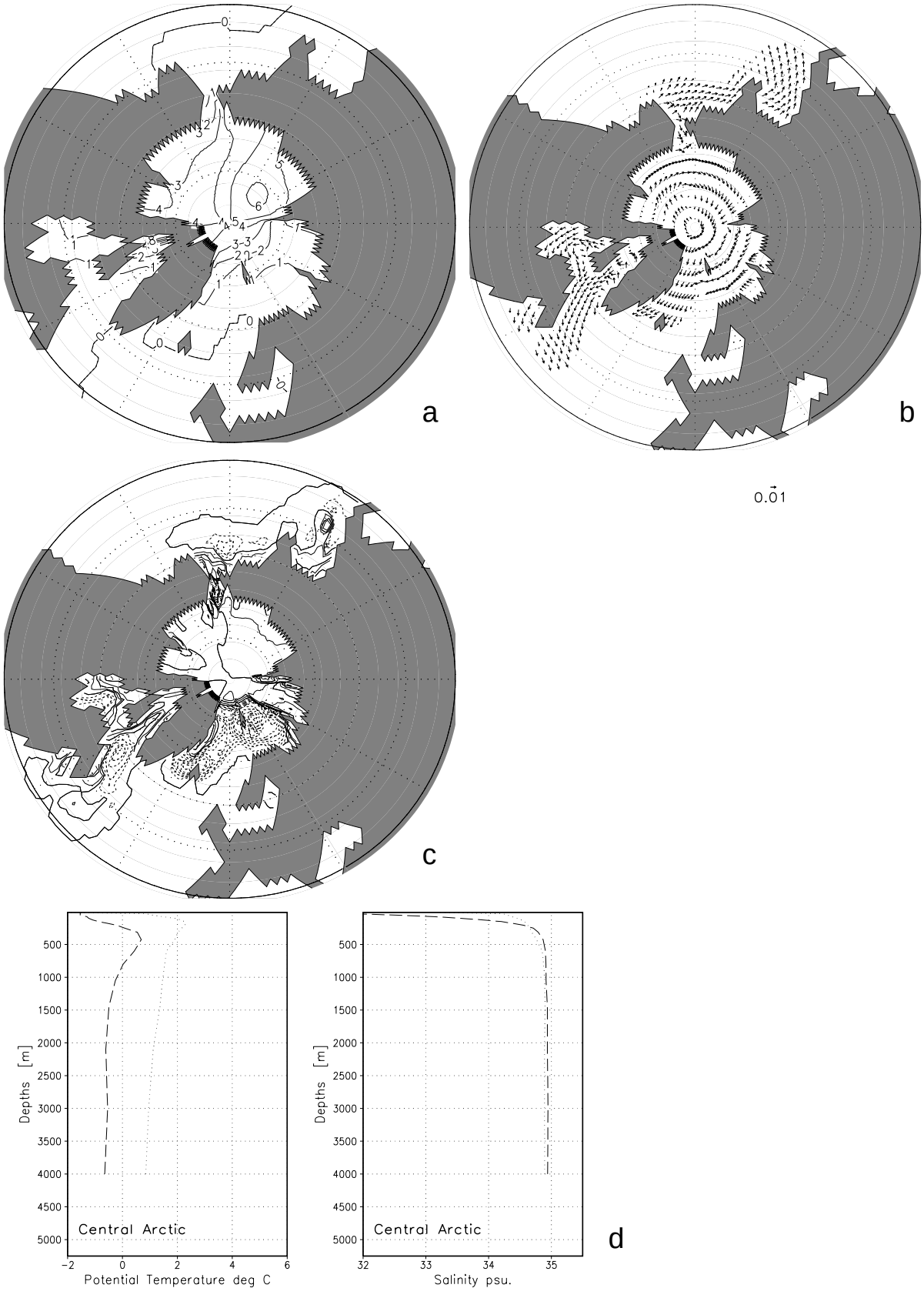

Figure 42: (a) Annual-mean sea-ice thickness in the northern hemisphere. C.I. is 1 m. (b) Annual mean sea-ice drift. Arrows which represent a speed above 1 cm s^{-1} are truncated to one zonal gridpoint distance.
(c) Simulated annual net sea-ice growth. Contour interval is 25 cm. Dashed contours are for ice melt.
(d) Simulated (dotted) and observed (Levitus et al. 1994, dashed) profiles of salinity and temperature in the Central Arctic.